

EXPERIMENTAL AND NUMERICAL INVESTIGATION OF CONFINED PREMIXED FLAME

By

Younis Mahal Najim

A DISSERTATION

Submitted to
Michigan State University
in partial fulfillment of the requirements
for the degree of

Mechanical Engineering - Doctor of Philosophy

2017

ABSTRACT

EXPERIMENTAL AND NUMERICAL INVESTIGATION OF CONFINED PREMIXED FLAME

By

Younis Mahal Najim

Understanding the dynamics of premixed flames propagating during constant volume combustion is key to enhancing the performance of existing combustion devices, which provide 80% of the world's energy supply, and reducing the impact of pollution on the environment. This work experimentally and numerically investigates confined premixed flame propagation in an initially quiescent mixture. Three combustion chambers are used; a curved wave disc engine channel and rectilinear channels of aspect ratio 7 and 10. The mixture is methane/air and syngas (H_2/CO)/air initially at atmospheric pressure and room temperature. The channel walls are assumed to be isothermal to incorporate the effect of heat transfer. For two-dimensional analysis, the reaction rate is modeled using both detailed and reduced kinetic mechanisms. The mass diffusion is investigated using three different diffusion models with different levels of approximation; the multicomponent diffusion model of Chapman-Enskog including the Soret effect; the mixture-averaged model; and constant Lewis number. For three-dimensional analysis, a large eddy simulation coupled with the transport equation of the reaction progress variable is used. In this work, the reaction rate predicted using the Boger model of algebraic flame surface density is modified by incorporating a transient flame speed that accounts for the variation in the temperature and pressure of the unburned gases. The experimental measurements include schlieren photography to track the flame structure and propagation speed, and the pressure-time history during the combustion process is measured by a pressure sensor mounted in the channel wall. The experimental measurements validate the numerical simulation results and provide further understanding of the flame and pressure dynamics.

Unlike behavior previously reported in straight or 90° bend channels, premixed flame propagation in the wave disc engine channel exhibits different features: the convex tulip flame converts back into a concave flame and thus reveals the influence of channel geometry on flame evolution. The experiments show that the rate of pressure change eventually becomes negative mainly due to heat losses that engender a correspondingly slower flame propagation during the final stage of burning. The analysis of the numerical results reveals the effect of the interaction between the flame front, pressure field, and flame-induced flow on flame evolution during all stages of flame structure development. The results also demonstrate that both multicomponent diffusion with the Soret effect and the mixture-averaged model produce slightly different results in flame speed, structure, peak temperature, and average pressure for the methane/air mixture, while the deviation is more pronounced for syngas flames. The methane/air flame produced by the unity Lewis number model, however, lags behind its counterparts during early stages and dramatically accelerates, at which time the values of peak temperature and average pressure show unrealistic behavior. Furthermore, unity Lewis number flames develop an artificial second tulip flame after the first tulip flame is annihilated. This second tulip flame is neither observed in the Chapman-Enskog and mixture-average simulations, nor in the experiments. This reveals the role of the Lewis number in the intrinsic thermodiffusive flame instabilities and tulip flame formation. The three-dimensional simulation uncovers an interesting behavior for the flame structure that is introduced here as a “transverse tulip” flame, which has not been previously reported. The “transverse tulip” flame evolves in the direction perpendicular to that of the initial tulip flame after the latter undergoes the transition from cusped convex back to the concave finger shape. The commonly used Zimont model produces an unrealistically diffused flame front. The large eddy simulation coupled with the here-modified algebraic flame surface density overcomes this issue and reproduces the experimental observations of the flame structure, pressure-time history, and burning time with good agreement.

Copyright by
YOUNIS MAHAL NAJIM
2017

ACKNOWLEDGMENTS

This work would not have been possible without an unforgettable and enriching association with the Turbomachinery Laboratory and Combustion Laboratory at Michigan State University.

I would like to express my deep sense of gratitude and indebtedness to my advisor, Prof. Norbert Mueller, for providing me the opportunity and guidance throughout my PhD study. His keen interest and personal involvement during this study is beyond words of gratitude.

I am deeply indebted to Prof. Indrek Wichman for his close association with every part of this project and for providing space in his laboratory to set up and run my experiments. I am incredibly grateful to Prof. Charles Petty for his invaluable advices and discussion about the turbulence modeling which led me to understand various aspects of turbulence modeling and realizability. Many thanks go to Prof. Abraham Engeda for his helpful criticisms and suggestions as members of the supervisory committee for this dissertation.

I wish to thank my colleagues within the Turbomachinery Laboratory, for their continuous help and every bit of their valuable input. I gratefully acknowledge the Higher Committee For Education Development and Ministry of Higher Education and Scientific Research in Iraq for the unique opportunities given to me, allowing me to pursue my PhD degree.

At last but not the least, I would like to thank my family for their endless support in achieving this great success in my life. I am forever grateful for all the assistance and encouragement they have provided throughout my academic life.

TABLE OF CONTENTS

LIST OF TABLES	viii
LIST OF FIGURES	ix
KEY TO SYMBOLS	xv
KEY TO ABBREVIATIONS	xix
Chapter 1 INTRODUCTION	1
1.1 Background	1
1.2 Motivation and Objectives	3
1.3 Thesis Outline	6
Chapter 2 LITERATURE REVIEW - CONFINED PREMIXED FLAME	7
2.1 Dynamics of confined premixed flame	7
2.2 Molecular Diffusion Impact on Confined Premixed Flame	12
2.3 Syngas Premixed Flame	14
2.4 Turbulent Premixed Flame	15
Chapter 3 GOVERNING EQUATIONS AND MODELING	18
3.1 Laminar Premixed Flames	19
3.1.1 Reaction rate - Kinetic Mechanism	21
3.1.2 Molecular diffusion	26
3.1.2.1 Lewis Number	29
3.1.3 Gas properties	31
3.2 Turbulent Premixed Flame	32
3.2.1 Large Eddy Simulation	33
3.2.1.1 LES filtering	34
3.2.1.2 Filtered Conservation Equations	35
3.2.1.3 Subgrid Scale Model	37
3.2.2 Combustion Model- Flamelet Concept	38
3.2.2.1 Flame Speed Closure	39
3.3 Boundary and Initial Conditions	40
3.3.1 Numerics	40
Chapter 4 EXPERIMENT SETUP	43
4.1 Combustion Chambers	43
4.2 Experiment Setup	46
4.3 Methods of Measurement	48

Chapter 5	EXPERIMENTAL AND NUMERICAL SIMULATION	51
5.1	Flame Front Evolution	51
5.1.1	Non-symmetrical Tulip Flame	51
5.1.2	Diffusion impact	57
5.1.2.1	Methane/air flame	57
5.1.2.2	Syngas flame	61
5.2	Pressure Dynamics and Flame Speed	63
5.3	Flame-Induced Flow	68
5.3.1	Flame-induced flow and vorticity	68
5.3.2	Flame flow interaction	71
5.4	Impact of Soret effect	75
5.5	Influence of Effective Lewis Number	84
5.6	Characteristic Burning Regime	89
5.7	Influence of Mixture stoichiometry on Syngas Flames	91
5.7.1	Flame structure	91
5.7.2	Pressure dynamics	96
5.7.3	Flame-flow interaction	99
Chapter 6	FLAME SURFACE DENSITY FOR LES	104
6.1	Three-Dimensional Structure of the Flame Front	104
6.1.1	Transverse tulip flame	104
6.1.2	3D flame dynamics in a rectangular channel	108
6.1.3	Flame surface density	111
6.1.4	Turbulent flame speed	113
6.1.5	Assessment of AFSD	117
Chapter 7	CONCLUSIONS AND RECOMMENDATIONS	121
7.1	Conclusion	121
7.2	Recommendations	125
APPENDICES		126
	Appendix A Grid Resolution Test	127
	Appendix B Turbulent Flame Model	131
BIBLIOGRAPHY		135

LIST OF TABLES

Table 3.1:	Chemical-Kinetic Mechanisms used in this work.	21
Table 3.2:	Mass diffusion Coefficient for Multicomponent, mixture-average, and constant Lewis number.	28
Table 3.3:	Summary of CFD simulation cases.	42
Table 5.1:	Cases for syngas flame simulations.	92
Table A.1:	CFD cases used to examine grid resolution.	127

LIST OF FIGURES

Figure 1.1:	Schematic diagram illustrating premixed flames structure.	2
Figure 1.2:	Schematic design of the wave disc engine.	5
Figure 2.1:	Sequence of flame phases developed in a rectangular channel.	9
Figure 2.2:	Modified turbulent flames regimes Poinot & Veynante (2005) and Peters (1999)	17
Figure 3.1:	Flame speed predicted by San Diego kinetic mechanisms and tested against available experimental data from literature Beeckmann et al. (2014), Halter et al. (2005), Vagelopoulos & Egolfopoulos (1998), Qin & Ju (2005). The analysis consists one-dimensional free propagating, premixed flame.	24
Figure 3.2:	Laminar flame speed for syngas kinetic mechanism of Kèromnès et al. (2013) validated with available experimental data Hassan et al. (1997), Burbano et al. (2011).	24
Figure 3.3:	Laminar flame speed for DRM19, San Diego Mech. under different operating pressures.	25
Figure 3.4:	Laminar flame speed for DRM19 and San Diego Mech. under different reactants temperature.	25
Figure 3.5:	Turbulence energy spectrum regimes	34
Figure 4.1:	Schematic diagram of computational domain.	44
Figure 4.2:	Schematic diagram of single wave disc engine channel used for experimental measurements	45
Figure 4.3:	Closed rectangular channel serves as combustion chamber	45
Figure 4.4:	Schematic diagram of the experimental setup. The premixed flame images are measured at rate 3600 <i>fps</i> , and the pressure readings are sampled at 5 <i>kHz</i> . . .	47
Figure 4.5:	Pressure measurements tested against available data from literature Dunn-Rankin et al. (1988)	49
Figure 4.6:	Normalized values of average pressure measurements for stoichiometric CH_4 /air flame.	50

Figure 4.7:	Raw data recorded by pressure transducer for eight(8) experiment to ensure the reproducibility of the tests.	50
Figure 5.1:	Evolution of the WDE confined premixed flame using schlieren photography (images on the left) and mass fraction contours of HCO , which serve to track the flame locus, from the numerical simulations (images on the right): (a-d) hemispherical expansion and evolution to a concave “finger” flame; (e) inner part of lateral flame touches the inner sidewall; (f) outer part of lateral flame touches the outer sidewall and flame front flattens; (g) initial formation of tulip flame cusp which generates the characteristic convex tulip flame shape; (h-k) inner flame tongue grows by radially displacing the flame cusp toward the outer sidewall ; (l) upper flame tongue disappears; (n-o) tulip flame converted to curved flame.	55
Figure 5.2:	Comparison between the experimental and numerical simulations of the normalized flame locations X_F/X_{Fmax} . Also shown is the ratio of these normalized flame locations, showing that the numerical flame evolution is always faster than the experimental flame evolution.	56
Figure 5.3:	Methane/air premixed flame front development; (on the right) flame shadowgraphy and (on the left) flame fronts for $M(I)$, $M(II)$, and $M(III)$ models: (a-f) flame of $M(III)$ lags behind $M(I)$ and $M(II)$ and small discrepancy can be observed between $M(II)$ and $M(II)$ in b, (g-h) $M(III)$ flame is ahead of $M(I)$ and $M(II)$; (i-k) $M(III)$ develops a second tulip flame; (l) $M(I)$, $M(II)$, and $M(III)$ and converted into concave flames.	59
Figure 5.4:	Flame tip distance from igniter location recorded at the channel centerline for models $M(I)$, $M(II)$, $M(III)$ and the experiment. The initial condition from which time is reached is the instant at which all flames have penetrated 5 mm into the channel.	60
Figure 5.5:	Premixed syngas flame front development for $M(I)$, $M(II)$, and $M(III)$ diffusion models.	62
Figure 5.6:	Experimental measurements of normalized flame speed, normalized pressure $P[bar]/3.15$, normalized rate of pressure change $(dP/dt)[bar/s]/866$, and normalized pressure second derivative. The numbers in these denominators are maximum values that are used to scale all of the curves for improved visualization. The data shown are averages of eight separate experiments. Also shown on the right-hand scale is the experimentally measured variance of the pressure data, indicating it to be under 1%. The experiments measure flame position: flame speed is obtained by differentiation.	66

Figure 5.7:	Interaction between flame front and flame-induced flow: (a) burned gas produced by lateral flame moves from sidewalls toward the centerline of the channel, and then is deflected along the channel centerline; (b) inner lateral flame is quenched while upper lateral flame continues to thrust the burned gases toward the inner wall and is then deflected toward the flame front; (c) inversion of burned gas flow; (a-c) vorticity is generated in the near wall region of the channel by the forward forced flow; (d-f) vorticity is generated in burned gas behind the flame front by the rearward forced flow. The change in flame morphology from concave to convex occurs between (c) and (d) as the tulip is formed while the change from convex to concave occurs between (e) and (f) as the concave flame front is reconstituted.	70
Figure 5.8:	Velocity field induced by the flame at different combustion time.	71
Figure 5.9:	Flame-induced flow and the characteristic saddle points of unity Lewis number flame: (a) spherical flame surrounds saddle point; (b) finger flame front away from saddle point ; (c) saddle point moves close to skirt flame; (d-f) saddle point moves close to lower tongue of the first and second tulip flame; (g-h) no saddle point was observed.	73
Figure 5.10:	Soret effect impact on the CH_4 species concentration plotted along the normalized channel width in the unburned region.	76
Figure 5.11:	Soret effect impact on the AR species concentration plotted along the normalized channel width in the unburned region.	76
Figure 5.12:	Soret effect impact on the O_2 species concentration plotted along the normalized channel width in the unburned region.	77
Figure 5.13:	Soret effect impact on the N_2 species concentration plotted along the normalized channel width in the unburned region.	77
Figure 5.14:	Soret effect impact on the H_2O species concentration plotted along the normalized channel width in the burned region.	78
Figure 5.15:	Soret effect impact on the CO_2 species concentration plotted along the normalized channel width in the burned region.	79
Figure 5.16:	Soret effect impact on the H_2 species concentration plotted along the normalized channel width in the burned region.	79
Figure 5.17:	Soret effect impact on the O species concentration plotted along the normalized channel width in the burned region.	80

Figure 5.18: Mass fraction of H_2 and CO distributed across the WDE channel for the case $M(I)$	81
Figure 5.19: Mass fraction of O_2 and N_2 distributed across the WDE channel for the case $M(I)$	81
Figure 5.20: Mass diffusion flux due to Soret effect at, 14.96 ms for: (a) CH_4 ; (b) O_2 ; (c) CO_2 ; (d) N_2	83
Figure 5.21: Average pressure developed in the WDE channel under three different diffusion model $M(I)$, $M(II)$, and $M(III)$ for stoichiometric methane/air.	85
Figure 5.22: Peak temperature developed in the WDE channel under three different diffusion model $M(I)$, $M(II)$, and $M(III)$ for stoichiometric methane/air.	85
Figure 5.23: Average pressure developed in the WDE channel under three different diffusion model $M(I)$, $M(II)$, and $M(III)$ for syngas/air of $\phi = 0.7$ and 50% H_2	86
Figure 5.24: Peak temperature developed in the WDE channel under three different diffusion model $M(I)$, $M(II)$, and $M(III)$ for syngas/air of $\phi = 0.7$ and 50% H_2	87
Figure 5.25: Evolution of effective Lewis number derived from case $M(II)$ for methane/air mixture at different combustion time.	88
Figure 5.26: Normalized inverse Peclet number ratio $\mathcal{N}/\mathcal{N}_{(2)}$ versus normalized total time t/t_{max} . The hydrodynamic Regime (1), and the thermodiffusive Regime (2) occupy 10 and 20% of the total time. The heat-loss Regime (3) occupies the remaining 70% of the burn time.	90
Figure 5.27: Syngas flame structure for different stoichiometric ratios and hydrogen content (C1-9).	93
Figure 5.28: Syngas combustion time for different mixture stoichiometry.	95
Figure 5.29: Instantaneous syngas flame distance for different mixture stoichiometry.	96
Figure 5.30: Time-history of the channel average pressure under different mixture stoichiometry.	97
Figure 5.31: Time-history of the normalized pressure under different mixture stoichiometry.	98
Figure 5.32: Normalized syngas flame distance for different mixture stoichiometry.	99

Figure 5.33: Flame front interaction with flame-induced flow for stoichiometric ratio of 0.7 for different combustion time, hydrogen content, and flame front position at the channel centerline.	101
Figure 5.34: Flame front interaction with flame-induced flow for stoichiometric ratio of 1.0 for different combustion time, hydrogen content, and flame front position at the channel centerline.	102
Figure 5.35: Flame front interaction with flame-induced flow for stoichiometric ratio of 1.5 for different combustion time, hydrogen content, and flame front position at the channel centerline.	103
Figure 6.1: Flame structure evolution;(a) hemispherical flame, (b) finger flame, (c) skirt flame (d) straight flame front on transverse plane and concave flame on lateral plane, (e) non-symmetric tulip flame on lateral plane, (f) initial tulip flame back to concave finger shape (g-h) transverse tulip flame.	106
Figure 6.2: Experiment flame front shadowgraphy (on the left side) and numerical simulation flame front on plane $z = 0 \text{ mm}$ and $z = 7.25 \text{ mm}$ projected on one plane (on the right side).	107
Figure 6.3: Three-dimensional, flame front structure developed in a rectangular chamber. (a) spherical expansion of ignition kernel, (b) finger-flame expansion, (c) skirt-flame, (d) tulip-flame.	109
Figure 6.4: Evolution of flame structure, flame-induced flow, and dynamics of saddle point.	110
Figure 6.5: Flame surface density and product formation rate for WDE channel.	112
Figure 6.6: Flame surface density and product formation rate for the rectangular chamber.	112
Figure 6.7: Variation of flame speed during the flame propagation in the WDE channel.	114
Figure 6.8: Temperature of unburned gases and average pressure developed in the WDE channel.	115
Figure 6.9: Transient flame speed developed in a rectangular channel.	116
Figure 6.10: Unburned gases average temperature and pressure for premixed flame propagating in the rectangular channel.	116
Figure 6.11: Time-history of the average pressure developed in a rectangular chamber.	118

Figure 6.12: Comparison between flame predicted by algebraic flame surface density and experimental observation.	119
Figure 6.13: Comparison between modified algebraic flame surface density and Zimont model	120
Figure A.1: Flame front structure and flame-generated flow predicted by (a) current mesh size(150×1500) and (b) finer mesh(300×3000).	128
Figure A.2: Average pressure of the syngas/air premixed flames.	129
Figure A.3: Methane/air flame front structure predicted by 0.05 mm and 0.025 mm maximum cell sizes. The Flames front are represented by C_2H_6 contours.	130
Figure A.4: Mass fraction of HCO species plotted along a line of 0.8 mm passing through the methane/air flames front.	130
Figure B.1: Maximum cell Reynolds number evaluated during flame propagating in the 3D rectangular channel.	131
Figure B.2: Maximum cell Reynolds number evaluated during flame propagating in WDE channel.	132
Figure B.3: Average Damköhler number for WDE channel.	133
Figure B.4: Unburned gases density developed during flame propagation in a rectangular channel.	134
Figure B.5: Unburned gases density developed during flame propagation in the WDE channel. Also showing the mixture average density.	134

KEY TO SYMBOLS

English Symbols

A_{fj}	pre-exponential factor of reaction j
c	reaction progress variable
c_p	specific heat capacity
Da	Damköler number
\mathbf{D}_{kl}	multicomponent mass diffusion coefficient
D_{Tk}	thermal diffusion coefficient of species k
d	distance to the closest wall
E_j	activation energy of reaction j
e	total energy
F_k	diffusion driving force
$G(x_i)$	LES filter function
h	enthalpy
H_k^o	enthalpy of species k evaluated at standard condition
\mathbf{I}	matrix identity
\mathbf{J}_k	molecular mass flux of species k
Ka	Karlovitz number
k_B	Boltzmann constant
K_{fj}	forward rate of reaction j constants
K_{rj}	reverse rate of reaction j constants
Le	Lewis number
Ls	characteristic length in WALE SGS model

l_t	integral length scale
M_k	molecular weight of species k
N_s	total number of mixture species
\mathcal{N}	non-dimensional characteristic time ratio
p	pressure
p_{atm}	atmospheric pressure
Pr	Prandtl number
Q_i	Progress of reaction
\mathbf{q}	net energy crossing the control volume surface by the mechanisms of molecular conduction and diffusion of species k
R	gas constant, 8314 (J/kgK)
Re_t	turbulent Reynolds number
S_k^o	entropy of species k evaluated at standard condition
S_l	laminar flame speed
$S_{l_{ref}}$	laminar flame speed evaluated at standard conditions
t	time
T	temperature
T_u	unburned gases temperature
\mathbf{T}	stress tensor based on the Newtonian fluid assumption
T^*	dimensionless temperature ($T^* = T/(\varepsilon/k_B)_k$)
\mathbf{u}	the mass average velocity vector of the gas mixture, $\mathbf{u} = (u, v, w)$
V_k	diffusion velocity of the species k
X_k	mole fraction of species k

x, y, z	Cartesian coordinates axis
Y_k	mass fraction of species k
$(\tilde{})$	filtered quantity for LES

Greek Symbols

α	thermal diffusivity of the mixture
β_j	temperature exponent of reaction j
Δ	the LES filter width
δ_{ij}	Kronecker delta function
ε_k	the Lennard-Jones potential well depth
κ	von Kármán constant
λ	thermal conductivity
μ	mixture-average dynamic viscosity
μ_{SGS}	subgrid-scale viscosity
ν''_{kj}	stoichiometric coefficients of products of species k
ν'_{kj}	stoichiometric coefficients of reactants of species k
∇	the gradient operator
ρ	density
ρ_u	unburned gases density
Σ	flame surface density
σ_{ij}	subfilter stresses
σ_k	the Lennard-Jones collision diameter
ϕ	equivalence ratio

ψ_s	stoichiometric ratio air to fuel ratio
Ω_E	collision integral function
ω_k	molar rate of production of species k ,
ω_T	heat release term
τ_l	the integral turbulent timescale
τ_c	the chemical or reaction rate timescale

KEY TO ABBREVIATIONS

AFSD	algebraic flame surface density
BML	Bray Moss Libby model
CNC	Computer Numerical Control
CV	constant volume
DNS	direct numerical simulation
fps	frame per second
FSD	flame surface density
LES	large eddy simulation
M(I)	multicomponent diffusion model with Soret effect included
M(II)	mixture-averaged diffusion model
M(III)	constant Lewis number
PDE	pulse detonation engine
RANS	Reynolds Averaged Navier Stokes equations
SGS	subgrid-scale
WALE	wall-adapting local eddy-viscosity subgrid-scale model
WDE	wave disc engine

Chapter 1

INTRODUCTION

1.1 Background

Combustion is a chemical reaction in which the oxidizer rapidly reacts with the fuel and liberates heat. The fuel can be a solid (such as wood and coal), liquid (such as gasoline and hydrocarbon fuel), and gas (such as natural gas). The combustion field is extremely broad and can be classified based on the way the fuel and oxidizer are introduced in the flame zone. In premixed flames, as their name implies, the fuel and oxidizer are thoroughly mixed at the molecular level prior to their burning. This combustion mode is used in many practical combustion devices such as gasoline-fueled internal combustion engines, lean premixed in a power-generating gas turbine, gas appliance stoves. The structure of premixed flames is illustrated in Fig. 1.1.

On the other hand, the non-premixed flames in which the fuel and oxidizer are separately introduced into the combustion chamber where they must mix before significant reaction can commence. Such flames are used in many combustion processes where the reaction rate is controlled by mixing processes which are due to molecular diffusion, convection, and turbulent mixing.

Other combustion modes are the laminar and turbulent flames depending on the flow, whether it is laminar or turbulent. Moreover, in gasdynamics, the terms deflagration and detonation are used to describe another combustion modes in which the flames propagate at subsonic and supersonic speed, respectively.

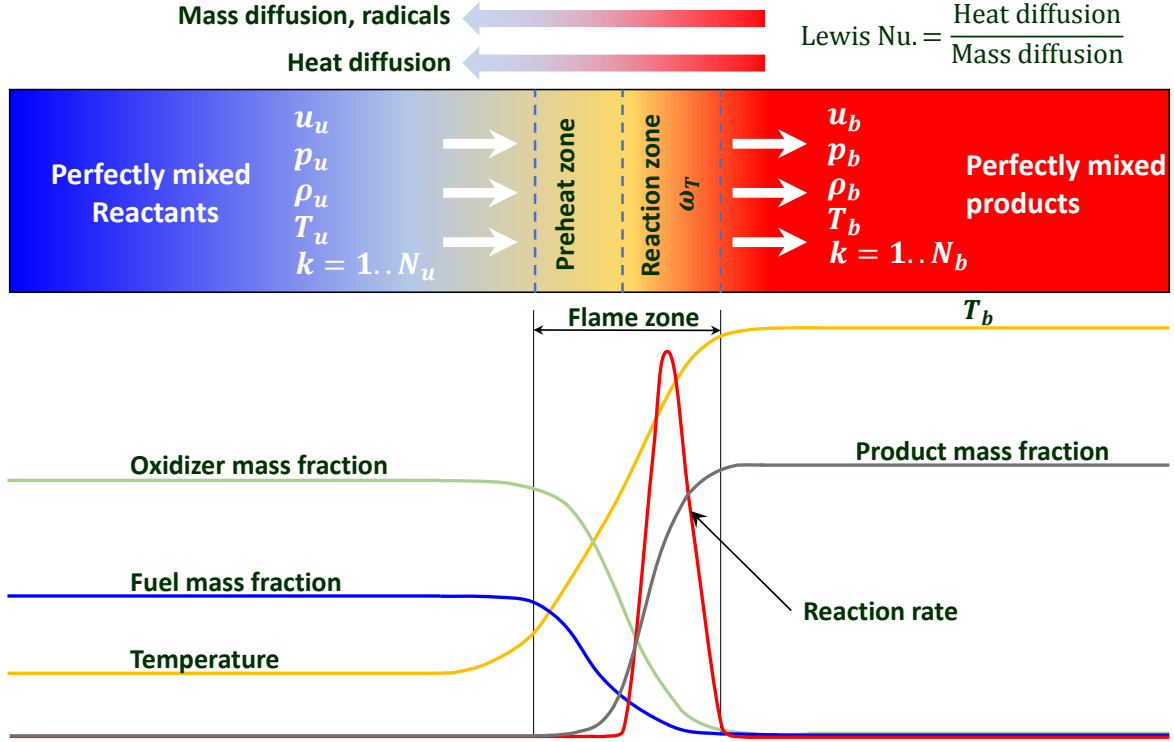


Figure 1.1: Schematic diagram illustrating premixed flames structure.

The premixed flames involves two distinct zones; preheat and reaction zones. In the preheat zone, the energy diffuses from the burnt high temperature region and heats the mixture to the temperature where combustion reactions commence. The main fuels oxidize into products in the reaction zone where the heat of combustion is released. Also, the concentration and temperature gradient in the reaction zone represent a potential driving force for radicals and species diffusion. The heat and mass diffusion play crucial role in the combustion process and flame structure. The ratio between heat and mass diffusion is known as Lewis number.

Unlike non-premixed flames, the premixed flames are characterized by laminar flame speed which can be defined as the propagation speed normal to the unwrinkled flame surface. The laminar flame speed is one of the most important property of a combustible mixture that depends on the thermochemical and transport properties of the mixture, and therefore it provides information about the reactivity and diffusivity of the reacting mixture Shang et al. (2016). It is also used as a basis

for turbulent flame speed and to validate the chemical kinetic mechanism.

The increase in turbulence intensity in the vicinity of flame front changes the flame structure from laminar smooth front to wrinkled, corrugated, stretched, thickened flame and end up with flame quenching when the Kolmogorov length scale becomes larger than the flame stretch limit Poinso & Veynante (2005), Peters (2000). The turbulence mixing speed up the transport of heat and radicals at the flame front and hence increase the reactivity and flame speed.

1.2 Motivation and Objectives

Combustion are essential process for power generation which indisputably represents a primary driving potential of human development. Currently, 85% of the energy consumed in the United States comes from combustion of hydrocarbon fuel such as natural gas, petroleum, and coal McIlroy et al. (2006). However, the increase in global energy demand and the limitation of hydrocarbon energy sources in addition to environmental concerns exert continuous need for highly efficient combustion devices and alternative energy resources. Natural gas and syngas offer an alternative and attractive source of energy by diversifying the energy use and emitting less CO_2 per unit of energy compared to oil and coal which helps to slow down the impact of fossil fuel combustion on climate change. The availability of natural gas is deemed to be potentially larger than both conventional crude oil and unconventional resources combined. In the United State, the production of natural gas increased by 35% from 2005 to 2013 and its share of the total U.S. energy consumption rose from 23% to 28% U.S Department of Energy (2015).

This particular work is motivated by research and development of the wave disc engine (WDE), which was designed and built at Michigan State University (MSU). A schematic design of WDE is shown in Fig. 1.2. The thermodynamic foundation of this engine is the Humphrey cycle that

utilizes an internal combustion engine cycle consisting of compression which is mainly performed through pressure waves, constant volume combustion, work extraction from hot gases expansion, and heat rejection to the ambient. All these processes take place in radial arranged and curved channels mounted around the WDE shaft.

The WDE must work at high frequencies in order to produce power with a reasonable efficiency. Details concerning the wave disc engine concept can be found in Sun et al. (2012), Sun (2011), Kiran (2013). It has been demonstrated that the time for combustion inside the WDE channel consumes about 95% of the total cycle time Hariharan & Wichman (2014). This indicates that the time required for the burning process limits the WDE from operating at high frequencies, which is a key issue for improving its performance. This also shows that the time remaining for the work extraction stroke is brief compared with the cycle time. Any attempt to extract more work should be accompanied by increasing the time for work harvesting. Accelerating the flame propagation rate inside the WDE channel can reduce the burning time and allow the WDE to operate at higher rotational speeds in order to produce more work Johansen (2009).

The main objectives of this work is as follow:

- To better understand the pressure and flame dynamics inside the wave disc engine channel. This is an essential step toward establishing a reference point from which future advancements in flame and burning acceleration in WDEs can be assessed.
- To provide further understanding on the impact of diffusion models and thermal diffusion on the dynamics of premixed methane/air and syngas/air flames propagating in a curved non-symmetrical closed channel. The influence of mixture stoichiometry on syngas flame structure and pressure dynamics is also examined.
- Since the available computational resources can't handle the the three dimensional model

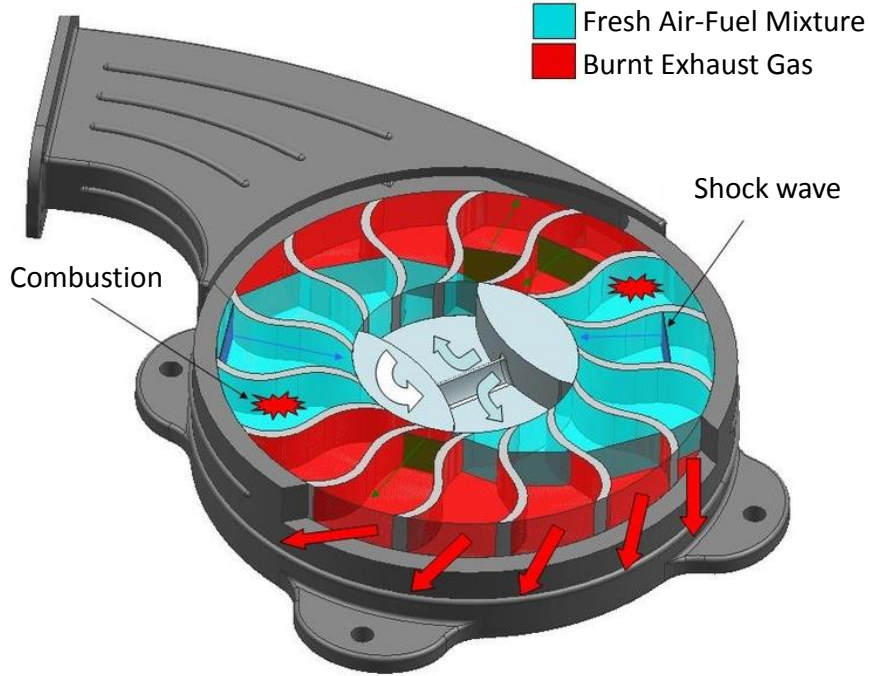


Figure 1.2: Schematic design of the wave disc engine.

with detailed chemistry and diffusion model, the three-dimensional model of WDE and rectangular channel ($38\text{ mm} \times 38\text{ mm} \times 279.4\text{ mm}$) is solved using large eddy simulation and single transport equation for reaction progress variable in which the source term is predicted using the algebraic flame surface density modified by including a temperature- and pressure-dependent laminar flame speed.

- Since the premixed flame propagates into quiescent mixture and the flow induced by the flame is evolving with time, an adaptive switch is used between Metghalchi-Keck flame-speed correlation for laminar flow and Zimont flame speed closure model for turbulent flow.
- To validate the numerical simulation results, experimental measurements for wave disc engine and rectangular channel are conducted using schlieren photography to track the absolute speed and structure of the flame and pressure sensor is mounted on the channel wall to record the pressure time-history during combustion process.

1.3 Thesis Outline

This dissertation is a compilation of experimental and numerical simulations aimed at understanding the pressure dynamics and the temporal development of flame structure in confined chambers. Chapter 2 gives an overview of the confined premixed flame, proposed mechanism for tulip flame formation and mass diffusion impact on the flame and pressure. Chapter 3 of the thesis provides a summary of the governing equations describing a incompressible reactive mixture of gases and reaction modeling for laminar and turbulent flame. Chapter 4 presents the experimental setup and method of measurements. A discussion of experimental and numerical simulation results for two-dimensional premixed flame as well as the mass and thermal diffusion impact on the flame structure and pressure time-history are presented in Chapter 5. Chapter 6 discusses the main elements of three-dimensional evolution of flame and flame generated flow in both WDE and rectangular channel. Finally, a conclusions from the present work and recommendation for the future studies are described in Chapter 7.

Chapter 2

LITERATURE REVIEW - CONFINED PREMIXED FLAME

The confined premixed flames represent 99% of practical combustion devices which recover heat released in furnaces or mechanical power in engines such as internal combustion engines, pulse detonation engines, the wave rotor and the wave disc engine (WDE). In addition, the study of both premixed flame spread and the explosion of reacting gases in confined spaces is relevant for safety in silos, mines, oil refinery, and petro-chemical processes Ogle, 2017. However, the analysis of confined flames is much complicated than freely propagating flames, mainly due to heat exchange with walls, flame-acoustic interaction, and complex geometry of combustion chambers. In the next sections, the main features of flame structure developed in a confined, curved and straight channels are reviewed from literature sources. The impact of diffusion transport and turbulence on the confined flame structure is also reviewed and discussed.

2.1 Dynamics of confined premixed flame

Constant volume (CV) premixed flame propagation usually associated with the formation of tulip flame which has a long and interesting history. This history began over eighty years ago when Ellis published an experimental study of premixed flame propagation inside a closed cylinder,

marking the start of a new era in premixed flame research Ellis (1928). Subsequent studies have shown that a premixed flame propagating in a channel of aspect ratio larger than approximately two (2) experiences essentially four phases that have been observed and reproduced in numerical and experimental studies Ponizy et al. (2014), Xiao et al. (2014b), Hariharan & Wichman (2014). These phases are shown in Fig. 2.1: (a) after ignition, the flame surface propagates spherically at constant flame speed; (b) a finger- shaped flame propagates axially away from the ignition source (spark) with rapidly increasing flame surface area; (c) a flame skirt is formed when the flame touches the sidewalls. The lateral parts of the flame skirt are annihilated by the cold sidewalls leading to a dramatic reduction in the flame surface area, and the flame propagation speed is decreased; (d) the flame subsequently flattens and begins to fold and finally develops into a tulip flame, which propagates to the end of the channel Xiao et al. (2012a), Xiao et al. (2013). A fifth stage, introduced and discussed in this work, is found in the numerical analysis and verified experimentally, is the slow extinction of the flame at the far wall by heat losses.

The evolution of the flame shape leads to an important question. What is the physical interpretation for the flame shape changes, especially the tulip flame, and which flow parameter is most responsible?

Many mechanisms have been proposed to answer this question by studying the key parameters involved in the flame morphology development and evolution. Some of the proposed mechanisms are: Darrieus- Landau and other combustion/heat transfer instabilities Gonzalez et al. (1992), Dunn-Rankin et al. (1988), Chomiak & Hou (1996), Matalon & McGreevy (1994), the interaction between flame and vortex motion generated on the burned gas side due to vorticity produced by the flame Matalon & Metzner (1997), Kiran et al. (2014), Xiao et al. (2013), the saddle point motion across the flame front Hariharan & Wichman (2014), quenching of the flame by the sidewalls and the viscous effect Ellis (1928), Starke & Roth (1986), Lewis & v. Elbe (1987). Most of these

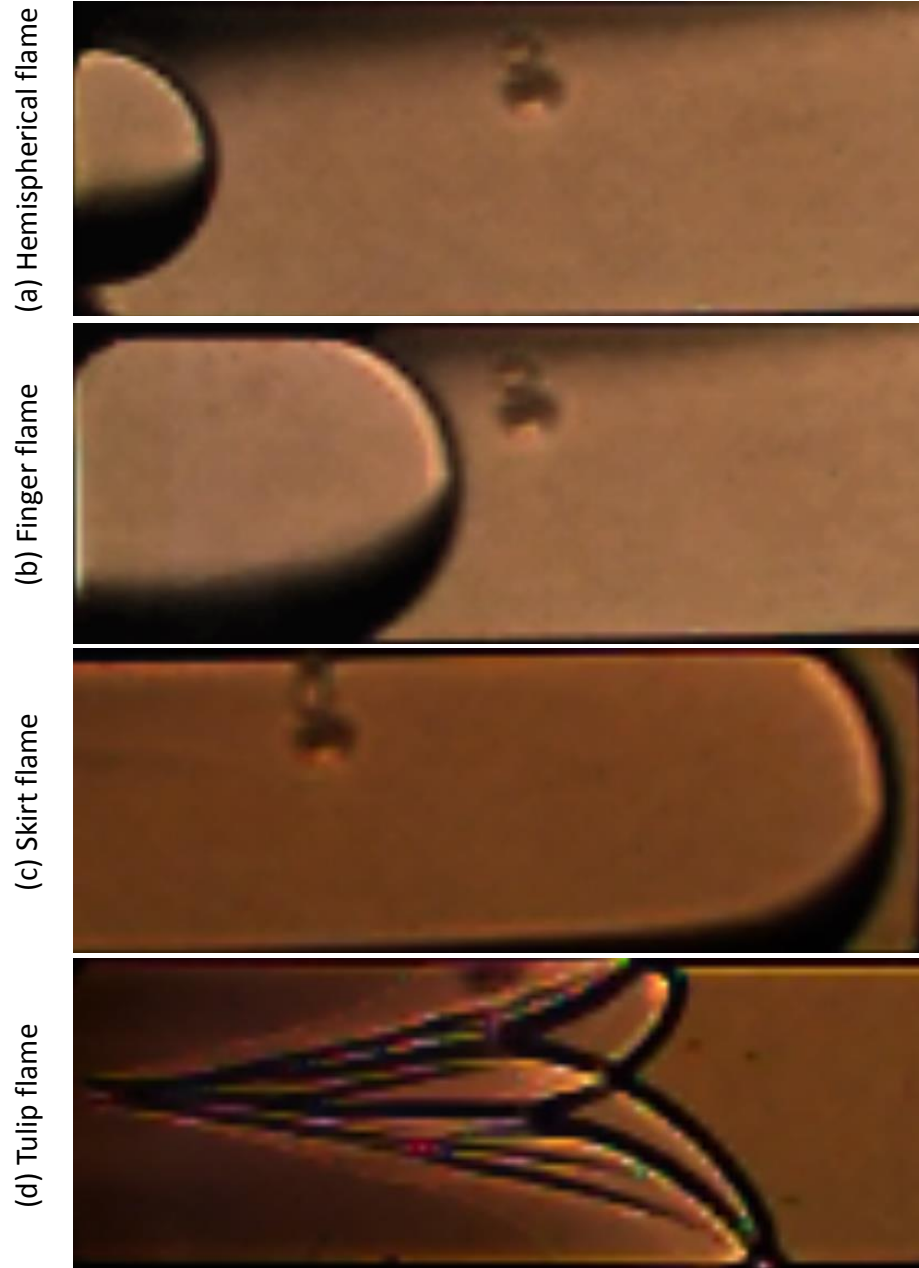


Figure 2.1: Sequence of flame phases developed in a rectangular channel.

studies were conducted using straight channels and tubes, which in some cases were open and partially open ended Clanet & Searby (1996). It is important to note that the notion of four stages of combustion ((a)-(d) above) was formalized by Clanet and Searby Clanet & Searby (1996), in whose work on open-ended tubes there was no flame quenching: our work has extended the num-

ber of flame stages to five. Concerning the fundamental science of the physics of flame evolution, there is currently no universally acknowledged dominant mechanism for tulip flame formation and evolution in a closed CV chamber. Furthermore, no flow or combustion parameter has been found directly responsible for the evolving flame shape. Thus it is not possible, to date, to neutralize this hypothetical effect in order to generate a confined premixed flame without showing the dramatic shape change from concave initial flame to convex tulip flame Ponizy et al. (2014). Nevertheless, the work of Hariharan & Wichman (2014), Zhou et al. (2006) and Ponizy et al. Ponizy et al. (2014) has made substantial progress toward this goal. It is instructive to quote from the latter: “It should be stressed... that the intrinsic instabilities of the flame front (Rayleigh-Taylor, Richtmeyer-Meshkov or Darrius-Landau) are not involved in this process (of flame front inversion). Indeed, the reverse flow which is responsible for the flame front inversion (concave to convex tulip) always starts in the zone close to the ignition point and not at the flame front.” Ponizy et al. (2014). These statements are supported by the work in Hariharan & Wichman (2014) which discusses in detail the manifestation of the various flame events in terms of the flow field topology, and specifically in terms of the characteristic saddle point, which propagates through the flow field as a geometric and temporal harbinger of flame front morphological change.

The mechanism of tulip flame formation and the other flame phases are important for combustion acceleration because the flame shape and surface area have a direct influence on the burning rate. Knowing how to increase the flame surface area under specific conditions is a key aspect of flame acceleration for an increased burning rate. The majority of previous studies were carried out using straight channels or tubes. However, the WDE chamber currently under investigation is shaped by two arcs of different radii (Fig. 4.2) and thus it is of interest to examine the channel curvature impact on flame dynamics. The study of premixed laminar flame propagation in a closed rectangular channel with a 90° bend has been carried out experimentally and numerically

by B. Zhou et al. Zhou et al. (2006). They observed a phenomenon they characterized as “flame shedding” when the flame propagated through the first 45° of the bend. The flame could generate a thrust force pushing the unburned gases forward, producing a flame-induced flow which appeared to be responsible for the tulip flame formation after the flame left the bend vicinity. The influence of mixture composition in hydrogen-methane-air on flames in a 90° pipeline with a high aspect ratio was experimentally investigated by Emami et al. Emami et al. (2013). The bend influences the fluctuation of flame speed and pressure, producing a potential hazard risk for the pipeline. Xiao et al. Xiao et al. (2014a) carried out an experimental and numerical study on a closed combustion tube with a 90° bend. The tulip flame that had developed in the straight channel section disappeared when it entered the channel bend where the lower tongue of tulip flame grew while the upper finger was annihilated. The convex tulip flame evolved, as in the current work, into a concave flame, although the evolution was not smooth.

Some general conclusions may be drawn from these studies: (1) The dynamics of premixed flames propagating in a closed CV chamber is a complex phenomenon that involves the mutually-interacting processes of fluid dynamics, heat transfer and chemical kinetics. No unique and certain mechanism has yet been proposed to explain tulip flame formation. (2) The bending of the combustion chamber has a critical influence on the flame dynamics; it may annihilate the tulip flame and convert it to a concave flame, while producing fluctuations in flame speed and pressure. (3) The previous literature indicates that there is a lack of work on the non-symmetrical confining chamber curvature effect on premixed flame dynamics. These effects can be found in many particular CV chambers like internal combustion engines or the WDE.

2.2 Molecular Diffusion Impact on Confined Premixed Flame

Recently, the numerical simulation has provided critical information about the dynamics of confined premixed flame. It was shown that a considerable discrepancy was observed in flame speed Smooke (2013), Liu et al. (2015), Bongers & De Goey (2003), flame extinction Williams (2001) Xin et al. (2015), Grcar et al. (2009), soot formation Dworkin et al. (2009), ignition condition Andac & Egolfopoulos (2007), Han & Chen (2015) and other flame characteristics when they are predicted by different diffusion models. This emphasizes the importance of diffusion model to accurately resolve the confined premixed flame characteristics. Ern and Giovangigli Ern & Giovangigli (1999) have numerically investigated the impact of multicomponent diffusion on counter flow and freely propagating laminar premixed methane/air and hydrogen/air steady flames using detailed reaction mechanism and three different diffusion models. It was shown that thermal diffusion has an obvious effect on hydrogen flame speed and no significant impact on methane flame. Higher peak temperature was obtained when the thermal diffusion is included while no significant impact of diffusion models on peak temperature. In another study, the effect of multicomponent and thermal diffusion on methane/air diffusion flame was numerically investigated using relatively detailed combustion mechanism (25 chemical reactions between 16 species). It was found that the multicomponent diffusion model predicts 8% larger flame length, 4% larger flame sheet thickness, and 5 K lower maximum flame temperature compared with simple Fick's law model Kleijn & Akker (1999). The contribution of thermal diffusion or Soret effect was also found to increase and reduce the stretched flame speed during early stages of flame propagation for light and heavy fuel, respectively Han & Chen (2015). It was shown that the multicomponent transport affects the flame extinction limit for both methane and hydrogen fuels. Another study by Grcar et al. Grcar et al. (2009) has shown that the multicomponent transport model in lean hydrogen-air flames predicted

“hotter, significantly faster flames with much faster extinction and division of cellular structures”. A comprehensive review by Hilbert et al. Hilbert et al. (2004) included more than 200 publications on turbulent flames with detailed chemistry and multidimensional diffusion model. This review study concluded that the impact of multicomponent diffusion model plays essential role on local flame structure especially for curved lean or rich freely propagating flames. The literature review indicates growing interest of using more elaborate diffusion model to provide further understanding of premixed flame; however, the computational cost of solving the multicomponent diffusion model seemed to be the main reason for making simple diffusion models e.g. constant Lewis and Schmidt number commonly used in combustion simulations Giacomazzi et al. (2007). It is instructive to quote from the latter that “these assumptions (of constant Lewis and Schmidt number) have never been theoretically justified nor verified in practical flame”, and hence it is important to investigate how much the main characteristics of unsteady premixed flame propagating in closed channel would deviate by using simple diffusion model of unity Lewis number and more elaborate multicomponent diffusion models including thermal diffusion? Since the overwhelming literature concerning the impact of diffusion model on premixed flame was focusing on turbulent and laminar diffusion flame configurations and little attention has obviously been given to multicomponent diffusion effects in confined premixed laminar flames. Part of this work is dedicated to provide further understanding on the impact of diffusion models and thermal diffusion on the dynamics of premixed stoichiometric flames propagating in two-dimensional, curved non-symmetrical closed channel.

2.3 Syngas Premixed Flame

synthesized gas (usually named syngas) is primarily a mixture of hydrogen and carbon monoxide mixed in different volumetric percentage with other diluents such as nitrogen (N_2), steam (H_2O), or carbon dioxide (CO_2). Syngas is one of the promising alternative fuel and environmentally clean source of renewable energy because it can be produced from variety of primary fuel sources such as biomass, coal, and hydrocarbon fuels and hence diversifying energy supply. The recent development in the integrated gasification combined cycle (IGCC) power plants have attracted considerable attention in syngas flame dynamics due to its industrial importance in reducing the CO_2 emission, and diversifying the power plant driving fuel such as biomass, hydrocarbons, and coal. Therefore, the syngas fuel plays a crucial role in facilitating carbon-free power generation using (IGCC) technology Zhang et al. (2016), Tuncer & Mendez-Vilas (2013). The adjustment of syngas compositions is highly depended on the primary fuel components and gasification processes. Therefore, the volumetric content of H_2 and CO in syngas fuels varies significantly according to the type of production processes, which in turn pose challenges in controlling the syngas flame behavior such as flashback, thermos-acoustic instabilities, NO_x emission due to drastic variation in chemical and transport properties as well as the laminar flame speed between hydrogen and hydrocarbon fuel. The other challenge is to design a fuel flexible, combustion chamber that can tackle the variability in syngas fuel compositions. This requires a solid knowledge about confined flame dynamics under wide range of mixture stoichiometry. Brambilla et al. (2015) reported a numerical and experimental investigation of syngas premixed flame in a 7 mm height mesoscale, open end channel at atmospheric pressure. Dinesh et al. (2016, 2015b,a) presented a DNS study about syngas flame propagation with high hydrogen content and different turbulent Reynolds number (50, 100, 150) at elevated pressure (1-4 bar). It is observed that the cellular flame structure of syngas is

highly depended on the elevated pressure under different initial turbulent conditions.

The present study undertakes a numerical investigation of premixed syngas flames propagating in a 2D, rectangular, closed channel of aspect ratio of 10 (10 *mm* in height \times 100 *mm* in length) for different stoichiometric ratio (0.7, 1.0, 1.5) and H_2/CO ratio (1:4, 1:1, 4:1). The dynamics of premixed syngas flame propagating in a closed channel has not been investigated in the literature. Among fundamental combustion parameters required to better understand the propagation of syngas burning, flame topology, pressure time-history, and burning rate are the most important since it directly related to industrial combustors.

2.4 Turbulent Premixed Flame

Generally speaking, turbulent flame definition comes from the change in flame structure as it propagates through turbulent flow field. Many experimental and numerical studies have proven that increasing turbulence level changes the flame structure from laminar smooth front to wrinkled, corrugated, stretched, thickened flame and end up with flame quenching when the Kolmogorov length scale becomes larger than the flame stretch limit Poinso & Veynante (2005). These observations were characterized by Damköhler (1947) and two distinct regimes have been identified based on the turbulence effect on the flame structure (Fig. 2.2):

1. Regime of large scale turbulence ($Da > 1$) where the flame is thinner than the Kolmogorov scale and the chemical time scale is shorter than the turbulent time scale ($Ka < 1$). The flame structure is wrinkled by turbulence motion but remains comparable to the laminar flame.
2. Regime of a small scale turbulence ($Da \ll 1$) in which the reactant and products are mixed by small turbulence eddies. The flame structure at this regime is usually referred as “well stirred reactor” or broken reaction zone Peters (2000).

A third regime, which is named “thickened flame regime” or “distributed reaction zones.”, was identified later in the regime of $K_a > 1$ and $Da > 1$ where the chemical time scale is shorter than the turbulent integral time scale but the flame thickness is larger than the Kolmogorov length scale. In this regime, the turbulence eddies interacts with the reactants and products transport and hence modifies the flame inner structure, more details can be found in Poinso & Veynante (2005), Glassman et al. (2015).

In the large scale turbulence regime, the flame is represented as a collection of small but finite laminar flame elements and propagate locally with the laminar flame speed. These thin layers are embedded within turbulent flow, one dimensional, time depended and strongly interact with flame-generated flow Peters (1988). Based on the flamelet concept, the reaction rate is obtained as the product of laminar flame speed, which depends on local pressure and temperature, and flame surface area density Bray & Cant (1991), Gülder & Smallwood (2007).

The definition of flame surface density here comes to simplify the difficulties associated with the temporal evolution of scalar surfaces embedded in turbulent flows, which are difficult to quantify directly Swaminathan & Bray (2011). Marble & Broadwell (1977) introduced the density of isosurface per unit volume which is defined at each Eulerian cube in the computational domain.

In this work, the temporal variation of mixture temperature and pressure on the premixed flame speed is incorporated with the algebraic flame surface density to estimate the reaction rate. The evolution of three-dimensional confined flame structure is studied for low turbulence intensities which is developed by flame-generated flow.

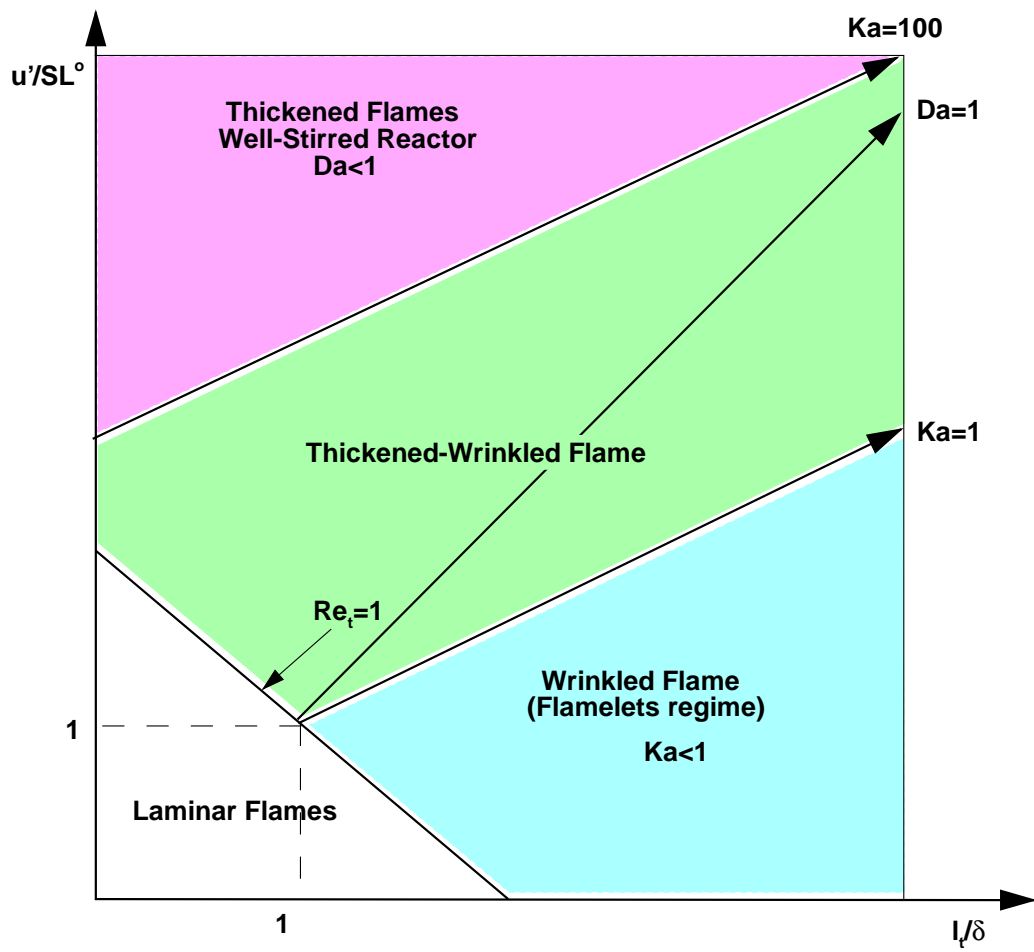


Figure 2.2: Modified turbulent flames regimes Poinso & Veynante (2005) and Peters (1999)

Chapter 3

GOVERNING EQUATIONS AND MODELING

The remarkable development of combustion science is gained by theory, experiment, numerical simulation and the combination between them. Over the past 60 years, the computer hardware and high-performance computational technologies have advanced significantly making the numerical simulation a truly competitive research tool with experiment and theory that provides invaluable information about the combustion phenomena. The computation of premixed flames in practical combustion chambers such as industrial furnaces, internal combustion engines and gas turbines chamber is, however, an expensive task and exceeds the current computational capabilities Smooke (2013); Kleijn & Akker (1999). This is due to; (1) a large number of species and chemical reactions required for combustion mechanism of the hydrocarbon fuels; (2) the difficulties arising from turbulence-flame interaction; (3) a wide range of time scales and strong coupling between chemical reactions, diffusion and transport, and flow dynamics result in very stiff differential equations, (4) the mixture properties are strong function of temperature which varies with time in constant volume combustion.

3.1 Laminar Premixed Flames

The modeling of laminar premixed flame is of critical importance because it represents the foundation and elementary blocks of the turbulent flames, which exists in the majority of industrial chambers. Under the concept of flamelet assumption, for example, the turbulent flame can be presented as a collections of stretched, thin, one-dimensional, laminar flamelet embedded within turbulent flow field Williams (1975), Peters (1988). Furthermore, both laminar and turbulent flames produce the same adiabatic flame temperature and pressure which is critical for industrial combustion chambers. However, the confined premixed flame propagation relies on a complex physical phenomena that involves; (1) complex combustion chemistry represented by hundreds of chemical reactions between typically 30-50 of chemical species for simple hydrocarbon fuel; (2) the reaction zone reside within very narrow space of order (0.1 mm) which required fine computational grids to capture the rapid change in mixture compositions and properties; (3) complex multi-physics phenomena and inherently multidimensional which involves stiff numerical equations due to wide range of time scale for chemical reactions, diffusion, and fluid dynamics; (4) a huge temperature gradient requires the thermo-chemical and transport properties to be represented as a strong function of local temperature Smooke (2013); Kleijn & Akker (1999). For these reasons, the three-dimensional systems with detailed chemistry and complex diffusion model are well beyond our current computational ability. In this section, the governing equations are presented for laminar confined premixed flame propagating in two-dimensional channel.

$$\frac{\partial \rho}{\partial t} + \nabla \cdot \rho \mathbf{u} = 0 \quad (3.1)$$

$$\frac{\partial \rho \mathbf{u}}{\partial t} + \nabla \cdot \rho \mathbf{u} \mathbf{u} = \nabla \cdot \mathbf{S} + \mathbf{f} \quad (3.2)$$

$$\frac{\partial \rho e}{\partial t} + \nabla \cdot (\mathbf{u}(\rho e + p)) = \omega_T + \nabla \cdot (\mathbf{u} \cdot \mathbf{S}) - \nabla \mathbf{q} + \mathbf{u} \cdot \mathbf{f} \quad (3.3)$$

$$\frac{\partial \rho Y_k}{\partial t} + \nabla \cdot \rho \mathbf{u} Y_k = \nabla \cdot \mathbf{J}_k + \omega_k, \quad k \in \mathbb{S}[1 \dots N_s] \quad (3.4)$$

$$p = \frac{\rho R T}{M_m}, \quad M_m = \left(\sum_{k=1}^{N_s} \frac{Y_k}{M_k} \right)^{-1} \quad (3.5)$$

$$\mathbf{S} = -p \mathbf{I} + \mathbf{T} \quad (3.6)$$

$$\mathbf{T} = \mu (\nabla \mathbf{u} + (\nabla \mathbf{u})^T) - \frac{2}{3} \nabla \cdot \mathbf{u} \mathbf{I} \quad (3.7)$$

$$\mathbf{q} = -\lambda \nabla T + \sum_{k=1}^{N_s} \rho \mathbf{u}_k Y_k h_k = -\lambda \nabla T + \sum_{k=1}^{N_s} \rho \mathbf{u}_k Y_k \int_{T_o}^T c_{pk} dT \quad (3.8)$$

$$e = \sum_{k=1}^{N_s} Y_k h_k - \frac{p}{\rho} + \frac{1}{2} \mathbf{u} \mathbf{u} \quad (3.9)$$

The unknowns variables (primitive variable) in the governing equations are: $\mathbf{u} = (u, v, w)$, the mass average velocity vector of the gas mixture; T , temperature; P , pressure; Y_k , mass fraction of species $k, k \in \mathbb{S}[1 \dots N_s]$; and ρ , mixture density. The equations also contains other quantities of: t , time; e , specific energy defined in Eq. 3.9; \mathbf{T} , stress tensor based on the Newtonian fluid assumption defined in Eq. 3.7; \mathbf{q} , net energy crossing the control volume surface by the mechanisms of molecular conduction and diffusion of species k defined in Eq. 3.8; \mathbf{J}_k , diffusion flux defined in Eq. 3.19; u_k , diffusion velocity of species k , which will be discussed further in section 3.1.2; μ , mixture-average dynamic viscosity; and λ , mixture-averaged thermal conductivity.

The aforementioned two-dimensional, compressible Navier-Stokes equations for laminar pre-mixed flame are solved using a pressure-based solver in which the pressure and velocity are coupled using the SIMPLE scheme. Space is discretized using a second-order upwind scheme and the transient solution was advanced using a first order implicit scheme with dual time stepping.

3.1.1 Reaction rate - Kinetic Mechanism

The prediction of the net rate of heat released from premixed flame, ω_T , and other flame characteristics is a fundamental problem and one of the remaining challenging issues in combustion modeling Smooke (2013). This requires a reliable design of detailed chemical-kinetics mechanism which is, for hydrocarbon combustion, usually required large number of chemical reactions between dozens of intermediate species that appears in fraction of mm and within fraction of millisecond and therefore required an expensive computational task Kiran et al. (2013), Mat-alon (2009), Xiao et al. (2015), Kleijn & Akker (1999). The combustion mechanisms used in this work are the San Diego combustion mechanism which consists 244 reactions between 50 species Chemical-Kinetic Mechanisms for Combustion Applications, San Diego Mechanism web page, Mechanical and Aerospace Engineering (Combustion Research), University of California at San Diego (2014), the DRM19 reduced mechanism based on GRI-Mech 1.2 which consists 84 elementary reactions between 19 species Frenklach & M. (1994), and H_2/CO syngas mechanism Kèromnès et al. (2013), see table 3.1.

Mechanism	Type	No. Species	No. reactions
San Diego Mechanism	Detailed reaction mechanism	50	244
DRM19	Reduced from GRI-Mech 1.2	21	84
Syngas H_2/CO	Detailed Mechanism	15	48

Table 3.1: Chemical-Kinetic Mechanisms used in this work.

The heat release due to chemical reaction, ω_T , is the highest term in the energy equation within the reaction zone and it is responsible for temperature rising hence no indices is needed for this term so as the temperature for all mixture components. The heat released is determined based on the sum of mass creation or destruction of each species multiplied by the associated energy

released or absorbed as follow:

$$\dot{\omega}_T = - \sum_{k=1}^{N_s} \Delta h_f^o M_k \dot{\omega}_k \quad (3.10)$$

$$\dot{\omega}_k = - \sum_{i=1}^{N_r} (v''_{kj} - v'_{kj}) Q_j \quad (3.11)$$

$$Q_i = K_{fj} \prod_{k=1}^{N_s} [X_k]^{v'_{kj}} - K_{rj} \prod_{k=1}^{N_s} [X_k]^{v''_{kj}} \quad (3.12)$$

$$K_{fj} = A_{fj} T^{\beta_j} \exp\left(-\frac{E_j}{RT}\right) \quad (3.13)$$

$$\frac{K_{fj}}{K_{rj}} = \left(\frac{P_{atm}}{RT}\right)^{\sum_{k=1}^{N_s} (v''_{kj} - v'_{kj})} \exp\left(\frac{\Delta S_k^o}{R} - \frac{\Delta H_k^o}{RT}\right) \quad (3.14)$$

$$\frac{\Delta S_j^o}{R} = \sum_{k=1}^{N_s} (v''_{kj} - v'_{kj}) \frac{S_k^o}{R} \quad (3.15)$$

$$\frac{\Delta H_j^o}{RT} = \sum_{k=1}^{N_s} (v''_{kj} - v'_{kj}) \frac{H_k^o}{RT} \quad (3.16)$$

The quantities in the chemical model equations are: $\dot{\omega}_k$, molar production rate of species k ; M_k , molecular weight of species k ; Q_i , reaction rate of progress defined for each reaction $j, j \in \mathbb{R}[1 \dots N_r]$ that involve species k ; v''_{kj} , v'_{kj} , stoichiometric coefficients of products and reactants of species k in reaction j , respectively; K_{fj} , forward rate of reaction j constants, which is not really constant but rather strong function of temperature T as shown in the Arrhenius expression of Eq. 3.13, moreover, it depends on both temperature and pressure in the fall off reactions; K_{rj} , reverse rate of reaction j constants and it is estimated based on the thermodynamic equilibrium as shown in Eq. 3.14; A_{fj} , pre-exponential factor of reaction j ; β_j , temperature exponent of reaction j ; E_j , activation energy of reaction j ; S_k^o , and H_k^o , entropy and enthalpy of species k evaluated at temperature T and pressure P_{atm} and tabulated as polynomial coefficients in the thermochemical properties data file.

There are two common ways to satisfy the constrain of species mass conservation $\sum_{k=1}^{N_s} Y_k = 1$; the first one is to distribute the residuals all over the species mass fraction which is weighted by the species mass fraction; the second approach is to assume that the most abundant species (N_2 in this work) behaves as a dilute and its mass fraction is set to one minus the sum of all other species mass fractions as:

$$Y_{N_s} = 1 - \sum_{k=1}^{N_s-1} Y_k \quad (3.17)$$

The performance of the reaction mechanisms used in this work is tested by solving one dimensional, premixed, freely propagating flame speed for each mechanism and compared with available experimental data from literature, see Figs. 3.1, 3.2.

The effect of initial pressure, unburned temperature, and equivalence ratio on the laminar flame speed are also plotted to assess the sensitivity of combustion mechanisms, see Figs. 3.3, 3.4. The multicomponent diffusion and Soret effect were also included in this analysis. The chemical model is solved at the end of each time step using CHINEMKIN-CFD solver which performs the integration over all the chemical reactions at the associated species concentrations calculated by the flow solver.

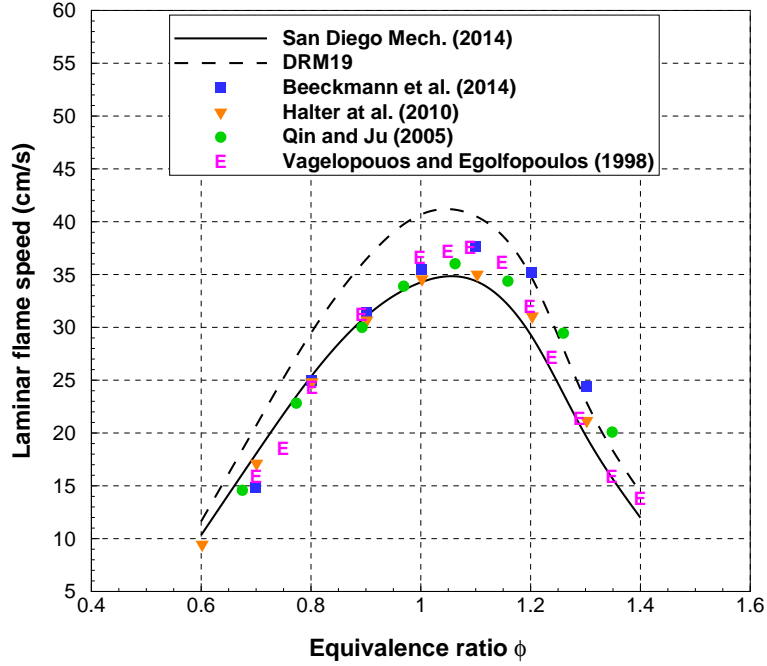


Figure 3.1: Flame speed predicted by San Diego kinetic mechanisms and tested against available experimental data from literature Beeckmann et al. (2014), Halter et al. (2005), Vagelopoulos & Egolfopoulos (1998), Qin & Ju (2005). The analysis consists one-dimensional free propagating, premixed flame.

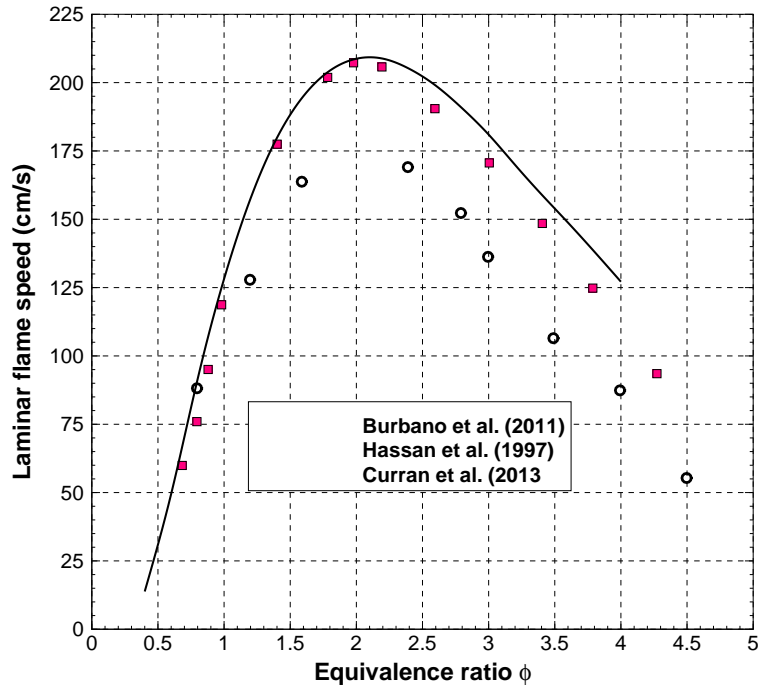


Figure 3.2: Laminar flame speed for syngas kinetic mechanism of Kèromnès et al. (2013) validated with available experimental data Hassan et al. (1997), Burbano et al. (2011).

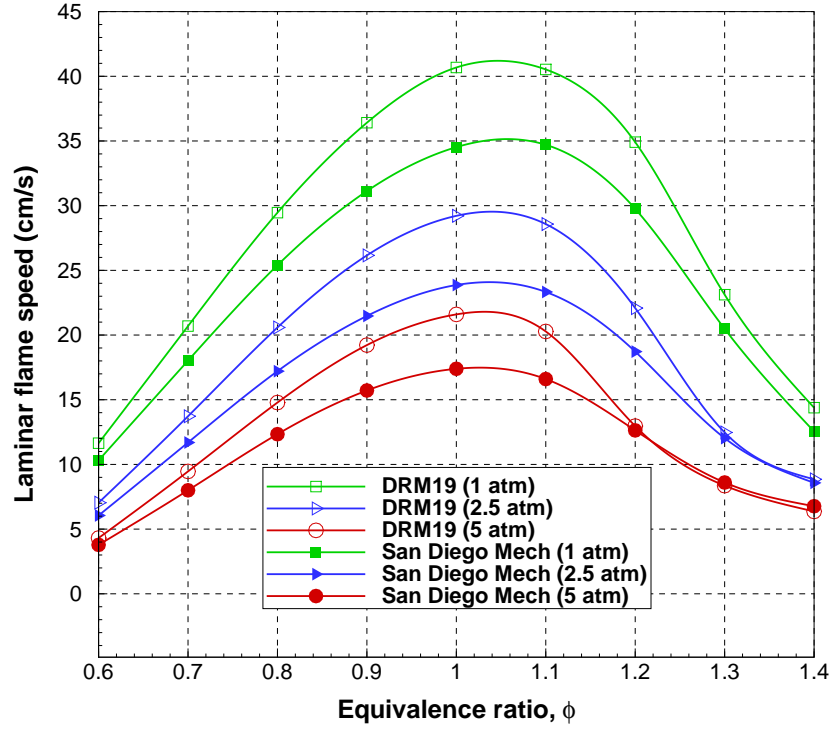


Figure 3.3: Laminar flame speed for DRM19, San Diego Mech. under different operating pressures.

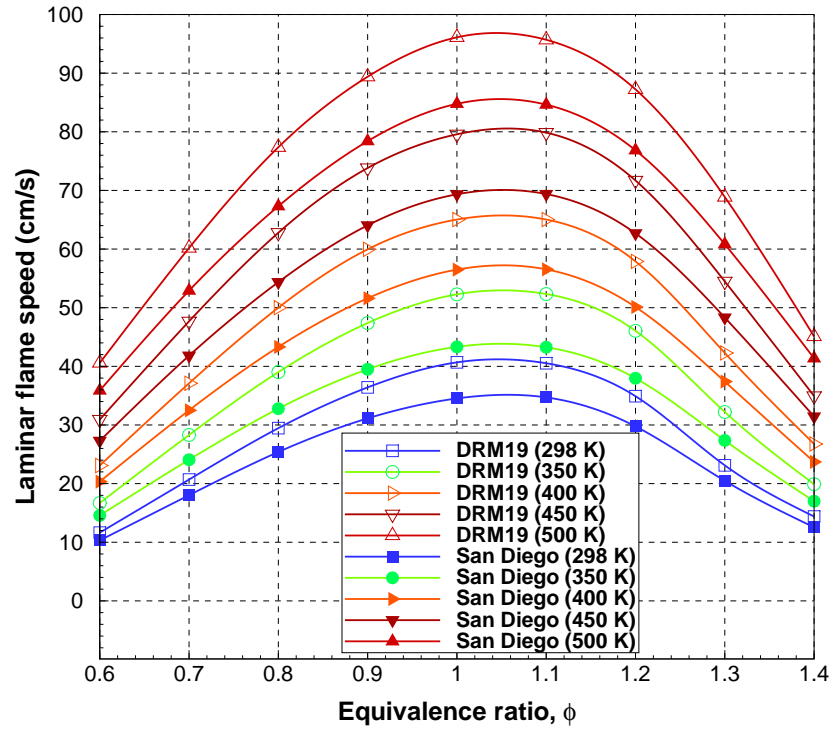


Figure 3.4: Laminar flame speed for DRM19 and San Diego Mech. under different reactants temperature.

3.1.2 Molecular diffusion

In multicomponent mixture, a species moves with diffusion velocity if there exist a gradient in species concentration, temperature, pressure or external force. The general expression for diffusion velocity can be written as:

$$V_k = - \sum_{l=1}^{N_s} \mathbf{D}_{kl} F_k - D_{T,k} \frac{\nabla T}{T} \quad (3.18)$$

Here the F_k is the driving force which takes into account the gradient of species concentration, pressure, and external force of being non-uniformly distributed over mixture species. \mathbf{D}_{kl} is the multicomponent diffusion coefficient of species k into species l , $D_{T,k}$ is the thermal diffusion coefficient of species k . In this work, the external forces acting equally on each species in the mixture. The driving force resulting from pressure gradient in the flow field is a differential effect that result from spatial fluctuation of pressure and becomes effective only when the molecular weight of the chemical species deviates considerably from the mean molecular weight of the mixture Smooke (2013), Grcar et al. (2009). The diffusion of species due to pressure gradient is usually small and negligible and hence is omitted in this study Vedachalam et al. (2015), Kleijn & Akker (1999). The second term in Eq. 3.19 refers to the thermal diffusion (Soret effect, thermophoresis, or thermodiffusion) in which the heavy and light molecules exhibit different response to the forces exerted by temperature gradient which increases the concentration of the heavy molecules on the cold side and light molecules on the hot side Eslamian (2012), Dworkin et al. (2009). Thus the resulting molecular mass flux J_k may be expressed by multicomponent extension of the Chapman-Enskog theory Bird et al. (2007):

$$\mathbf{J}_k = \rho_k V_k = - \sum_{l=1}^{N_s} \left(\rho \mathbf{D}_{kl} \nabla Y_k - D_{T,k} \frac{\nabla T}{T} \right) \quad (3.19)$$

The net of these driving potentials result in moving the species with a diffusion velocity V_k , which represent the core of diffusion problem that is traditionally known as extremely complicated since no explicit information is provided by kinetic theory for the diffusion transport coefficient but instead linear systems of diffusion equations whose dimension $N_s \times N_s$, which need to be solved on each computational grid point De Charentenay & Ern (2002). Therefore the modelling and computation of multicomponent diffusion is computationally expensive Smooke (2013), Giacomazzi et al. (2007), Giovangigli (2014). In recent years, a considerable progress has been made in simplifying the multicomponent diffusion models based on level of approximation, reduction mechanism, and improving the numerical algorithm for solving the resulting linear system Xin et al. (2015), Hilbert et al. (2004), Ern & Giovangigli (2008). Three different diffusion models depending on the level of approximation are used in this work; multicomponent diffusion of Chapman-Enskog model $M(I)$; mixture-averaged diffusion model $M(II)$; constant Lewis number diffusion model $M(III)$, to emphasis the effect of multicomponent diffusion model on flame structure evolution and pressure time history, see table 3.2.

Model	Formula	Description
$M(I)$	$D_{kl} = 0.010635 \frac{T^{3/2}}{p_s M_{kl}^{1/2} (\sigma_k + \sigma_l)^2 \Omega_E}$	a modified version of Chapman-Enskog model McGee (1991), Chapman & Cowling (1970). Thermal diffusion is included.
$M(II)$	$D_{km} = \frac{1 - X_k}{\sum_{j,j \neq k}^{N_s} X_j / D_{kj}}$	Mixture-average diffusion model based on Fickian model. No thermal diffusion was included.
$M(III)$	$D_{km} = \frac{\lambda_k}{\rho c_{pk} Le}$	Constant Lewis number. No thermal diffusion was included. $Le = 1.0$ for CH_4 /air mixture and $Le = 0.57$ for syngas/air mixture.

Table 3.2: Mass diffusion Coefficient for Multicomponent, mixture-average, and constant Lewis number.

The first model $M(I)$ is based on kinetic theory using the effective Lennard-Jones diameter $(\sigma_k + \sigma_l)/2$ which indicates the interaction characteristic length between k and l , and collision integral function $\Omega_E = \Omega_E(T^*)$, where, $T^* = T/(\varepsilon/k_B)_{kl}$, is the dimensionless temperature and ε_{kl} , k_B are the effective Lennard-Jones potential well depth for the collision and Boltzmann constant, respectively. The integral function Ω_E can be expressed as Reid & Sherwood (1966):

$$\Omega_E(T^*) = \frac{1}{(T^*)^{0.145}} + \frac{1}{(T^* + 0.5)^2} \quad (3.20)$$

$$\left(\frac{\varepsilon}{k_B}\right)_{kl} = \sqrt{\left(\frac{\varepsilon}{k_B}\right)_k \left(\frac{\varepsilon}{k_B}\right)_l} \quad (3.21)$$

The values of parameters, $(\sigma, (\varepsilon/k_B))$, are provided for each species k by the transport data file.

The thermal diffusion coefficient was found using composition-depended and empirical-based ex-

pression as Kuo (2005):

$$D_{Tk} = -2.59 \times 10^{-7} T^{0.659} \left[\frac{M_k^{0.511} X_k}{\sum_{k=1}^{N_s} M_k^{0.511} X_k} - Y_k \right] \left[\frac{\sum_{k=1}^{N_s} M_k^{0.511} X_k}{\sum_{k=1}^{N_s} M_k^{0.511} X_k} \right] \quad (3.22)$$

In the second model $M(II)$ we consider a binary diffusion between species k and mixture following Fick's law approximation where nitrogen contribute more than 70% of the mixture weight and hence we assume that the mixture diffusion coefficient are dominated by nitrogen diffusion coefficient. The third model $M(III)$ represent the simplest diffusion model which assumes that the thermal diffusivity is sufficient to know and equivalent to the diffusion coefficient. In other words, the case of unity Lewis number assumes that the speeds of heat and species diffusion are the same. The constant Lewis number case $M(III)$ is implemented by allowing the mass diffusivity to vary with the associated thermal diffusivity so that the Lewis number of each individual species remains equal and constant.

3.1.2.1 Lewis Number

Lewis number is defined as the ratio of thermal diffusivity of the unburned mixture to mass the mass diffusivity of the deficient reactant which represents the energy balance at the flame and hence it has a direct effect on the intrinsic thermodiffusive instabilities, extinction, and stretch effects on flames Poinso & Veynante (2005). For a mixture with single fuel component such as methane/air mixture, the Lewis number can be expressed as:

$$Le_m = \frac{\lambda}{\rho c_p D_{km}} \quad (3.23)$$

Here the thermal diffusivity of the unburned mixture and D_{km} is the mass diffusivity of the deficient reactant which represent the fuel component for lean mixture and oxidizer for rich mixtures. An-

other definition proposed by Matalon (2014) based on the weighted average of the individual Lewis numbers. Based on the former definition, the effective Lewis number for methane/air mixture can be written as:

$$Le_{eff} = \sum_{k=1}^{N_s} X_k Le_k \quad (3.24)$$

When the mixture consists more than one fuel component such as syngas which consists of two primary fuel, hydrogen and carbon monoxide, the estimation of the effective Lewis number is not trivial and still area of active research Bouvet et al. (2013), some of these approaches are:

1. Effective Lewis number based on the heat releases from fuel components Wu et al. (2011):

$$Le_Q = 1 + \frac{Q_{k_1}(Le_{k_1} - 1) + Q_{k_2}Le_{k_2}}{(Q_{k_1} + Q_{k_2})} \quad (3.25)$$

2. Linear effective Lewis number based on the volume fraction and Lewis number of the mixture fuel components Muppala et al. (2009), Bouvet et al. (2013):

$$Le_V = X_{k_1}Le_{k_1} + X_{k_2}Le_{k_2} \quad (3.26)$$

3. Effective diffusivity approach Dinkelacker et al. (2011):

$$Le_D = \frac{\alpha}{X_{k_1}Le_{k_1} + X_{k_2}Le_{k_2}} \quad (3.27)$$

where subscripts k_1 and k_2 represent the first and second component of the fuel, Q is the amount of heat released from the associated fuel component, X_k is the molar fraction of component k .

3.1.3 Gas properties

The propagation of premixed flame in closed chamber of isothermal walls is characterized by sequential change in flame speed and structure, mixture composition, pressure, and temperature for both burned and unburned gases which results in considerable variation in species thermochemical (c_p, S_k^o, H_k^o) and transport (μ, λ) properties of the individual species and consequently the mixture. The thermochemical properties of species are determined following CHEMKIN's polynomial format CHEMKIN-PRO 15131 (2013) whose coefficients are provided in the thermochemical data file. The mixture specific heat capacity at constant pressure is obtained based on mixing law of mass fraction which is commonly used in combustion modeling Kleijn & Akker (1999):

$$c_p = \sum_{k=1}^{N_s} Y_k c_{p_k} \quad (3.28)$$

The kinetic theory assuming the Lennard-Jones intermolecular potential energy is used to estimate the transport properties as (μ, λ) of pure species Kleijn & Akker (1999):

$$\mu_k = 2.67 \times 10^{-6} \frac{M_k T}{\sigma_k^2 \Omega_E} \quad (3.29)$$

$$\lambda_k = \frac{15}{4} \frac{R}{M_k} \mu_k \left(\frac{14}{15} \frac{c_p M_k}{R} + \frac{1}{3} \right) \quad (3.30)$$

An appropriate scheme using semiempirical formula, which was proved to be the most rigorous and satisfactory approach, is used to obtain mixture-average viscosity and thermal conductivity as Bird et al. (2007), Kleijn (1995):

$$\mu = \sum_{k=1}^{N_s} \frac{X_k \mu_k}{\sum_{l=1}^{N_s} X_l \phi_{kl}} \quad (3.31)$$

$$\lambda = \sum_{k=1}^{N_s} \frac{X_k \lambda_k}{\sum_{l=1}^{N_s} X_l \phi_{kl}} \quad (3.32)$$

Where ϕ_{kl} is dimensionless quantity and it can be expressed as:

$$\phi_{kl} = \frac{1}{\sqrt{8}} \left(1 + \frac{M_k}{M_l} \right)^{-\frac{1}{2}} \left(1 + \left(\frac{\mu_k}{\mu_l} \right)^{\frac{1}{2}} \left(\frac{M_k}{M_l} \right)^{\frac{1}{4}} \right)^2 \quad (3.33)$$

The parameters for kinetic theory (Lennard-Jones parameters) which account for intermolecular interaction, are taken from CHEMKIN transport data file.

3.2 Turbulent Premixed Flame

Since large computational resources are required for solving the reaction rate using detailed chemical kinetics, a considerable attention has been paid by the combustion community towards finding an alternative combustion model that is tractable and computationally affordable. One common approach that is used for premixed flames is to solve one transport equation for the reaction progress variable. However, replacing the expensive combustion mechanism comes with the price of losing information about essential quantities:

- The reaction rate which needs to be modeled in order to close the progress variable equation. This term remains a challenge and active area of research in the combustion modeling field. The majority of combustion community accept the definition for turbulent flames as a collection of small but finite laminar flame elements called *flamelet* Gülder & Smallwood (2007). Based on this assumption, the reaction rate can be approximated by the product of flame speed and flame surface area density Bray & Cant (1991).
- The diffusion coefficient of the reaction progress variable. Since no molecular informa-

tion about reaction progress variable can be provided and utilized to obtain the molecular diffusion, the kinematic information is used to estimate the diffusion coefficient under the assumption of high turbulent mixing intensity.

The challenge arising from modeling the reaction rate reside in the definition of the reaction rate itself which is the rate at which reactants are consumed at the flame surface. This obviously requires information about flame speed and the flame surface area which both currently represent a central problem in premixed flame modeling and it has been a subject of a large number of experimental and theoretical studies.

3.2.1 Large Eddy Simulation

The turbulent flows are characterized over wide a range of scales that extend from the largest scales, which are typically associated and comparable in size to the characteristic length of the mean flow, to the smallest scales, which are responsible for the dissipation of turbulence kinetic energy. Theoretically, it is possible to directly resolve the whole range of spatial and temporal scales of the turbulence flows using direct numerical simulation, in which no turbulence model is needed. However, the computational cost of DNS, which is proportional to $Re_t^{9/4}$, exceeds the current computational capabilities for practical engineering problem that involves high Reynolds number.

In LES technique, the large eddies, which depend on computational domain and boundary conditions of the flow, are resolved directly on the grid points, while the small scales, which are less dependent on the geometry and are consequently more *universal* and *isotropic*, are implicitly modeled using a subgrid-scale model. LES thus falls between DNS and RANS in terms of cost and accuracy because it resolves some range of turbulence scales and models the rest, see Fig. 3.5.

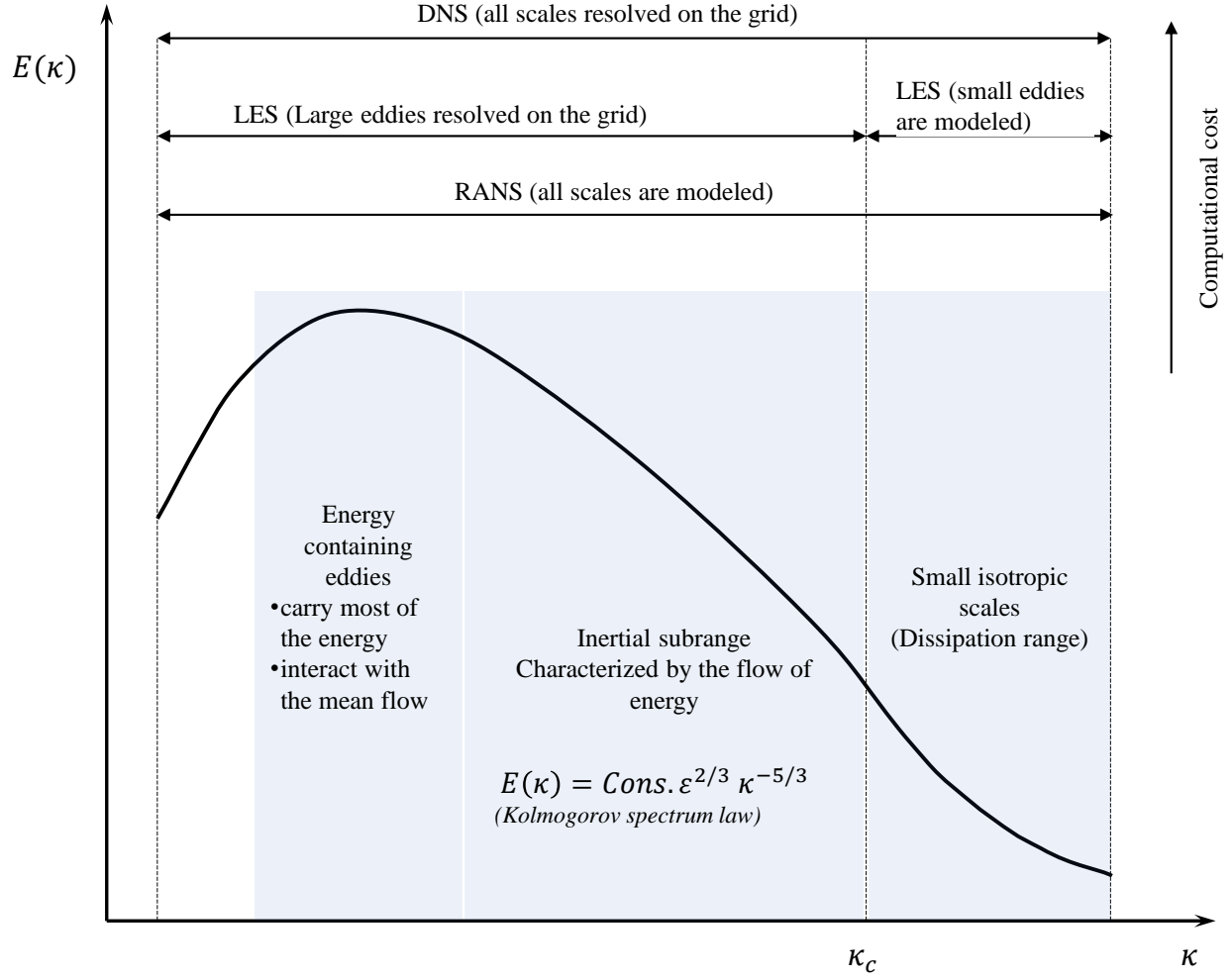


Figure 3.5: Turbulence energy spectrum regimes

3.2.1.1 LES filtering

In the large eddy simulation technique, the large and small scales fields are separated by filtering the governing conservation equations. One of the commonly used filters is the box filter, which is weighted averaging for a given volume of the physical space, and the spectral cut-off filter in which the quantities greater than a given cut-off frequency are truncated Pope (2000). The spatial filtered quantity $\tilde{\phi}$ can be expressed as:

$$\tilde{\phi}(x_i) = \int_{\Omega} \phi(x'_i) G(x_i, x'_i) dx'_i, \quad (3.34)$$

Where G is the LES filter function. For box in the physical space, the filter function G can be defined as:

$$G(x_i) = \begin{cases} \frac{1}{\Delta^3}, & \text{if } |x_i| \leq \Delta/2, \\ 0, & \text{otherwise,} \end{cases} \quad (3.35)$$

For Gaussian filter:

$$G(x_i) = \frac{6}{\pi\Delta^2} \exp(-6|x_i|/\Delta^2). \quad (3.36)$$

For spectral cut-off filter:

$$G(x_i) = \begin{cases} 1, & \text{if } \kappa \leq \kappa_c, \\ 0, & \text{otherwise,} \end{cases} \quad (3.37)$$

Where $i = 1, 2, 3$. and Δ is the filter width. The density-averaged (or Favre) filtering operator is incorporated here so that $\tilde{\phi}(x_i) = \frac{\bar{\rho}\phi}{\bar{\rho}}$.

3.2.1.2 Filtered Conservation Equations

The low-Mach number, Navier-Stokes equations are spatially filtered:

$$\text{Mass} \quad \frac{\partial \bar{\rho}}{\partial t} + \frac{\partial (\bar{\rho} \tilde{u}_i)}{\partial x_i} = 0. \quad (3.38)$$

$$\text{Momentum} \quad \frac{\partial}{\partial t} (\bar{\rho} \tilde{u}_i) + \frac{\partial}{\partial x_j} (\bar{\rho} \tilde{u}_i \tilde{u}_j) = \frac{\partial \sigma_{ij}}{\partial x_j} - \frac{\partial \tilde{p}}{\partial x_i} - \frac{\partial}{\partial x_j} (\bar{\rho} \widetilde{u_i u_j} - \bar{\rho} \tilde{u}_i \tilde{u}_j). \quad (3.39)$$

$$\text{Energy} \quad \frac{\partial}{\partial t} (\bar{\rho} \tilde{h}_s) + \frac{\partial}{\partial x_i} (\bar{\rho} \tilde{u}_i \tilde{h}_s) = \tilde{\omega}_T + \frac{\partial}{\partial x_i} \left(\lambda \frac{\partial \tilde{T}}{\partial x_i} \right) - \frac{\partial}{\partial x_i} (\bar{\rho} \widetilde{u_i h_s} - \bar{\rho} \tilde{u}_i \tilde{h}_s). \quad (3.40)$$

$$\text{Progress variable} \quad \frac{\partial}{\partial t} (\bar{\rho} \tilde{c}) + \frac{\partial}{\partial x_i} (\bar{\rho} \tilde{u}_i \tilde{c}) = \tilde{\omega}_k + \frac{\partial}{\partial x_i} \left(\bar{\rho} D_c \frac{\partial \tilde{c}}{\partial x_i} \right) - \frac{\partial}{\partial x_i} (\bar{\rho} \widetilde{u_i c} - \bar{\rho} \tilde{u}_i \tilde{c}). \quad (3.41)$$

$$\tilde{p} = \tilde{\rho} R \tilde{T} \quad (3.42)$$

where

$$\sigma_{ij} = \mu \left(\frac{\partial \tilde{u}_i}{\partial x_j} + \frac{\partial \tilde{u}_j}{\partial x_i} \right) - \frac{2}{3} \mu \frac{\partial \tilde{u}_l}{\partial x_l} \delta_{ij} \quad (3.43)$$

Here \tilde{u}_i is the filtered velocity component, \tilde{p} is the flow filtered pressure, \tilde{T} is the filtered temperature, $\bar{\rho}$ is the filtered density, \tilde{h}_s is the sensible enthalpy, \tilde{c} is the filtered reaction progress variable.

The subgrid terms are modeled based on the gradient diffusion approximation:

Subgrid-scale stresses:

$$\overline{\rho \tilde{u}_i \tilde{u}_j} - \bar{\rho} \tilde{u}_i \tilde{u}_j = -\mu_{SGS} \left(\frac{\partial \tilde{u}_i}{\partial x_j} + \frac{\partial \tilde{u}_j}{\partial x_i} \right) \quad (3.44)$$

Subgrid enthalpy flux term:

$$\overline{\rho (\tilde{u}_i \tilde{h}_s - \tilde{u}_i \tilde{h}_s)} = \frac{\mu_{SGS}}{Pr_{SGS}} \frac{\partial \tilde{h}_s}{\partial x_i} = \frac{\mu_{SGS}}{Pr_{SGS}} \frac{\tilde{c}_p}{Pr_{SGS}} \frac{\partial \tilde{T}}{\partial x_i} \quad (3.45)$$

Subgrid scalar flux term:

$$\overline{\rho (\tilde{u}_i \tilde{c} - \tilde{u}_i \tilde{c})} = \frac{\mu_{SGS}}{Sc_{SGS}} \frac{\partial \tilde{c}}{\partial x_i} \quad (3.46)$$

Here Pr_{SGS} is the subgrid Prandtl number equal to 0.85.

The compressible Navier-Stokes equations were solved using a pressure-based solver in which the pressure and velocity are coupled using the SIMPLE scheme. Space is discretized using second-order scheme for pressure and a central differencing scheme for density, momentum, energy, and reaction progress variables. The transient formulation was advanced using a bounded second-order implicit scheme with dual time stepping ANSYS[®] Academic Research (2015).

3.2.1.3 Subgrid Scale Model

Since the flame structure dynamics showed no signs of high turbulence intensities Najim et al. (2015), Hariharan & Wichman (2014) the flow generated by the flame is of low turbulent intensities. This requires a turbulent model capable of handling low turbulent or even laminar flow region. The wall-adapting local eddy-viscosity (WALE) is used here to model the subgrid-scale viscosity μ_{SGS} because: (1) the model return zero subgrid-scale viscosity in the laminar zone which allows accurate treatment of laminar zones that are expected in this particular case where the premixed flame starts at quiescent mixture and laminar flame propagation is expected. (2) this model use implicit damping effect and hence predicts accurately the behavior near-wall flow which becomes important in confined flame propagation μ_{SGS} Nicoud & Ducros (1999). The wall-adapting local eddy-viscosity is expressed as:

$$\mu_{sgs} = \rho L_s^2 \frac{\left(S_{ij}^d S_{ij}^d\right)^{3/2}}{\left(\tilde{S}_{ij} \tilde{S}_{ij}\right)^{5/2} + \left(S_{ij}^d S_{ij}^d\right)^{5/4}} \quad (3.47)$$

$$S_{ij}^d = \frac{1}{2} \left(\left(\frac{\partial \tilde{u}_i}{\partial x_j} \right)^2 + \left(\frac{\partial \tilde{u}_j}{\partial x_i} \right)^2 \right) - \frac{1}{3} \delta_{ij} \left(\frac{\partial \tilde{u}_i}{\partial x_i} \right)^2 \quad (3.48)$$

$$\tilde{S}_{ij} = \frac{1}{2} \left(\frac{\partial \tilde{u}_i}{\partial x_j} + \frac{\partial \tilde{u}_j}{\partial x_i} \right) \quad (3.49)$$

$$\tilde{S}_{ij} = \frac{1}{2} \left(\frac{\partial \tilde{u}_i}{\partial x_j} + \frac{\partial \tilde{u}_j}{\partial x_i} \right) \quad (3.50)$$

$$L_s = \min \left\{ \begin{array}{l} C_w V^{1/3} \\ \kappa d \end{array} \right. \quad (3.51)$$

The model constant C_w is 0.325, the von Kármán constant κ , and the distance to the closest channel wall d .

3.2.2 Combustion Model- Flamelet Concept

In this work, for three-dimensional problem, the combustion is modeled by solving single transport equation for reaction progress variable in which the reaction rate is predicted using algebraic flame surface density and flame speed closure. The heat release, $\tilde{\omega}_T$, in the energy equation can be expressed as:

$$\tilde{\omega}_T = Q_{LHV} Y_f \tilde{\omega}_c \quad (3.52)$$

Where Q_{LHV} is the heat of combustion of the associated fuel and Y_f is the fuel mass fraction. The source term, $\tilde{\omega}_c$, in the transport equation for the progress variable, is dominant within the flame region (or brush) which can be recognized when the reaction progress variable changes from the state of the unburned zone ($c = 0$) to the state of burned zone ($c = 1$). Therefore, the gradient of the reaction progress variable represents the surface moving, relative to fresh gases, with flame speed (S_l) and at which the artificial reactants is burned. Since no flame exist when $c = 0$ and $c = 1$, it is convenient to search for the flame by using the Bray-Moss-Libby (BML) expression for RANS which involves the $c(1 - c)$ which gives zero everywhere except when c has a non-zero gradient. Later, this expression was modified by Boger et al. (1998) to be used for LES by introducing model constant and filter size $\beta c(1 - c)/\Delta$,

$$\tilde{\omega}_c = \rho_u S_l \tilde{\Sigma}_f = \rho_u S_l \left(4\beta \frac{\tilde{c}(1 - \tilde{c})}{\Delta} \right) \quad (3.53)$$

Here the flame surface density Σ_f , the LES filter width Δ , the model constant β is 0.2, the unburned gases density ρ_u , the flame speed closure S_l .

The term $4\beta\tilde{c}(1 - \tilde{c})/\Delta$ is known as algebraic flame surface area density because it has algebraic form to describe the flame surface area and it could be more complicated and requires a transport equation to account for turbulent flame stretching, flame dilatation, expansion of burned gas, normal propagation, and dissipation of flame area. Details about the transport equation for flame surface area density can be found in Veynante & Vervisch (2002); Swaminathan & Bray (2011).

3.2.2.1 Flame Speed Closure

The key to the modeling of premixed combustion is the flame speed closure which plays a crucial role in the prediction of the reaction rate. The flame speed depends mainly on the flow parameter and the laminar flame speed which is a function of the fuel concentration, equivalence ratio, unburned gases temperature, pressure, and thermochemical properties. Turbulence can also wrinkle the flame surface by large eddies or thicken the flame by small eddies. In constant volume combustion, the temperature and pressure unburned gases change during combustion time. To account for the variation in temperature and pressure of the unburned gases, an experimental correlation suggested by Metghalchi and Keck Metghalchi & Keck (1980) is incorporated in the flame speed equation.

$$S_l = S_{l_{ref}} \left(\frac{T_u}{T_{ref}} \right)^{\Psi_T} \left(\frac{p}{p_{ref}} \right)^{\Psi_P} (1 - 2.1Y_{dil}) \quad (3.54)$$

$$S_{l_{ref}} = \Theta_1 + \Theta_2(\phi - \phi_M)^2 \quad (3.55)$$

$$S_{l_{ref}} = \Theta_1 + \Theta_2(\phi - \phi_M)^2, \quad \Psi_T = 2.18 - 0.8(\phi - 1), \quad \Psi_P = -0.16 + 0.22(\phi - 1) \quad (3.56)$$

Here the reference laminar flame speed, S_{lref} , is evaluated at standards temperature (T_{ref}) and pressure (P_{ref}) for methane/air mixture. The dilution mass fraction Y_{dil} , the equivalence ratio ϕ , the flame speed S_l , the unburned gases temperature and pressure T_u and P , respectively.

To account for turbulence generated by the flame, the Zimont turbulent flame speed closure is used Zimont et al. (1998):

$$S_t = F_z u' D_a^{0.25} \quad (3.57)$$

Where the F_z is the model constant, u' is the root-mean-square (rms) velocity, and D_a is the Damköhler number which is the ratio between turbulent integral timescale to reaction rate timescales, $D_a = \frac{\tau_c}{\tau_l}$. Since the flame starts in quiescent mixture, the methodology here is to monitor the turbulence development and check after each time step by comparing S_t and S_l and choose the dominant one.

3.3 Boundary and Initial Conditions

3.3.1 Numerics

The mesh is one of the most important components of the numerical simulation. In our study, the mesh or grid was generated using ICEM-CFD and the cell size depends on the combustion modeling scheme and type of the reacting mixture. The mesh size and time step were first estimated by solving one-dimensional, freely propagating flame using the same chemical mechanism and multicomponent diffusion model with Soret effect included.

For stoichiometric methane/air mixture of the San Diego mechanism, the computational domain area for the WDE channel is 568.5 mm^2 and is discretized in space with a maximum cell size of 0.1 mm. The cell height next to the channel wall boundaries is 0.02 mm with a growth rate fac-

tor of 1.2, which generates 110,000 cells in the entire computational domain. This appeared to be sufficient to capture the premixed methane/air flame. For syngas premixed flame, the WDE channel is discretized in space into 277800 quadrilateral cells with maximum and minimum cell size of 0.05 *mm* and 0.011 *mm*, respectively, see Fig. 4.1. The two dimensional, rectangular channel (10 *mm* \times 100 *mm*) is discretized in space into 200000 quadrilateral cells with cell size of 0.07 *mm*. The time step size varies between $10^{-8} - 10^{-6}$ s. A mesh independence studies were conducted to ensure that the grid resolution is sufficient to capture the premixed flame propagating in initially quiescent and confined mixture, see Appendix. A.

For the three-dimensional model, the maximum and minimum grid size is 0.4 *mm* and 0.08 *mm* with inflation ratio of 1.2 near channel walls. The time step is also selected to maintain the Courant-Friedrichs-Lewy number (CFL) below 0.25. The cell size, reaction mechanisms, and other details are summarized in table. 3.3

Combustion Chamber	Combustion Model	Flow model	Mesh size	Time step size
WDE, 2D	CH_4 /air (Detailed kinetic mechanism, Chemical-Kinetic Mechanisms for Combustion Applications, San Diego Mechanism web page, Mechanical and Aerospace Engineering (Combustion Research), University of California at San Diego (2014))	DNS	0.1-0.02 <i>mm</i>	10^{-8} - $10^{-6}s$
WDE, 2D	CH_4 /air (Reduced DRM19, Kazakov & Frenklach (1994)) and H_2/CO /air (Detailed mechanism, Kèromnès et al. (2013))	DNS	0.05 <i>mm</i>	$10^{-7} - 5 \times 10^{-6}s$
Rectangular Ch, 2D	H_2/CO /air (Detailed mechanism, Kèromnès et al. (2013))	DNS	0.07 <i>mm</i>	$10^{-8} - 10^{-7}s$
WDE and rectangular Ch, 3D	Algebraic flame surface density and transient flame speed	LES	0.4-0.08 <i>mm</i>	$CFL < 0.25$

Table 3.3: Summary of CFD simulation cases.

Chapter 4

EXPERIMENT SETUP

4.1 Combustion Chambers

Two closed channels that serve as combustion chambers in this work; the WDE channel as depicted in Fig. 4.1 and rectangular channel which is commonly used in the literature (Fig. 4.3). The WDE channel sidewalls are formed by two circular arcs of different center position; the inner and outer arc are 76.3 mm and 87.6 mm , respectively. The inlet and outlet ports of the channel are generated by another two arcs of 100 mm and 200 mm , respectively. The channel depth is 20 mm and parallel to the line perpendicular to the plane of Fig. 4.1. More details about the WDE channel design and other WDE configuration can be found in Sun (2011), Kiran (2013). The channel was machined using computer numerical control (CNC) machining. The top and bottom sides of the chamber are closed along its depth by two optically accessible, temperature and pressure-resistant glass ceramic sheets which are necessary for our schlieren system as shown in Fig. 4.2. The size of the rectangular chamber is $38\text{ mm} \times 38\text{ mm} \times 279.6\text{ mm}$ which is manufactured in similar way as the WDE channel.

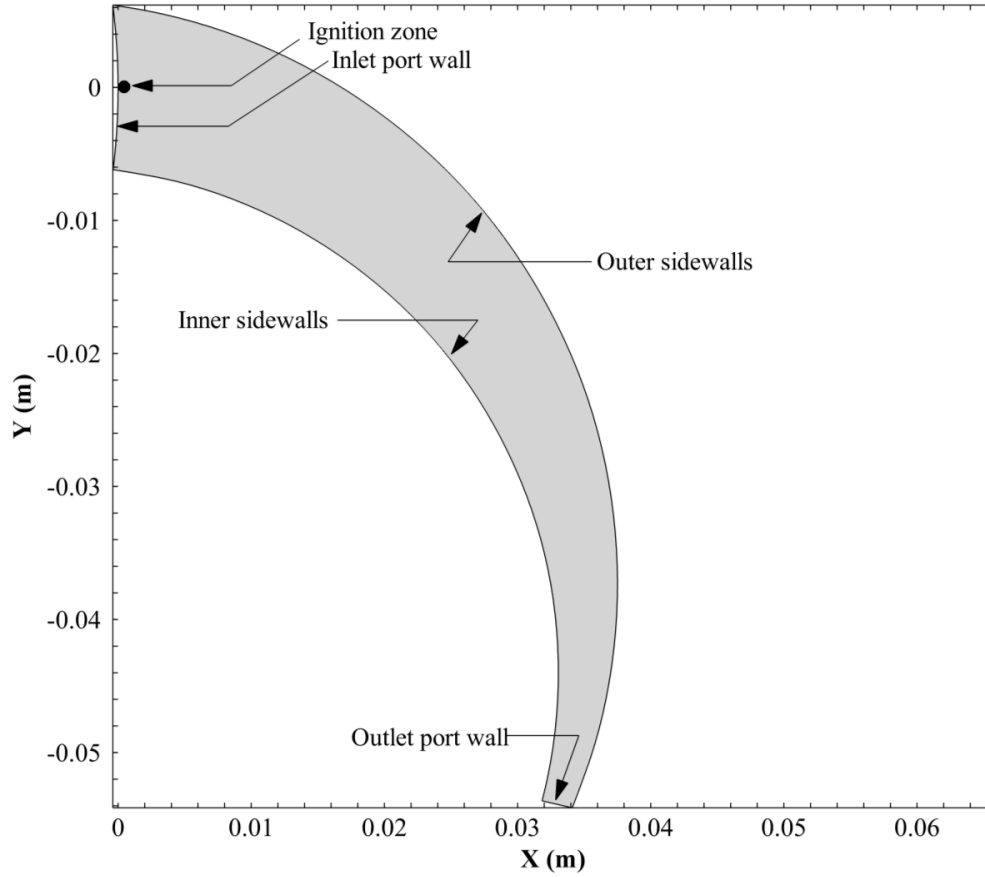


Figure 4.1: Schematic diagram of computational domain.

The combustion chambers are instrumented with two quick connectors isolating valves for inlet and outlet, spark plug, pressure sensor. The quick connectors valves are mounted on the channel sidewall and are used for evacuating, cleaning, charging and discharging the combustion chamber. The spark plug is located at the channel left wall (inlet port) as shown in Fig. 4.2.

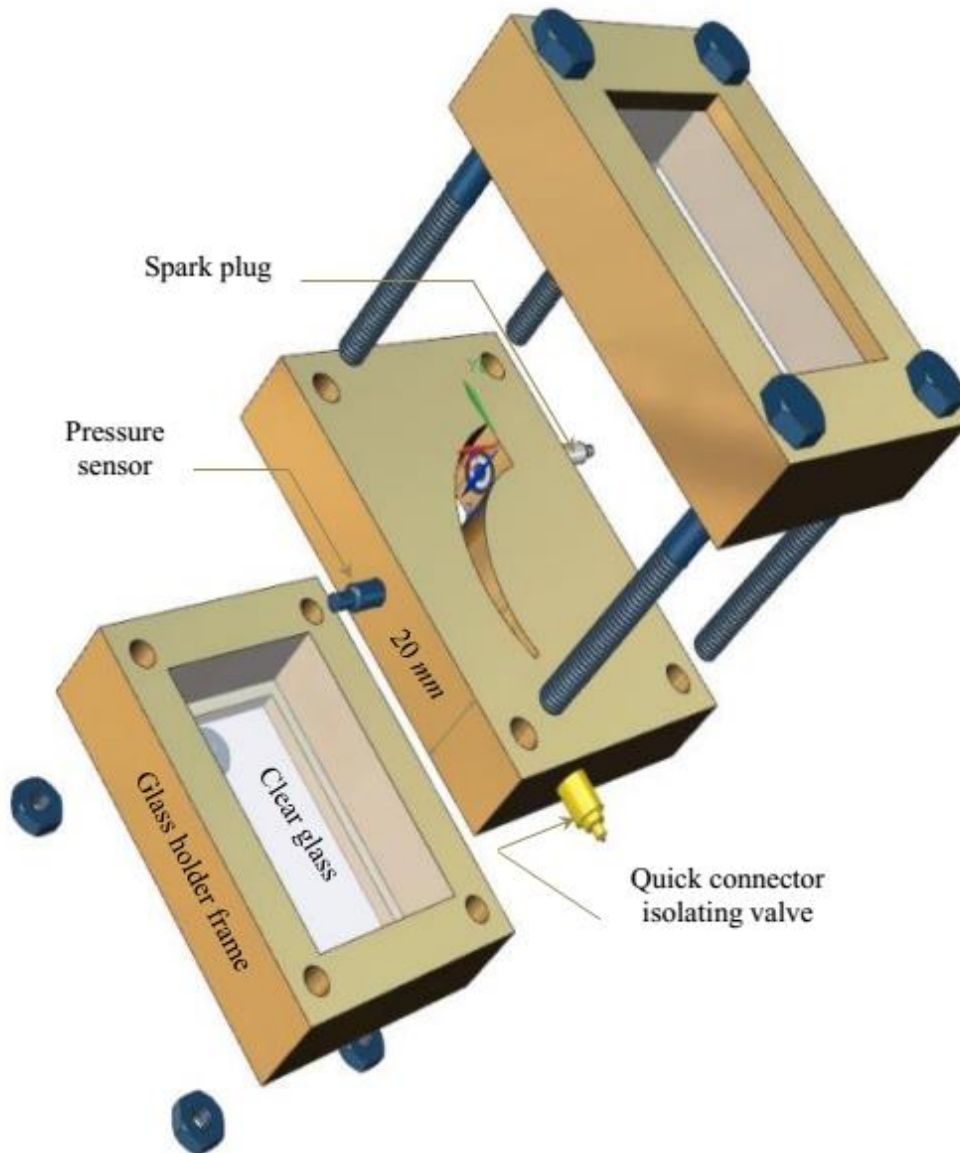


Figure 4.2: Schematic diagram of single wave disc engine channel used for experimental measurements

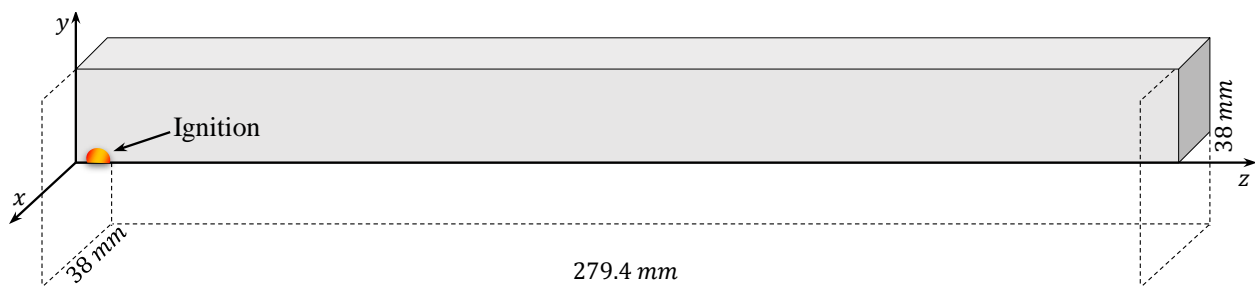


Figure 4.3: Closed rectangular channel serves as combustion chamber

4.2 Experiment Setup

Figure 4.4 shows a schematic diagram of the experimental setup. This is composed, firstly and most importantly, of the combustion chamber which are either the WDE channel or the rectangular channel that serve as the CV combustion chamber. In addition, a piezoelectric crystal Kistler pressure sensor (type 6052C) is connected to a Dual Mode Charge Amplifier (type 5010) to record the pressure-time history. The pressure sensor was calibrated as instructed in the manual and tested using available data from the literature Dunn-Rankin & Sawyer (1998), Kuzuu et al. (1996), see Figs 4.5, 4.6. The pressure sensor reading was sampled at a rate of 5 kHz . The flame propagation was captured using a z-type schlieren photographic system consisting of a high speed video camera (Photron FASTCAM SA4 500K-C1) operating at 3600 fps, a point light source, a knife edge, and two concave mirrors of 6" diameter and 60" focal length. A spark plug is flush mounted on the channel end wall. MSD Blaster is used to power the spark plug with 10 mJ of energy for every spark discharge.

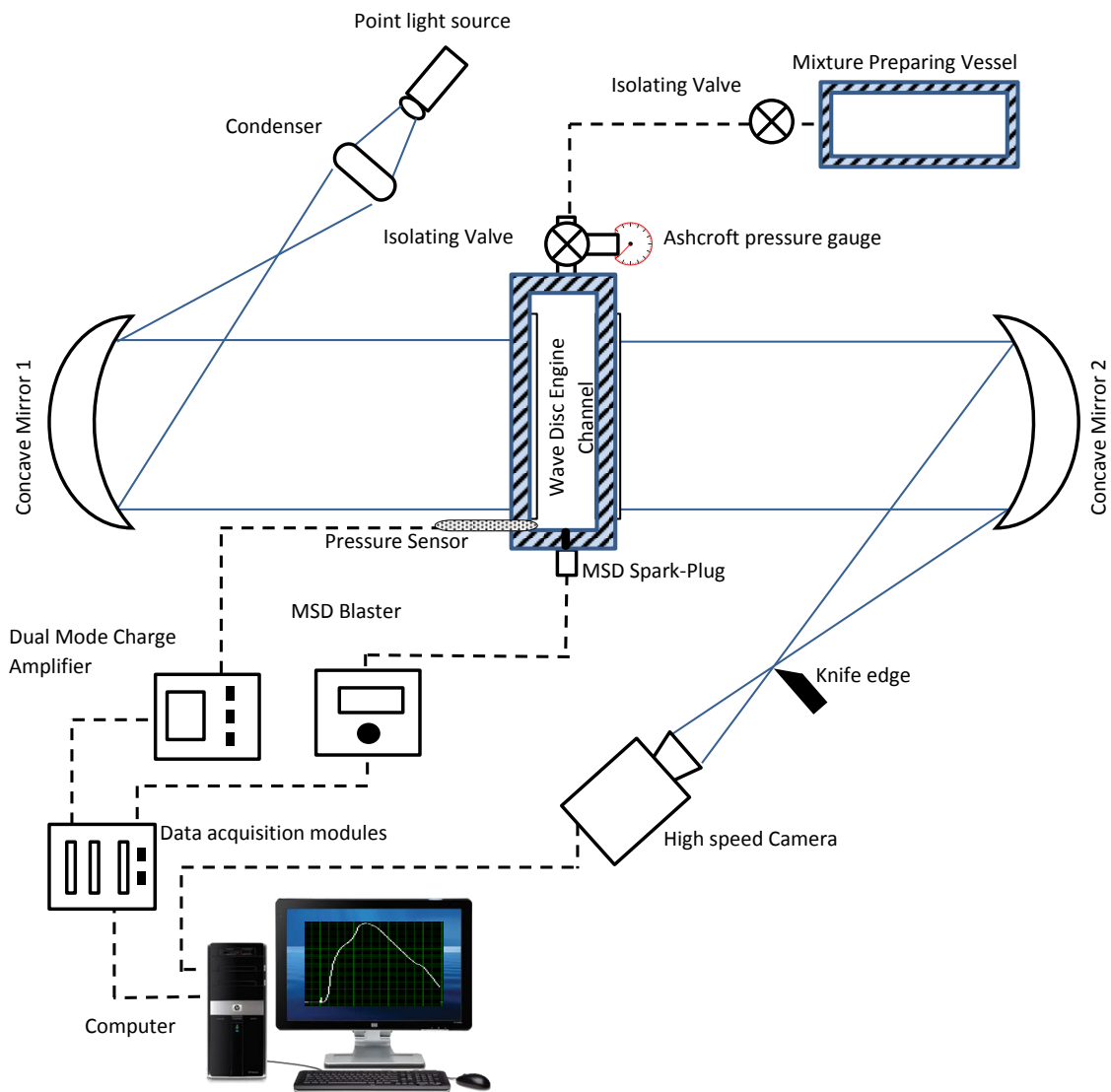


Figure 4.4: Schematic diagram of the experimental setup. The premixed flame images are measured at rate 3600 fps , and the pressure readings are sampled at 5 kHz .

4.3 Methods of Measurement

The experimental results discussed in this work were carried out for a stoichiometric methane-air mixture at initial temperature and pressure of 296 K and 102.65 kPa , respectively. The mixture was prepared in a separate vessel to ensure proper mixing using Dalton's law of partial pressures. The mixture was ignited using an MSD 10 mm spark plug mounted on a threaded hole through the center of the chamber inlet port. Ten (10) mJ of electrical energy was supplied to the spark-plug using an MSD Blaster coil. The experimental procedure was as follows:

- (1) Flush the channel with compressed air for 30 s to remove any combustion residuals remaining in the channel.
- (2) Evacuate the channel up to -720 mmHg (96 kPa) and then fill with combustible mixture. The remaining air inside the channel (5.325 kPa) was taken into consideration according to the following equation when the mixture was prepared:

$$P_{fuel} = (P_{air}^v + P_{air}^c) \frac{1}{\phi \psi_s} \frac{R_{fuel}}{R_{air}} \quad (4.1)$$

Here, ψ_s is the stoichiometric air to fuel ratio for methane, $\psi_s = 17.194\text{ kg air/kg fuel}$, R_{air} , and R_{fuel} are the gas constants for air and methane, respectively, $P_{air}^v, P_{air}^c, P_{fuel}$ are the absolute partial pressures for air in the vessel, chamber, and methane in the vessel, respectively, and ϕ is the equivalence ratio measured as kg fuel/kg air . For specific $(P_{air}^v + P_{air}^c)$ and ϕ , the partial pressure P_{fuel} was calculated using Eq. (3.1) and the methane was added to the vessel until the total mixture pressure of $P_{air}^v + P_{air}^c + P_{fuel}$ was attained.

- (3) A time delay of 30 s is employed before the spark-plug is activated in order to insure proper mixing and in order to eliminate any mixture motion inside the channel, thereby satisfying

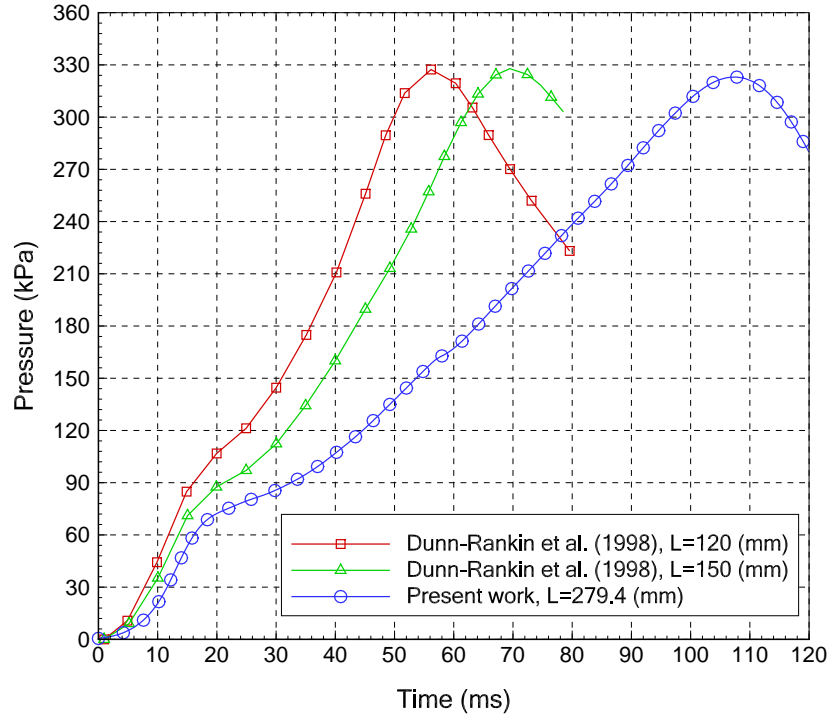


Figure 4.5: Pressure measurements tested against available data from literature Dunn-Rankin et al. (1988)

the initial quiescent mixture condition.

- (4) The high speed camera and pressure sensor is triggered shortly before spark-plug activation to initiate combustion. The data are recorded using a data acquisition system with a LabView interface.

To ensure the reproducibility of the flame structure and pressure dynamics, the quantity of mixture prepared in the vessel was sufficient for running eight (8) experiments. The experiments were reproducible and representative data are shown in Fig. 4.7.

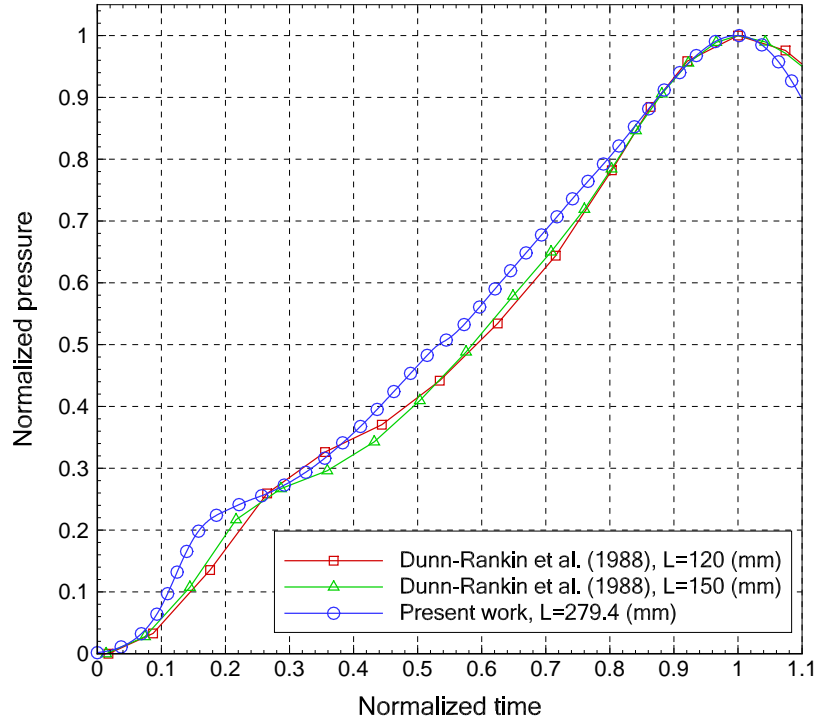


Figure 4.6: Normalized values of average pressure measurements for stoichiometric CH_4 / air flame.

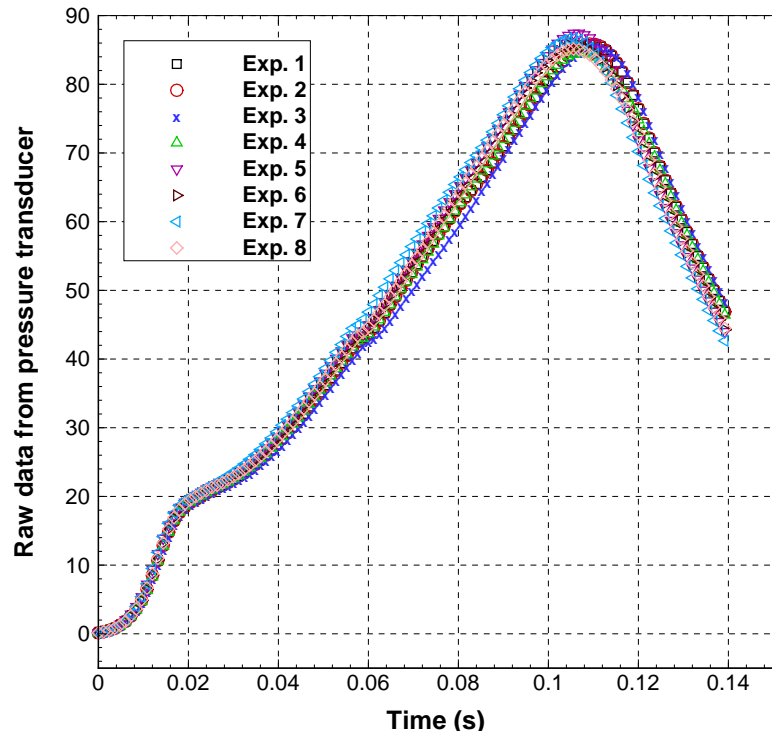


Figure 4.7: Raw data recorded by pressure transducer for eight(8) experiment to ensure the reproducibility of the tests.

Chapter 5

EXPERIMENTAL AND NUMERICAL SIMULATION

5.1 Flame Front Evolution

In this section, we present and discuss the dynamics of laminar premixed flames. The evolution of flame structure under different fuels, kinetics mechanism, diffusion models, and mixture stoichiometry is also discussed. The flame-induced flow, flame speed, average pressure and temperature developed in the WDE and rectangular channels are also inspected.

5.1.1 Non-symmetrical Tulip Flame

A numerical simulation of San Diego mechanism is conducted for two-dimensional WDE channel to understand the flame structure evolution in a non-symmetrical, curved channel. The transition of an ignition source to a concave finger flame to a convex “tulip” flame, and then the “tulip” once again into a concave flame under the WDE converging curvature effect of Fig. 4.2, represents an important transition process occurring for premixed flames in confined CV combustion. These characteristic flame features, along with the transition events generated by the combustor geometry of Fig. 4.2, are examined experimentally and numerically in this subsection.

Figure 5.1 shows the temporal sequence of the WDE flame propagation images. High-speed

schlieren experimental photographic images are shown on the left whereas mass fraction contours of HCO obtained from the numerical simulation to track the flame front are shown on the right. The color scale illustrates the flame structure evolution. Comparison of the images at the indicated times shows that the numerical scheme reproduced features of the flame that were recorded by high speed schlieren photography. The premixed flame exhibits different features than presented in the literature for straight channels Hariharan & Wichman (2014), Ellis (1928), Dunn-Rankin & Sawyer (1998) and channels with a 90° bend Ponizy et al. (2014), Emami et al. (2013), Xiao et al. (2014a).

Five main dynamic flame features or phases were recorded using schlieren photography that were also reproduced in numerical simulations. The first phase *I* starts after ignition in which the flame expands hemispherically with approximately constant flame propagation speed. This phase, which is brief and shows distinct signs of flame front acceleration soon after it begins, lasts in our study for only approximately 3 *ms*. We note that this time interval generally depends on how far the flame kernel is placed from the chamber walls, see Fig. 5.1a-Fig. 5.1d, and see Kiran et al. (2014), where the ignition kernel is located several *mm* from the wall and produces a distinctly non-spherical initial flame. Phase *II* takes place over the approximate time interval 3-5 *ms*, see Fig. 5.1d-Fig. 5.1c. The phase *II* flame propagates forward faster than toward the sidewalls while gaining surface area, which accelerates the flame. It is this phase that Clanet and Searby Clanet & Searby (1996) have characterized, using a very simple ad-hoc model, as having exponentially increasing flame speed. In phase *II* the chamber geometry (curvature) starts to impose itself by shaping the flame front, turning the flame front tip down toward the lower sidewall instead of forming a uniform finger-shaped flame that has been extensively reported for straight channels. When the flame skirt Clanet & Searby (1996) approaches the sidewalls, the trapped fresh mixture is consumed by the flame at a low rate due to the influence of viscosity

in the region near the wall and the even stronger influence of heat losses to the cold sidewalls. The viscous flow phenomenon has been referred to as “squish flow” Dunn-Rankin et al. (1988). Phase *III* appears during the approximate time interval 5-10 *ms*, where the lateral flame sides touch the lower sidewall before touching the upper wall and are gradually quenched. This results in a diminishment of the lateral part of the flame surface area leading to a deceleration of the flame front in laboratory coordinates. The flame is quenched on the inner sidewall faster than the outer sidewall because of the channel curvature effect, see Fig. 5.1e- Fig. 5.1f, in qualitative agreement with previous research on pipes and channels with 90° bends. Just after the lateral part of the flame is completely quenched at approximately 10 *ms*, phase *IV* begins. Here, the flame front continues to move along the inner wall faster than the flame close to the outer wall, while the flame in the middle region lags behind. This leads to the development of a non-symmetric tulip flame with its cusp pointing toward the burned gases, as shown in Fig. 5.1g- Fig. 5.1n. The flame tongue near the inner sidewall is longer with a rounded tip, while the upper flame tongue is much smaller. Over time, the inner flame tongue continues to grow by radially displacing the tulip flame cusp toward the outer sidewall, which action eventually consumes the upper flame tongue. As a consequence, the tulip flame diminishes during this time interval and completely disappears once the flame cusp touches the outer sidewall at approximately 17 *ms*. A concave propagating flame is thereafter reconstituted. The reconstitution of the concave flame, which is exhibited in the converged-curved channel, has not been reported in straight channels. In 90° channels, a similar process occurs, although the evolution is less clearly and smoothly exhibited than it is here for the gradual bend of our channel. Finally, phase *V* occurs when the flame is converted into a convex flame that subsequently experiences no major morphology changes until it approaches the channel end and extinguishes at the termination of combustion, at approximately 65 *ms* (Fig. 5.1o). This phase consumes approximately 75% of the combustion time, indicating

that the quenching phase occupies the bulk of the combustion time. In the beginning of this stage the mass consumption rate continues to increase. Near the end of combustion, at impending flame quenching, it finally plummets to its final value of zero. A theoretical and numerical analysis of premixed flame quenching for the plane flame/wall was carried out by Wichman and Bruneaux (1995).

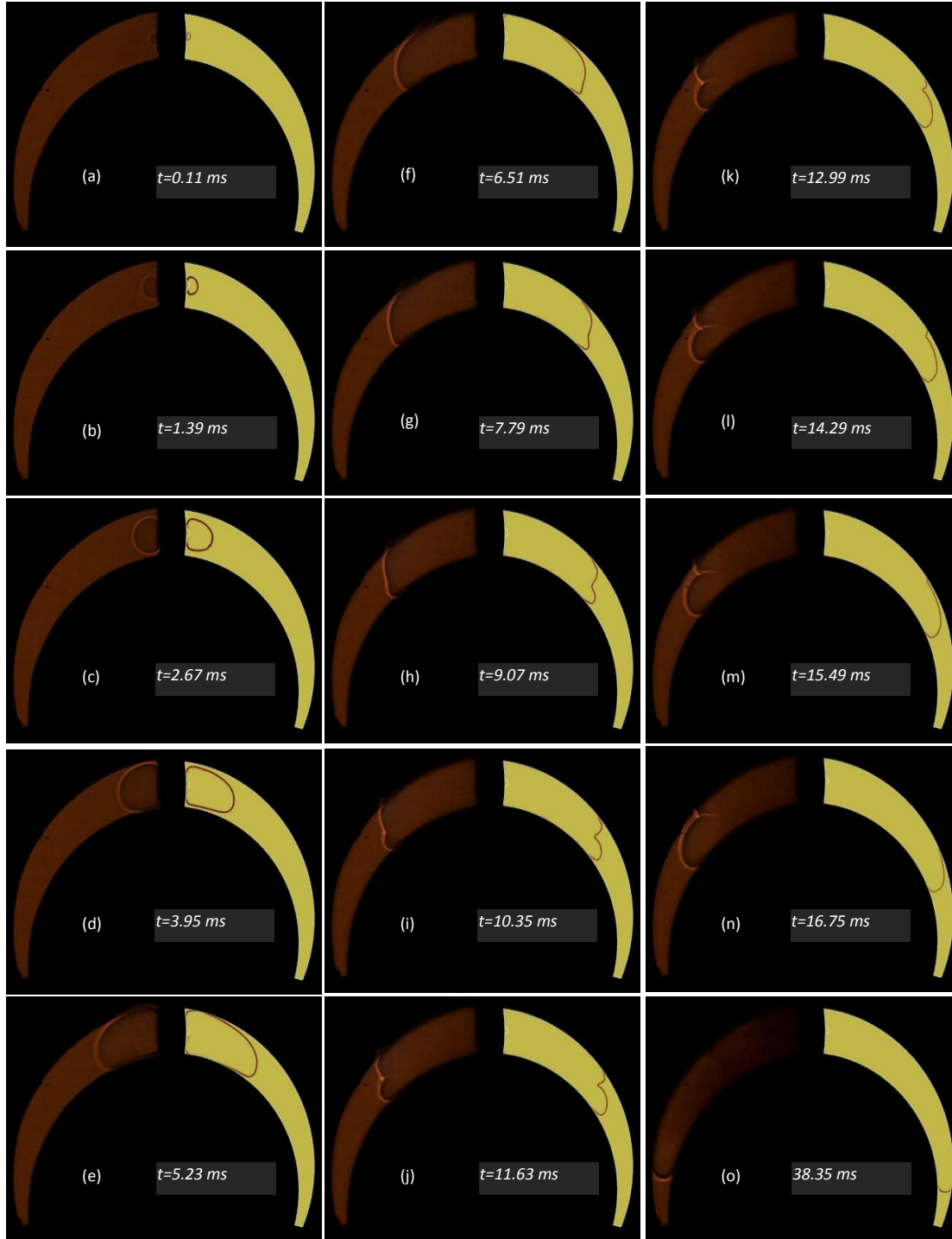


Figure 5.1: Evolution of the WDE confined premixed flame using schlieren photography (images on the left) and mass fraction contours of HCO , which serve to track the flame locus, from the numerical simulations (images on the right): (a-d) hemispherical expansion and evolution to a concave “finger” flame; (e) inner part of lateral flame touches the inner sidewall; (f) outer part of lateral flame touches the outer sidewall and flame front flattens; (g) initial formation of tulip flame cusp which generates the characteristic convex tulip flame shape; (h-k) inner flame tongue grows by radially displacing the flame cusp toward the outer sidewall ; (l) upper flame tongue disappears; (n-o) tulip flame converted to curved flame.

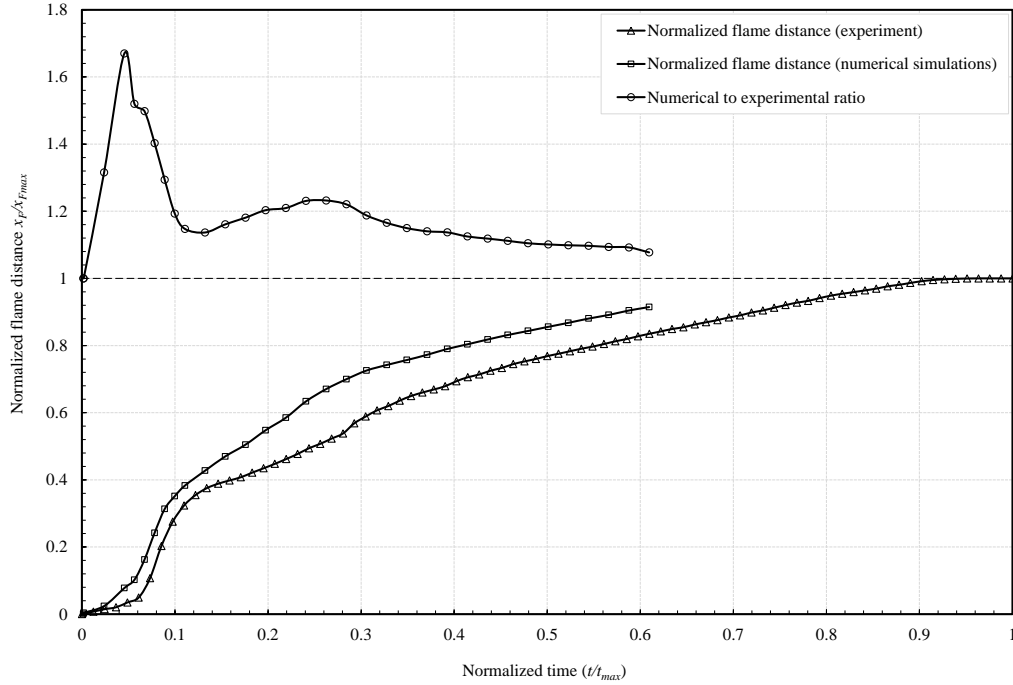


Figure 5.2: Comparison between the experimental and numerical simulations of the normalized flame locations X_F/X_{Fmax} . Also shown is the ratio of these normalized flame locations, showing that the numerical flame evolution is always faster than the experimental flame evolution.

The flame locations were determined from Fig. 5.1 and normalized by the length of mid-line between the inner and outer arcs of the channel X_F/X_{Fmax} and plotted versus normalized time t/t_{max} to provide a quantitative comparison between the experiment and the numerical simulation, see Fig. 5.2. The direct comparison between overall burn times and time differences between the various burning regimes (or phases) (I)-(V) indicates that the numerical evolution is always faster than the experimental evolution. A possible explanation is that despite the basic two dimensional appearance of the laboratory flame, it is a three dimensional entity with “side losses” of heat and radical species to the glass walls along the channel depth axis (see Fig. 4.2), in addition to having a possibly 3-D secondary flow structure.

5.1.2 Diffusion impact

5.1.2.1 Methane/air flame

In Fig. 5.3, the evolution of a premixed stoichiometric methane/air flame front in a curved closed channel is shown for the diffusion models $M(I)$, $M(II)$, $M(III)$ (on the left) and compared to a shadowgraph experiment (on the right). The models $M(I)$ and $M(II)$ produce miniscule discrepancies in flame position and structure. The largest discrepancy between $M(I)$ and $M(II)$ was during the accelerated finger flame stage, in which the flame rapidly adds surface area when the hydrodynamic effect of burned gas expansion is dominant. This occurs 3-5 *ms* after ignition (Figs. 5.3a-b, 5.4). When the lateral flames touch the cold sidewalls, $M(I)$ and $M(II)$ collapse and almost no discrepancy is seen between them through to the end of combustion. Thus, the mixture-average diffusion model is sufficient to describe combustion when air is the oxidizer and the multicomponent mixture is approximated as a binary mixture in which nitrogen is dominant.

Flame $M(III)$ deviates from $M(I)$ and $M(II)$ and lags behind them as early as 0.9 *ms* after ignition. This deviation grows with time and reaches a maximum shortly before the lateral $M(I)$ and $M(II)$ flames touch the sidewalls and decelerate (Fig. 5.3b-d). Since $M(I)$, and $M(II)$ initially propagate faster than $M(III)$, they touch the sidewalls and slow down before $M(III)$, which catches them to reduce the flame position discrepancy between them (see Figs. 5.3d-e, 5.4).

The evolution of the tulip flame inside a similar curved channel was investigated previously Najim et al. (2015). The lower tulip flame tongue for $M(I)$ and $M(II)$ start growing at around 9 *ms*, whereas the tulip flame lower tongue for $M(III)$ was observed at approximately 11 *ms* (see Figs. 5.3e-f). Similar to the previous work Najim et al. (2015), the lower tongue grows by displacing the tulip flame cusp toward the upper sidewall. This shrinks the upper tongue to convert the flame front again into a concave shape. One of the most pronounced differences in $M(III)$

is observed 11.8 *ms* when the growing lower tongue of $M(III)$ suddenly accelerates much faster than its counterparts $M(I)$ and $M(II)$ (Fig. 5.3f-g). At this time, the diminished upper tongue of $M(III)$ shows less rounding than its counterparts (Fig. 5.3g). The nature of the influence of the three diffusion models on the flame structure can be observed at about 15 *ms*. Here the dominant lower tongue of $M(III)$ decelerates and produces a second, smaller tulip flame while $M(I)$, $M(II)$ and the experiment flame remain concave and propagate slowly to the end of the channel (Fig. 5.3h-l). Like its predecessor, the second $M(III)$ tulip is annihilated when the flame cusp moves toward the upper sidewall. This shrinks the upper flame tongue and leaves behind a growing lower flame tongue. This evolves into a concave flame, which propagates (lags) behind $M(I)$ and $M(II)$ to the end of the channel (Fig. 5.3i-l). The $M(III)$ flame differs quantitatively and qualitatively from $M(I)$ and $M(II)$ as well as the experiments.

The flame distance is summarized in Fig. 5.4. Model $M(III)$ describes the premixed flame in the early stage to 11 *ms*, when the hydrodynamic phenomena associated with thermal expansion dominates. After 11 *ms*, $M(III)$ becomes unrealistic and fails to follow the experiment and models $M(I)$ and $M(II)$. In the experiment, the ignition produces an initial flame of diameter 5 *mm* whereas the numerical simulation ignition is modeled by patching an area of 2 *mm* diameter at the hot spot. To unify the results, the reference point for beginning the comparison of the experimental and numerical flame tip distance is chosen to be 5 *mm*.

The mixture-average model $M(II)$ predicts the flame speed and structure in good agreement with the elaborate multicomponent diffusion model $M(I)$. This agrees with the results of Ern and Giovangigli Ern & Giovangigli (1999) for a freely propagating flame. However, this result is confined to a stoichiometric methane/air mixture in which N_2 is 72.3% of the mixture weight.

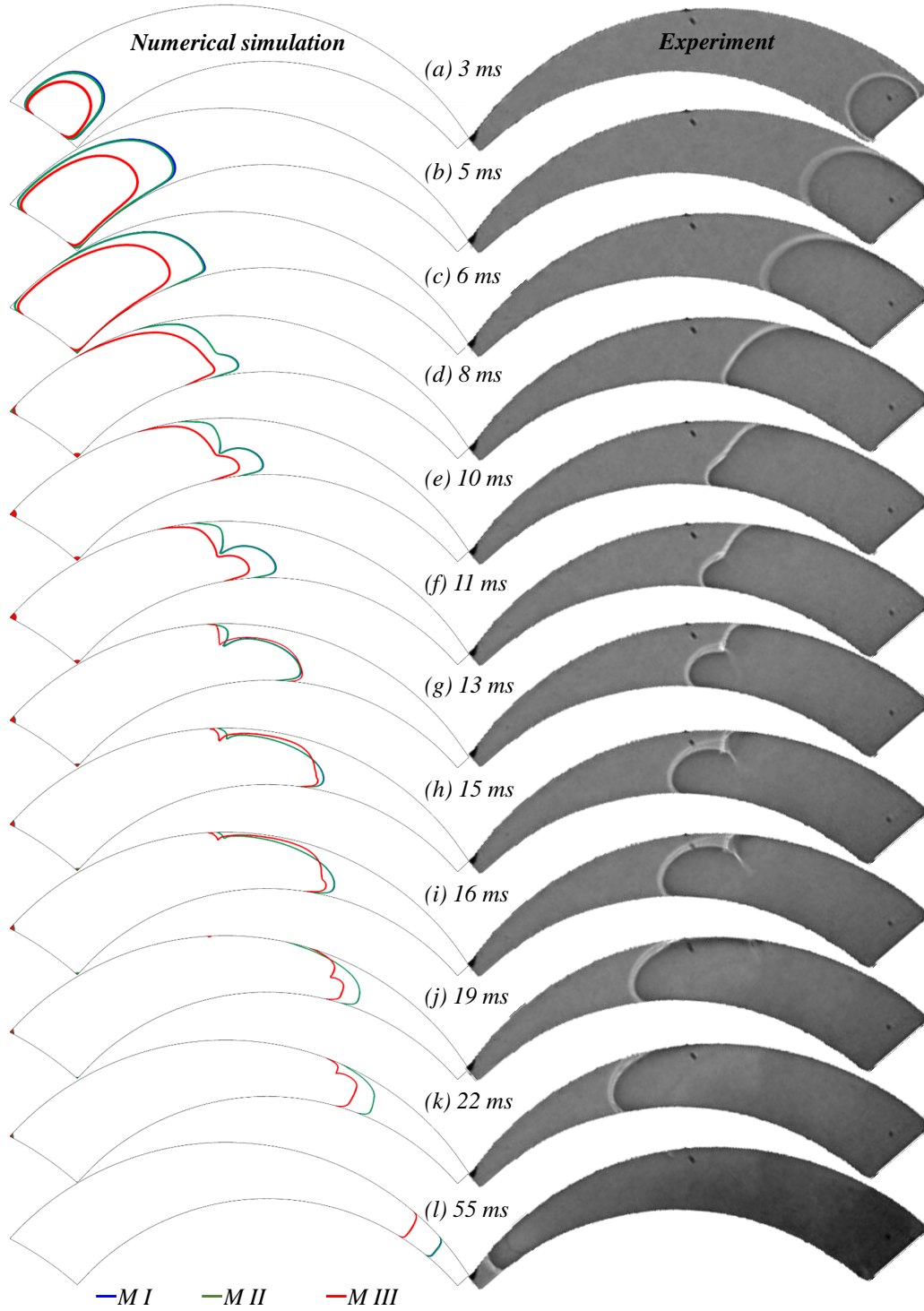


Figure 5.3: Methane/air premixed flame front development; (on the right) flame shadowgraphy and (on the left) flame fronts for $M(I)$, $M(II)$, and $M(III)$ models: (a-f) flame of $M(III)$ lags behind $M(I)$ and $M(II)$ and small discrepancy can be observed between $M(II)$ and $M(III)$ in b, (g-h) $M(III)$ flame is ahead of $M(I)$ and $M(II)$; (i-k) $M(III)$ develops a second tulip flame; (l) $M(I)$, $M(II)$, and $M(III)$ and converted into concave flames.

The second tulip flame, which is produced only by model $M(III)$, is of great importance for understanding the dynamics of confined premixed flames since neither the experiment nor models $M(I)$ and $M(II)$ produce reconstituted tulip flames. The global balance between heat and mass diffusion occasioned by putting $Le = 1$ is responsible for the second tulip flame. Thus, it appears that in certain flame stages a crucial role is played in tulip flame formation by Le , as discussed by Dunn-Rankin et al. (1988) and more recently by Ponizy et al. (2014).

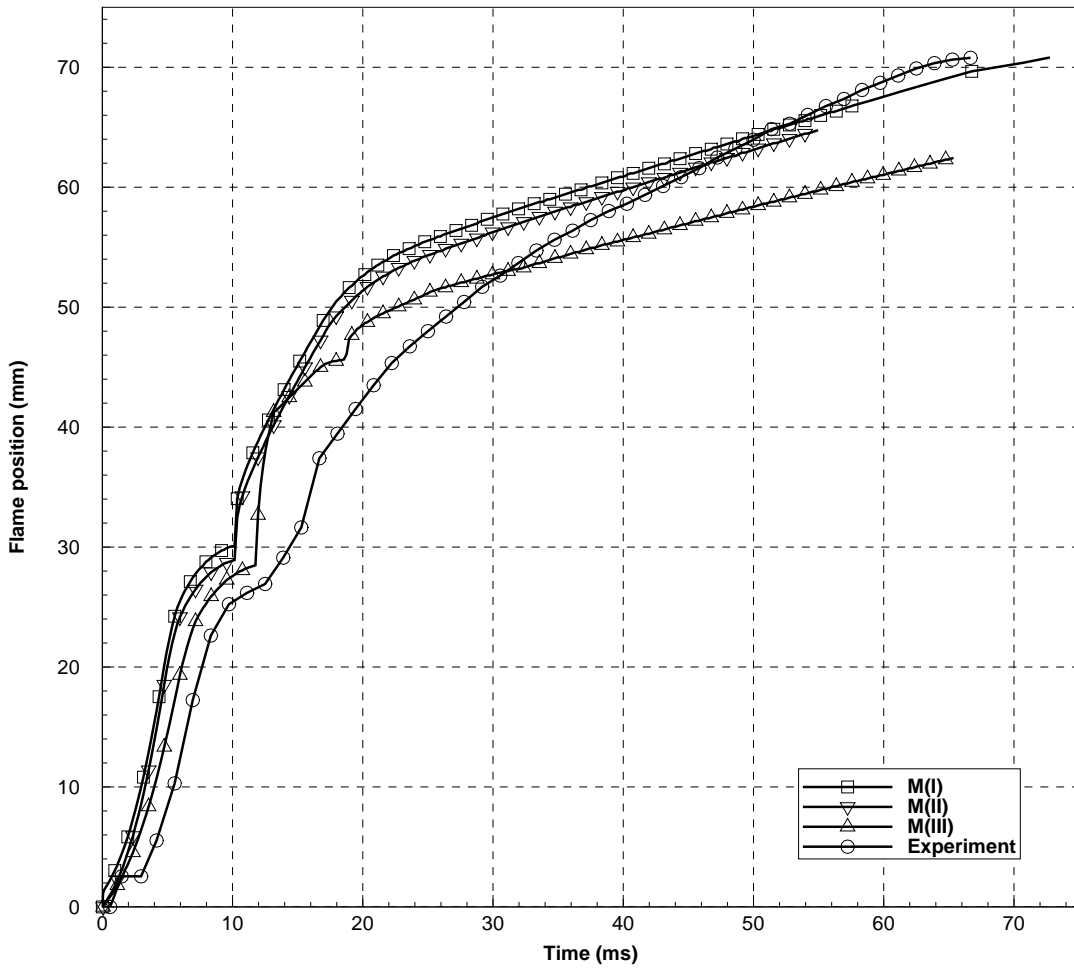


Figure 5.4: Flame tip distance from igniter location recorded at the channel centerline for models $M(I)$, $M(II)$, $M(III)$ and the experiment. The initial condition from which time is reached is the instant at which all flames have penetrated 5 mm into the channel.

5.1.2.2 Syngas flame

The flame fronts for lean premixed syngas flames of $\phi = 0.7$ and 50% H_2 are shown in Fig. 5.5 for three different diffusion models; Chapman-Enskog $M(I)$, mixture-averaged $M(II)$, and $Le = 0.575 = \frac{\lambda}{\rho c_p D_{kl}}$.

Unlike previously discussed of methane/air flame, the syngas flames exhibit more pronounced change in flame front structure under different diffusion models. The constant Lewis number case $M(III)$ under predicts the flame propagation speed throughout the combustion process. The mixture-averaged model $M(II)$ exhibits more pronounced deviation from the multicomponent model of Chapman-Enskog $M(I)$ than previously discussed for methane/air flames. The multicomponent model predicts flame front wrinkles at earlier time than mixture-averaged model, see Fig. 5.5-c. However, both $M(I)$ and $M(II)$ models predict similar average flame propagation speed. Fig. 5.5-c,f indicates that constant Lewis number is unable to produce the cellular structure of the flame front. However, Fig. 5.5-f shows very smooth wrinkles on the flame front.

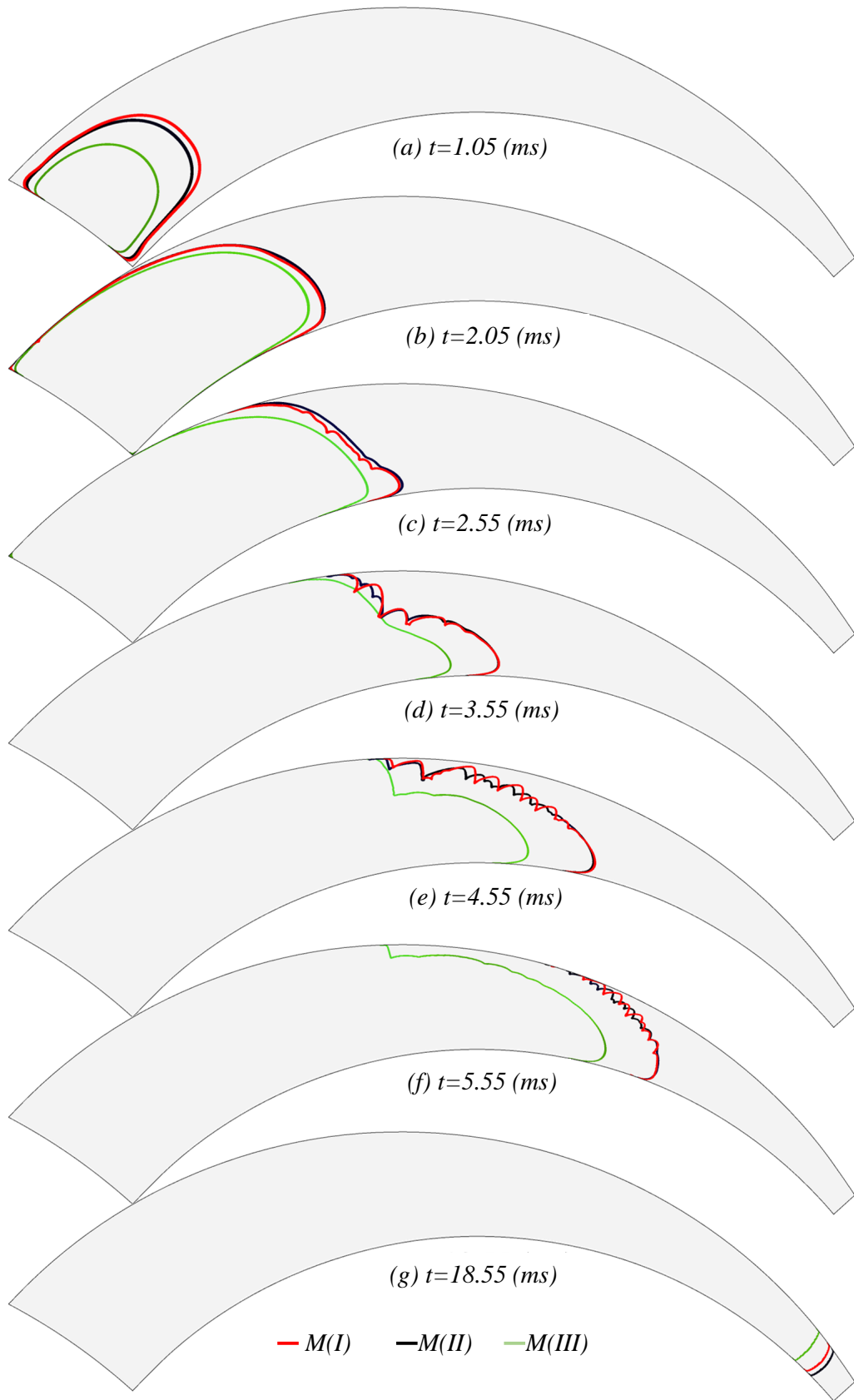


Figure 5.5: Premixed syngas flame front development for M(I), M(II), and M(III) diffusion models.

5.2 Pressure Dynamics and Flame Speed

Figure 5.6 shows the experimental flame speed and pressure evolution during methane/air flame propagating in the WDE channel. By excluding minor effects like dissociation and phase change of H_2O and considering the flame as a surface propagating at the observed flame speed, the rate at which the fuel is oxidized (or the rate of heat release) is proportional to the absolute flame speed and the flame surface area. In CV combustion, the pressure can be predicted by the net rate of heat addition, which can be simplified to specifying the average temperature change inside the vessel. The ideal gas equation, $p = mRT/V$, states that the chamber pressure is a function of temperature, T , when the quantity mR/V is constant. Thus in order to describe various important aspects of CV combustion, we examine the normalized rate of pressure change along with the behavior of instantaneous normalized flame speed, as shown in Fig. 5.6.

It is evident from Fig. 5.6 and from previous research (Hariharan & Wichman (2014), Ellis (1928), Ponizy et al. (2014), Xiao et al. (2013), Dunn-Rankin et al. (1988), etc.) that the flame speed and the pressure change history are related to one another. It is our contention that the phases of flame dynamic evolution are recognizable in the temporal structure of the absolute flame speed and the pressure field during burning.

Consider first the flame speed. Here we define an average flame speed by calculating the mean value of five (5) points on the flame front. We do this because tracking many points on the flame front yields a consistent average flame speed. Two points are taken at the intersection of the flame with the upper and lower sidewalls, while the other three points are equally spaced throughout the particular section of the channel height.

Consider now the pressure field. Here we shall use the experimentally measured pressure $p(t)$, which, as indicated in Fig. 5.6 is the average over eight (8) tests, as well as its first deriva-

tive $(dp(t)/dt)$ and its second derivative $(d^2p(t)/dt^2)$ as “signatures” for the various combustion phases, in conjunction with the flame speed measurements discussed above. The derivative yields local extrema of $p(t)$ whereas the second derivative yields inflection points of $p(t)$ as well as locations where the change of $p(t)$ is most rapidly increasing or decreasing. For the sake of clarity or presentation, the pressure, pressure derivative and second derivative are normalized such that their maximum values are unity (Fig. 5.6).

Physically, positive values of $dp(t)/dt$ indicate that as the pressure increases, the flame, which does not necessarily accelerate, is burning vigorously enough to provide sufficient thermal energy for pressure rise. Equation (4), for example, can be rewritten as $D(\rho E)/Dt = dp/dt$ when the following three qualifiers are acknowledged: (1) we consider regions outside the flame (where the chemical reaction term is exactly zero); (2) we neglect viscous dissipation; and (3) we disregard gradient transport of thermal energy. In the limit of a flame sheet model (infinitesimal flame thickness) the volume occupied by the flame front in the CV channel is negligible. The preceding equation directly relates thermal energy accumulation (loss) to the rate of pressure rise (fall). Thus, negative values of $dp(t)/dt$ suggest a weakening, decaying flame. The normalized first and second derivatives, $dp(t)/dt$ and $d^2p(t)/dt^2$, provide specific quantitative information on the structure of the pressure time-history and therefore, by extension, a rational, quantifiable sectioning of the five combustion phases.

Phase I, the ignition phase, is characterized by positive values of $dp(t)/dt$ and $d^2p(t)/dt^2$: here the flame is growing radially unobstructed and unaware of the surrounding CV confinement. Phase I may be taken to end when $dp(t)/dt$ is highest. This occurs when $d(dp(t)/dt)/dt$ is a maximum.

Consider now phase II, where the spherically expanding flame undergoes transition into the concave “finger” flame extensively discussed by Clanet and Searby Clanet & Searby (1996) in their open-ended circular tube experiments. The pressure in the CV chamber continues to monotonically

raise after phase I with large and increasing $dp(t)/dt$. However, at approximately a normalized time of 0.07 the value of $dp(t)/dt$ attains a maximum value after which it decreases. The maximum value of $dp(t)/dt$ is where one finds $d^2p(t)/dt^2 = 0$. This behavior of the pressure trace can also be seen in the $p(t)$ curve although not as distinctly as for the $dp(t)/dt$ curve. We believe that at this instant the flame skirts first touch the walls and then begin their rapid approach toward the flame front from behind the flame (see Fig. 5.1d- Fig. 5.1g): for this reason, the averaged flame front speed increases although the middle section of the flame front is slowing down. In general, locating the maximum of $dp(t)/dt$ seems to be a more reliable indicator of flame skirt touchdown than is visual ascertainment of the same. In phase II, the cross-section averaged flame speed still increases monotonically while also lagging with respect to the pressure trace. The averaging process using five points along the flame sheet produces a flame speed that is generally larger than would be found by sampling the flame speed at the center of the channel, because of the rapid acceleration of the sides of the flame as they quench along the cold walls. This phase is the only one in which the averaging process described above could possibly yield deceptive average flame speeds. Phase III, which is taken to begin at the maximum of $dp(t)/dt$ at normalized time 0.07, can be approximately characterized by the strong decrease throughout of $dp(t)/dt$. The value of p continues to increase though at a consistently diminished rate, hence the second derivative is always negative with a minimum value approximately in the middle of this phase. The latter part of phase III is characterized by the deceleration of the flame front caused by the quenching of the flame edges by the cold channel walls culminating, at the end of this phase, in a local minimum of the flame speed. However, the flame is sufficiently strong to maintain a pressure rise as reflected in the positive value throughout of $dp(t)/dt$. At the end of phase III, the flame is essentially flat. From Fig. 5.1h this occurs approximately when $\bar{t} = 9.1ms/65ms = 0.14$. A more careful evaluation of the flame images indicates that the flatness occurs almost exactly when the normalized time is

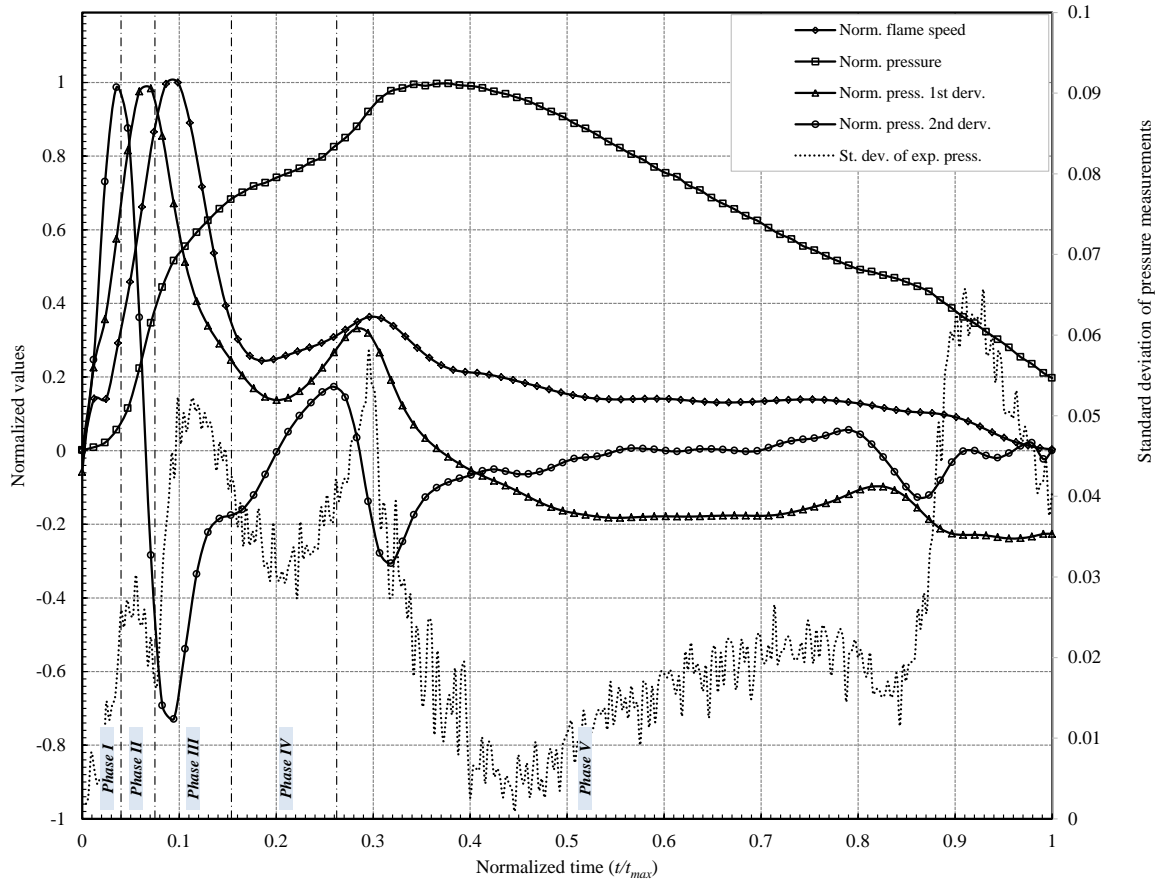


Figure 5.6: Experimental measurements of normalized flame speed, normalized pressure $P[\text{bar}]/3.15$, normalized rate of pressure change $(dP/dt)[\text{bar/s}]/866$, and normalized pressure second derivative. The numbers in these denominators are maximum values that are used to scale all of the curves for improved visualization. The data shown are averages of eight separate experiments. Also shown on the right-hand scale is the experimentally measured variance of the pressure data, indicating it to be under 1%. The experiments measure flame position: flame speed is obtained by differentiation.

0.15, as indicated in Fig. 5.6. This particular instant of burning was not included in Figs. 3a-o.

Phase IV begins with the formation of the flat flame front (Fig. 5.1h) which occurs in Fig. 5.6 at $\bar{t} = 0.14$. At this time the flame speed acquires a local minimum value as very nearly does the local value of $dp(t)/dt$. Phase IV ends when the tulip flame vanishes at $\bar{t} = 16.7ms/65ms = 0.26$ in normalized units (Fig. 5.1n). This endpoint coincides with a local maximum rate of increase of $dp(t)/dt$, where $d^2p(t)/dt^2$ is maximum. The newly reconstituted concave flame front has a large (relative) surface area, much as in phase II, and thus energy addition via $D(\rho E)/Dt = dp/dt$ once again increases rapidly before the flame begins its decay toward extinction in the quenching phase V, described below.

In phase V, the heat losses to the cold walls become more pronounced as the flame struggles to pass through the narrow space between the channel walls as it moves toward the channel end in search of as-yet-unburned reactant. These heat losses, which can be calculated from the numerical simulation and which begin at the start of stage V, are not shown in the present work. The flame front displays a continuous reduction in flame surface area. In phase V the rate of pressure change $dp(t)/dt$ becomes negative, which indicates that the thermal energy ρE in the channel is decreasing due to the weakness of the flame induced by heat losses. A discussion and an explicit calculation of this behavior is found in Kiran et al. Kiran et al. (2014). In phase V, The pressure curve reaches its maximum at about 0.37 of the combustion time (which occurs between Fig. 5.1n and Fig. 5.1o), after which $dp(t)/dt$ drops below zero. The pressure then starts to decrease and the flame in this phase decelerates. A marked reduction in flame speed and rate of pressure change is observed around 90% of combustion time, $\bar{t} = 0.9$ which indicates the time of flame quenching at the channel end wall.

5.3 Flame-Induced Flow

Once the combustion reaction starts and become self sufficient, the heat release term increased significantly in the reaction zone, which in turn hike the temperature and consequently the pressure. This environment induces flow called flame-induced flow which interacts afterward with flame front and contributes to flame dynamics evolution Jeung & Cho (1989).

5.3.1 Flame-induced flow and vorticity

The flow induced by the flame can create an environment near the flame front that subsequently alters flame evolution Kiran et al. (2014), Zhou et al. (2006), Xiao et al. (2012a). Here, we confine our discussion to the results of the simulation. In Fig. 5.7, the flame tracked by mass fraction contours of HCO and velocity vectors are plotted over a vorticity scale colored surface to characterize the interaction between flame front and flame-induced flow. As indicated previously in Sec. 3.1, the flame zone HCO distribution appeared to be adequately resolved in the simulations.

During the hemispherical expansion of the flame kernel, the burned gas flow produced from the lateral flame moves from the sidewalls toward the centerline of the channel and is then deflected axially downstream along the channel centerline toward the flame front, in the same direction of unburned gas moving ahead of the flame (Fig. 5.7a, Fig. 5.8). It is certain that this flow pattern contributes to the acceleration of the flame front during phases I-II. It is also evident that the flow pushed by lateral sections of the flame front is affected by chamber geometry, which narrows along its length (Fig. 4.2). This forward “push” of the unburned gases until about 7 ms (see Fig. 5.7a, Fig. 5.7b, and Fig. 5.7c) produces a large velocity gradient near the upstream channel walls, which generates a local vorticity maximum at the walls along with a narrow high-vorticity layer near the walls. This wall-generated vorticity is about a factor of five (5) larger than the local flame-

generated vorticity as is denoted by the color scaling in these figures. At approximately 5 *ms*, the lateral flame starts to touch the inner sidewall, which stops the forward propulsion of the flow from the bottom toward the centerline of the channel. The upper lateral flame, which has not yet touched the wall, continues to thrust the burned gases toward the inner wall, which are then deflected toward the flame front. These gases move downstream near the inner sidewall instead of the middle of the channel. The net effect is to accelerate the flame front near the inner sidewall as shown in Fig. 5.7b, and Fig. 5.8 making the flame “bulge” somewhat in this vicinity. During this time the upper lateral flame starts touching the top sidewall, producing fewer burned gases. No more burned gases can be observed moving from the lower segment of the lateral flame from approximately 5.5 *ms* onward (Fig. 5.7b). By this time, the majority of burned gases are produced by the flame front and hence deflected toward the ignition point while the unburned gases ahead of the flame front continue their movement downstream, see Fig. 5.7c. This inversion in burned gas flow can be clearly observed after $t \cong 6 \text{ ms} / 65 \text{ ms} = 0.092$ at the time when flame propagation experiences a significant deceleration during phase IV, see Fig. 5.6. The inversion in burned gas flow occurred 2-4 *ms* before the tulip flame cusp was first observed at around 10.5 *ms*. This indicates a distinct role played by inversion on premixed flame evolution Ponizy et al. (2014). The results also show that after the inversion of the burned gas flow, an increase in vorticity is observed behind the flame front. By contrast, a reduction is observed in the vorticity near the sidewalls in the unburned upstream region. Thus, the bulk velocity of unburned gas ahead of flame front slows down after flow inversion, see Fig. 5.7c, Fig. 5.7d, Fig. 5.7e, and Fig. 5.7f. This slowdown is caused in part by compression and by reverse flow of the vertical motion induced in this region by the forward thrust toward the sides of the channel. After that the tulip flame propagates downstream where the flame cusp moving toward the upper sidewall and the tulip flame is reverting to its pre-tulip concave shape (Fig. 5.7e). The burnt gases at this time move upstream while the fresh mixture

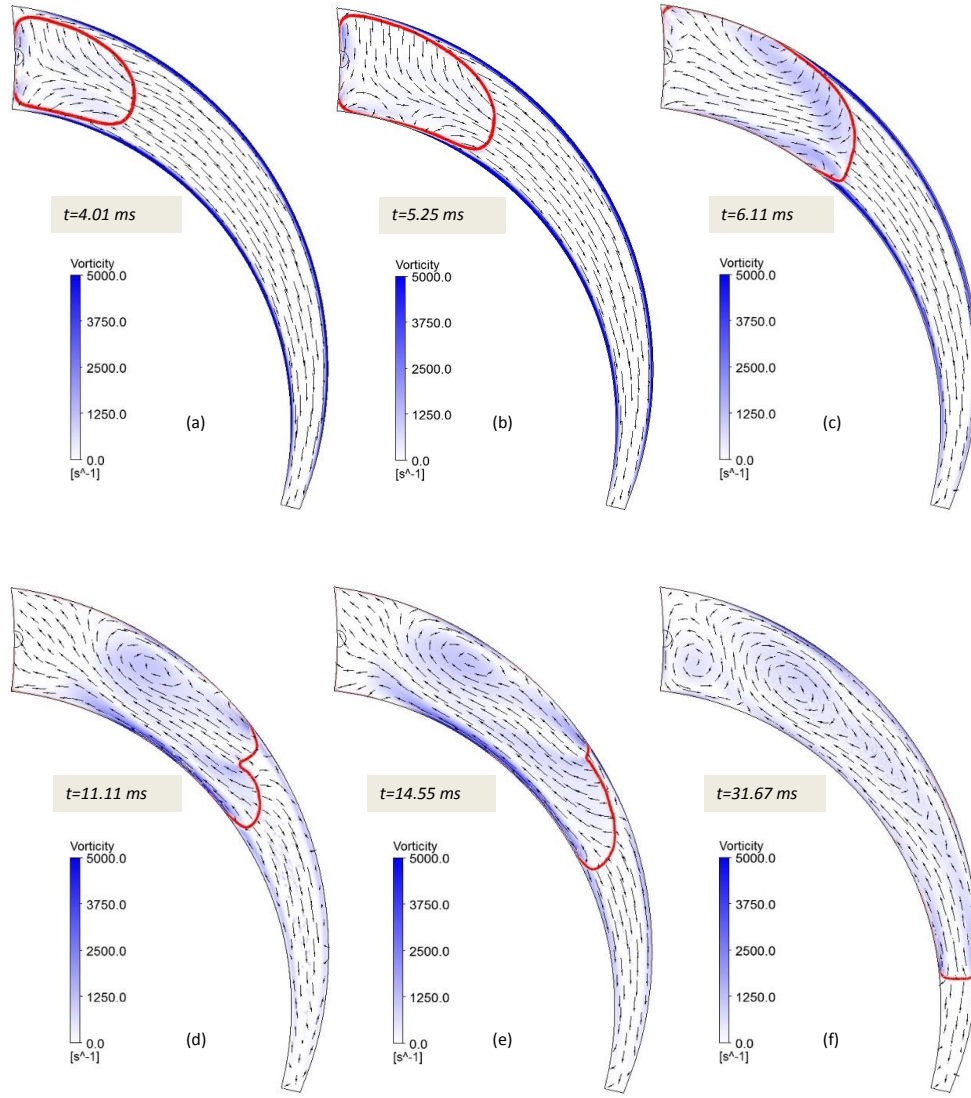


Figure 5.7: Interaction between flame front and flame-induced flow: (a) burned gas produced by lateral flame moves from sidewalls toward the centerline of the channel, and then is deflected along the channel centerline; (b) inner lateral flame is quenched while upper lateral flame continues to thrust the burned gases toward the inner wall and is then deflected toward the flame front; (c) inversion of burned gas flow; (a-c) vorticity is generated in the near wall region of the channel by the forward forced flow; (d-f) vorticity is generated in burned gas behind the flame front by the rearward forced flow. The change in flame morphology from concave to convex occurs between (c) and (d) as the tulip is formed while the change from convex to concave occurs between (e) and (f) as the concave flame front is reconstituted.

continues to move downstream until the flame quenches at the channel end wall, see Fig. 5.7f.

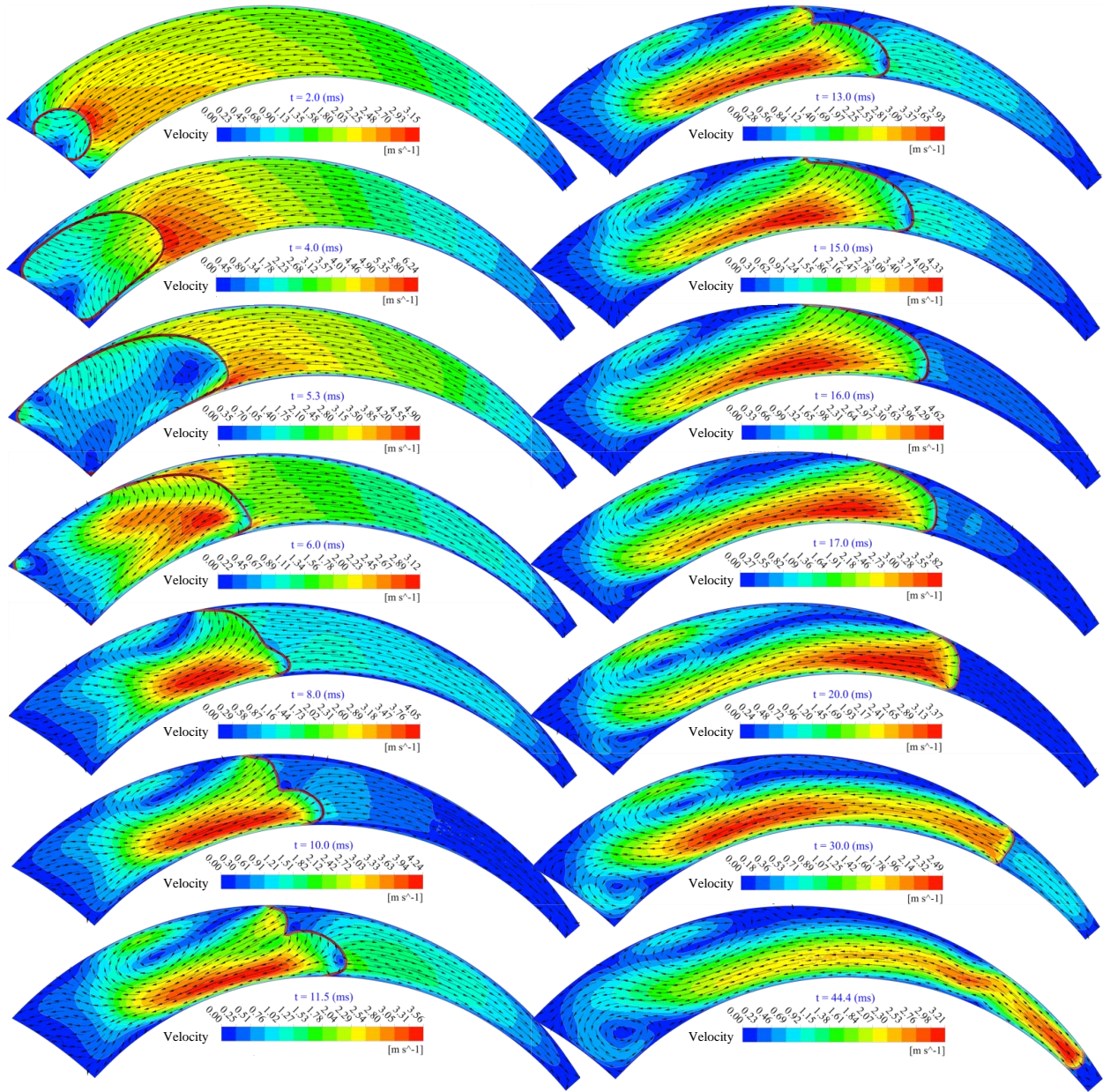


Figure 5.8: Velocity field induced by the flame at different combustion time.

5.3.2 Flame flow interaction

The small scale (high frequency) intrinsic instabilities of confined premixed flame propagating into quiescent mixture are basically caused by two main phenomena; the hydrodynamical phenomena

associated with thermal expansion of burned gases or flame-induced flows, and thermodiffusive phenomena controlled by Lewis number Kadowaki et al. (2005), Clavin (1985). Fig. 5.9 shows the flow interaction with flame front of $M(III)$. In the spherical and finger flame stage of Fig. 5.9a, the hydrodynamical phenomena associated with thermal expansion of burned gases is dominant. The flow near the flame front can be characterized by alignment angle between burned and unburned gases and the saddle point fitted near the ignition zone in the place where the burned gases produced by lateral flame are deflected toward flame front (Fig. 5.9a,b). Both burned and unburned flows are aligned to each other near the channel centerline and moving away from ignition which accelerates the flame front at this area while the flame slows down away from channel center toward the sidewalls as the alignment angle increase and approach maximum near the sidewalls. It is certain that the local absolute flame propagation speed is highly affected by the alignment angle between burned and unburned flows with inverse proportions, see Fig. 5.9a,b. Once the lateral flames annihilated by the cold sidewalls, the burned gases turned back into ignition zone and saddle point moves close to and behind the flame front on the downstream side at the place where the cusp of the tulip flame will be established later (Fig. 5.9c). Once the cusp and lower tongue of the tulip flame start evolving, the saddle point again moves next to and behind the lower tongue flame front and stay there till the upper tongue is fully diminished by growing lower tongue and the second tulip flame starts evolving (Fig. 5.9d-f). It can be observed that the lower tongue of the second tulip flame is free of the saddle point unlike its predecessor, which gives evidence that the presence of saddle point close to the flame front indicate that the flame front has the tendency to fold. It can be concluded from these results and work of Hariharan et al. Hariharan & Wichman (2014) that the movement of the saddle point presents a certain evidence that the flame-generated flow significantly contributes to the dynamics of the flame front and tulip flame formation.

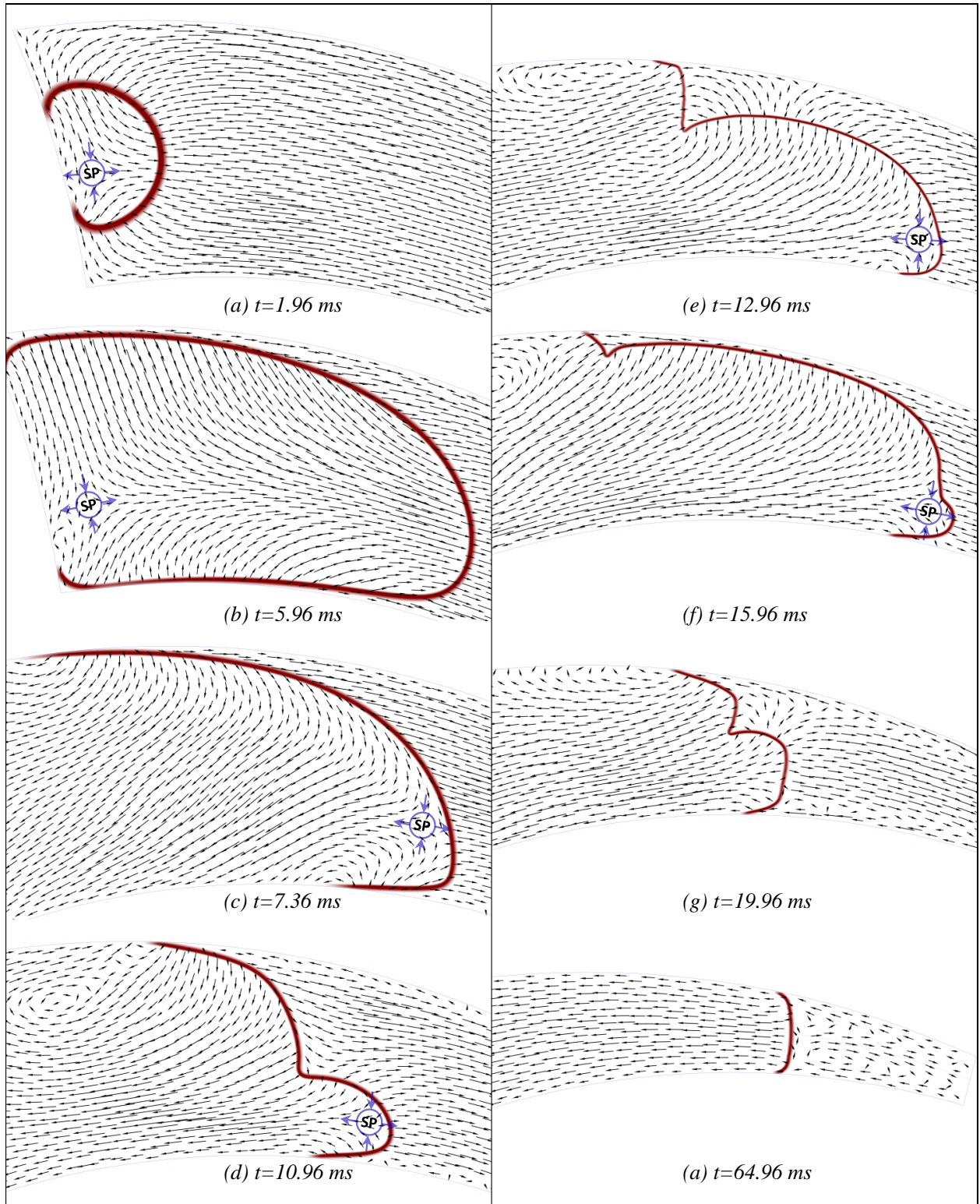


Figure 5.9: Flame-induced flow and the characteristic saddle points of unity Lewis number flame: (a) spherical flame surrounds saddle point; (b) finger flame front away from saddle point ; (c) saddle point moves close to skirt flame; (d-f) saddle point moves close to lower tongue of the first and second tulip flame; (g-h) no saddle point was observed.

In Fig. 5.7 and Fig. 5.8 the saddle point and various nodes and half saddles are not directly visible in the WDE channel as they were in the straight channel, see Fig. 6.4. The saddle point is identified in velocity vector plots as regions of very slow flow surrounded by fluid flowing in opposite directions along perpendicular axes. Such a flow pattern is evident in Fig. 5.7 and Fig. 5.8. Thus, Fig. 5.7a shows that nascent saddle formed right after ignition, and Fig. 5.7b shows that the saddle has moved close to and behind the flame front on the downstream side. In Fig. 5.7c the saddle is located along the flame front on its straighter edge toward the inside sidewall. Fig. 5.7d shows that the saddle point is located in front of the flame on its upstream side, whence the tulip shape of the flame front as discussed out in Section 6.1.2. It is not clear from Fig. 5.7e and Fig. 5.7f, where the saddle point is located after the concave flame front reconstitutes itself, although a careful examination of Fig. 5.7e suggests that it resides at or very near the flame front. The characteristic flow feature of saddle point motion appears to remain intact even when the CV chamber is a complex, curved shape.

The relevance of the motion of the saddle point consists of its direct relation to the fundamental structure of the flow field behind, at and in front of the flame during its evolution. Much effort has been expended in theoretical and physical discussions focusing on the basic nature of the transition from concave to convex tulip flame, for example whether it is governed by Rayleigh-Taylor, Richtmeyer-Meshkov or Darrius-Landau instability mechanisms. In fact, it is governed by none of these (Hariharan & Wichman (2014), Ponizy et al. (2014)), instead manifesting as the consequence of intense flame-flow interaction of a minimally two-dimensional kind: the formation of the tulip in straight channels and in the moderately curved channel studied here is the outgrowth of a complex flame-flow interaction whose most distinct and recognizable feature is the propagating saddle point.

5.4 Impact of Soret effect

In transport phenomena, Soret diffusion is the mechanism by which light (heavy) molecules are transported in multicomponent mixture toward (away from) the hot region driven by temperature gradient. To explore the Soret effect on mixture stoichiometry, the distribution of trapped reactants species between the flame front and the channel end wall was plotted versus normalized channel's width at arbitrary time of 55 *ms* where the temperature of fresh gases at the channel's center approaches 400 *K* due to the confinement effect, see Figs. 5.10, 5.11, 5.12, 5.13. The results reveals that the concentration of relatively light species such as CH_4 near the cold sidewalls of the channel is lower than the hot zone in the middle of the channel by 4.1% (Fig. 5.10), whereas the relatively heavy species like AR and O_2 has opposite concentration distribution by 2.28% and 0.88%, respectively, see Figs. 5.11, 5.12. Since the temperature gradient between the burned gases and cold sidewalls is much higher than unburned gases region, the Soret effect on species concentration become even more pronounced. The nitrogen N_2 , for example, has 1.312% higher concentration near the cold sidewalls in the burned gases side compared to 0.0075% in unburned gases side, (Fig. 5.13). The unburned mixture species show uniform and constant distribution when the Soret effect is not considered such $M(II)$ and $M(III)$ (Fig. 5.11)

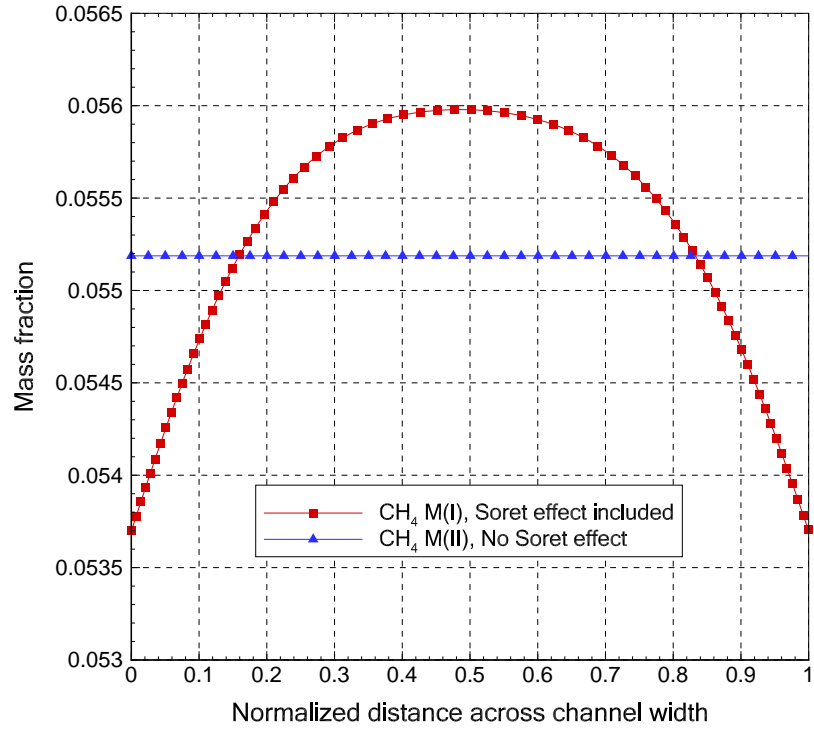


Figure 5.10: Soret effect impact on the CH_4 species concentration plotted along the normalized channel width in the unburned region.

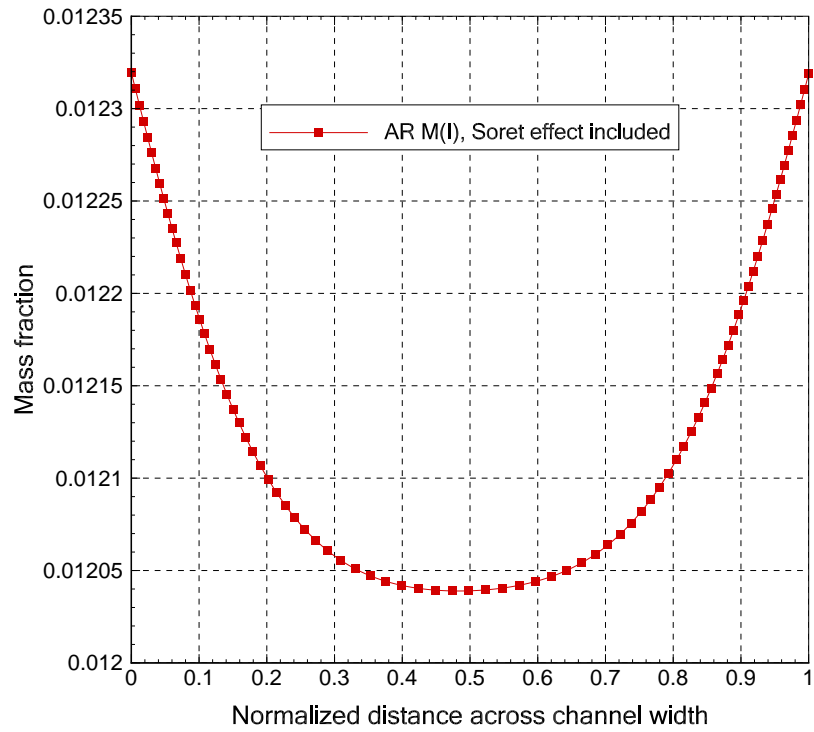


Figure 5.11: Soret effect impact on the AR species concentration plotted along the normalized channel width in the unburned region.

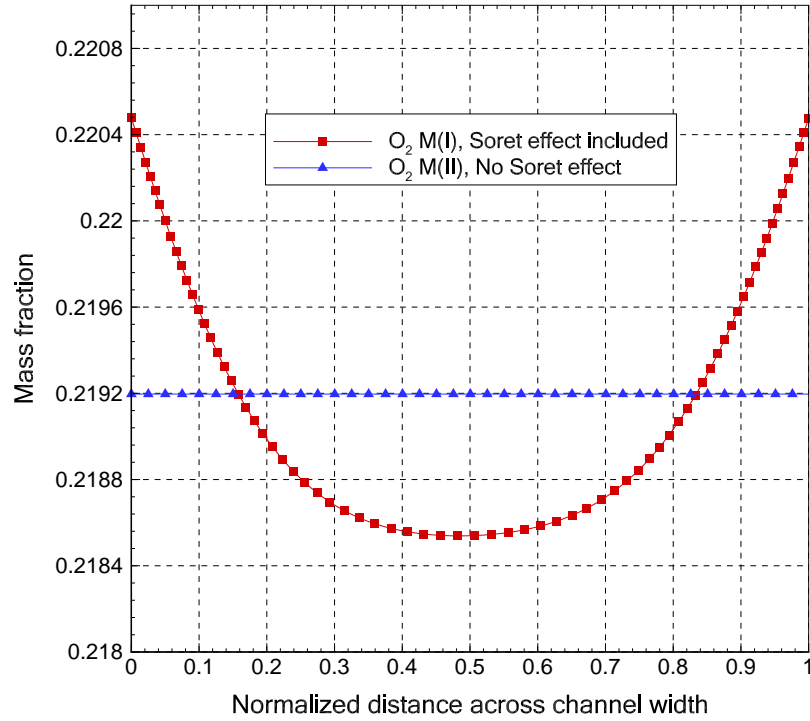


Figure 5.12: Soret effect impact on the O_2 species concentration plotted along the normalized channel width in the unburned region.

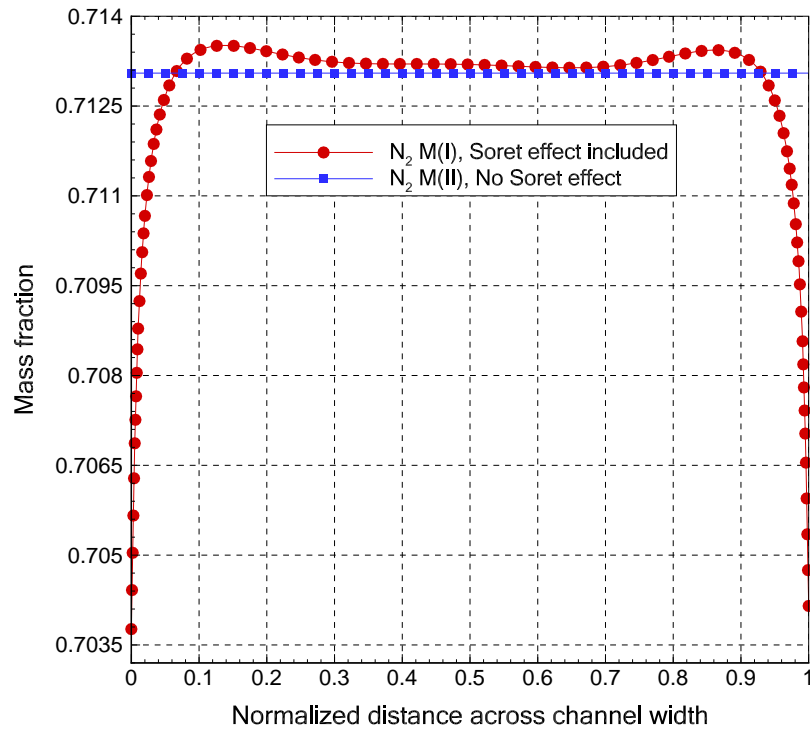


Figure 5.13: Soret effect impact on the N_2 species concentration plotted along the normalized channel width in the unburned region.

In the burned region where characterized by higher temperature, more species get involved, dissociation phenomena, and phase change, the transport of products species e.g. CO_2 , H_2O , N_2 , etc., reveals complicated transport behavior for species like H_2O , see Fig. 5.14. The distribution of products species in the burned region correlates with the temperature gradient distribution which is driven by the burned gases velocity field. The CO_2 species concentration (Fig. 5.15) exhibit similar behavior as O_2 (Fig. 5.12) with higher gradient near the wall due to higher temperature gradient and larger molecular weight while once again the H_2 species diffuses in the opposite direct.

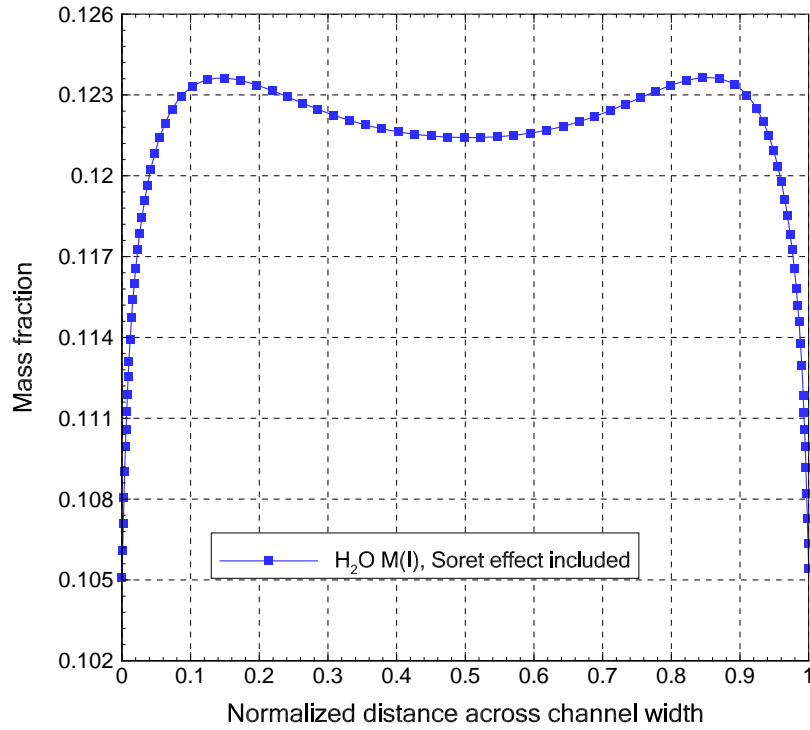


Figure 5.14: Soret effect impact on the H_2O species concentration plotted along the normalized channel width in the burned region.

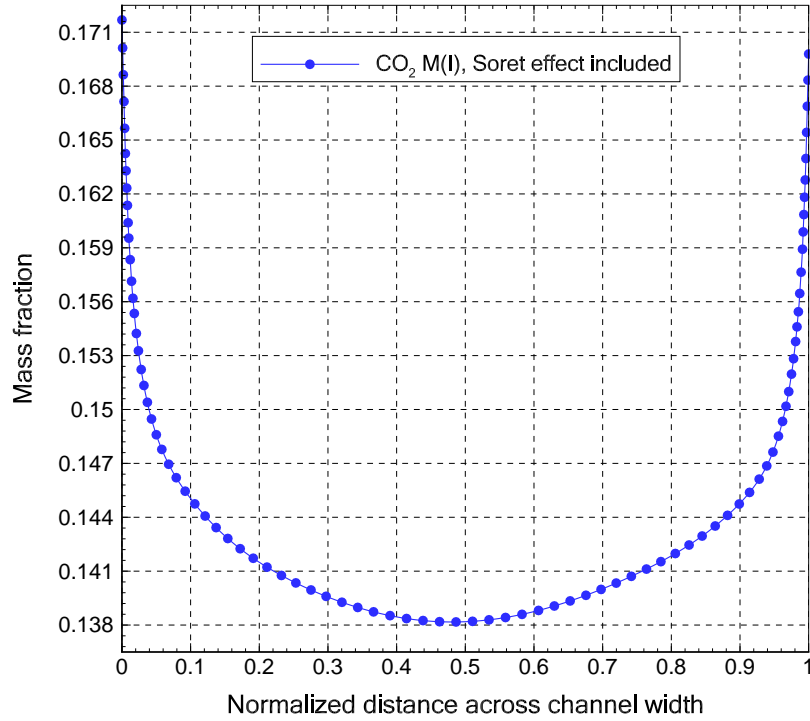


Figure 5.15: Soret effect impact on the CO_2 species concentration plotted along the normalized channel width in the burned region.

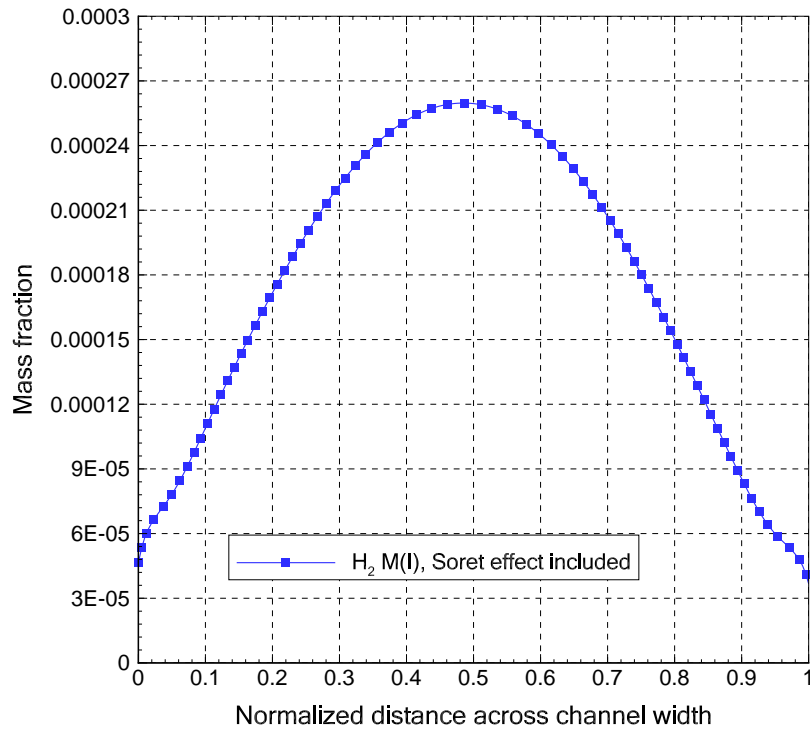


Figure 5.16: Soret effect impact on the H_2 species concentration plotted along the normalized channel width in the burned region.

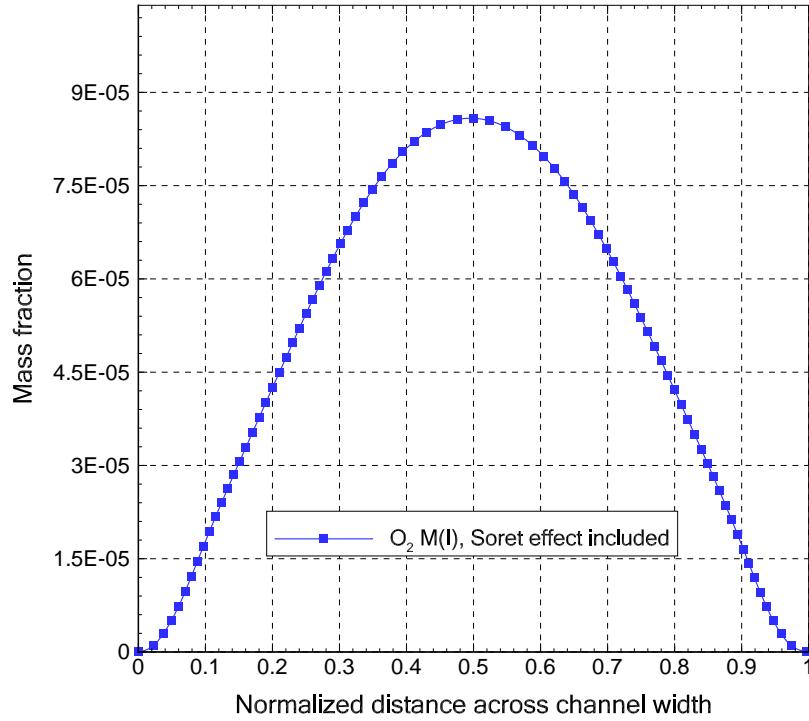


Figure 5.17: Soret effect impact on the O species concentration plotted along the normalized channel width in the burned region.

In syngas/air mixture, the light species of H_2 shows strong and opposite transport compared with CO due to the Soret effect which modifies mixture stoichiometry. The H_2 concentration can be $\sim 10\%$ more near the channel cold walls while the maximum difference in CO concentration is approximately 1.35% (Fig. 5.18). The O_2 and N_2 species migrate in the opposite direction to H_2 species as shown in Fig. 5.19.

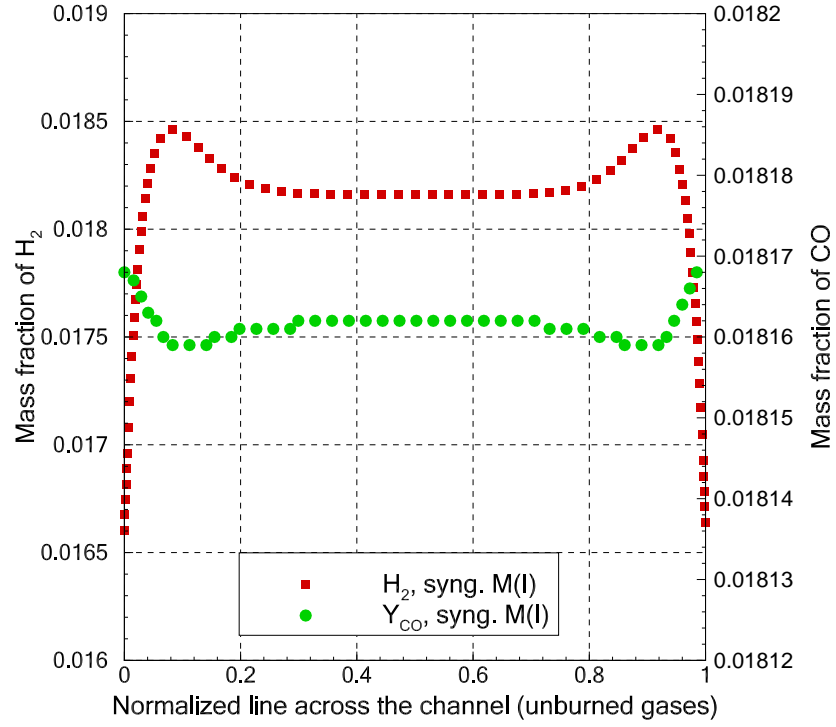


Figure 5.18: Mass fraction of H_2 and CO distributed across the WDE channel for the case $M(I)$.

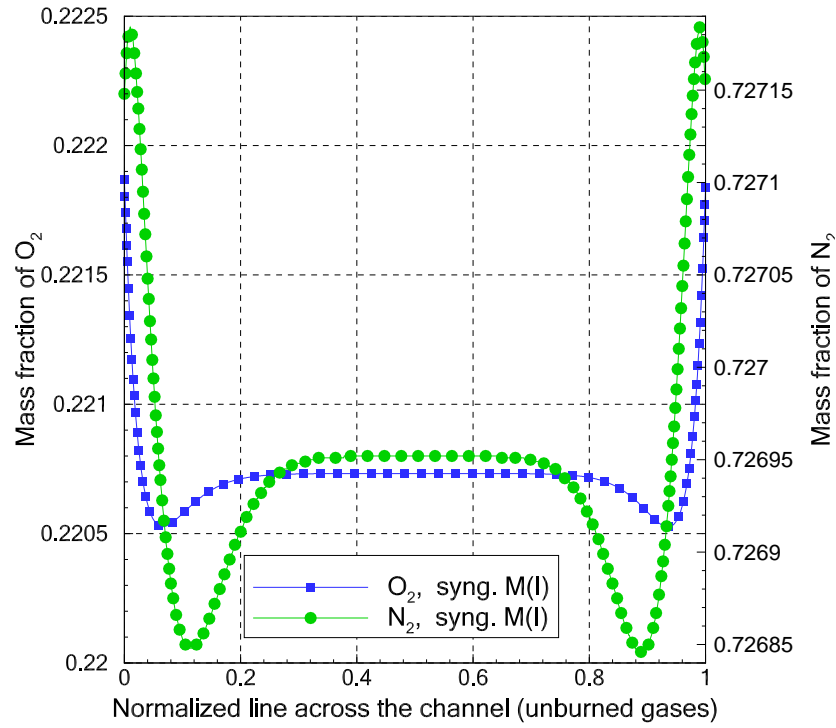


Figure 5.19: Mass fraction of O_2 and N_2 distributed across the WDE channel for the case $M(I)$.

The mass flux ($kg/(m^2s)$) of CH_4 , O_2 , N_2 , and CO_2 due to the Soret effect at 14.96 ms shows that the relatively light species such as CH_4 and N_2 have a negative mass flux near the cold sidewalls, which means that they migrate against the temperature gradient from low to high temperature region, see Fig. 5.25a,d. An opposite behavior can be observed for relatively heavy species like CO_2 and O_2 , see Fig. 5.20b,c.

The results show the quantitative contribution of Soret effect in changing the mixture stoichiometry ahead of the flame and near the chamber cold sidewalls. The mixture near the cold sidewalls is obviously lean mixture of equivalence ratio 1.03 since the CH_4 migrates away from the cold wall whereas the O_2 migrates toward the cold walls due to Soret effect. These changes in species concentration, however left no significant effect on flame absolute speed and structure (Fig. 5.3), peak temperature (Fig. 5.22), and average pressure (Fig. 5.22), nevertheless the transport behavior of multicomponent mixture is of critical importance in safety and pollution areas. The same conclusion was drawn from previous work of Yang et al. Yang et al. (2011) where Soret effect on freely propagating n-butane/air mixture was considered.

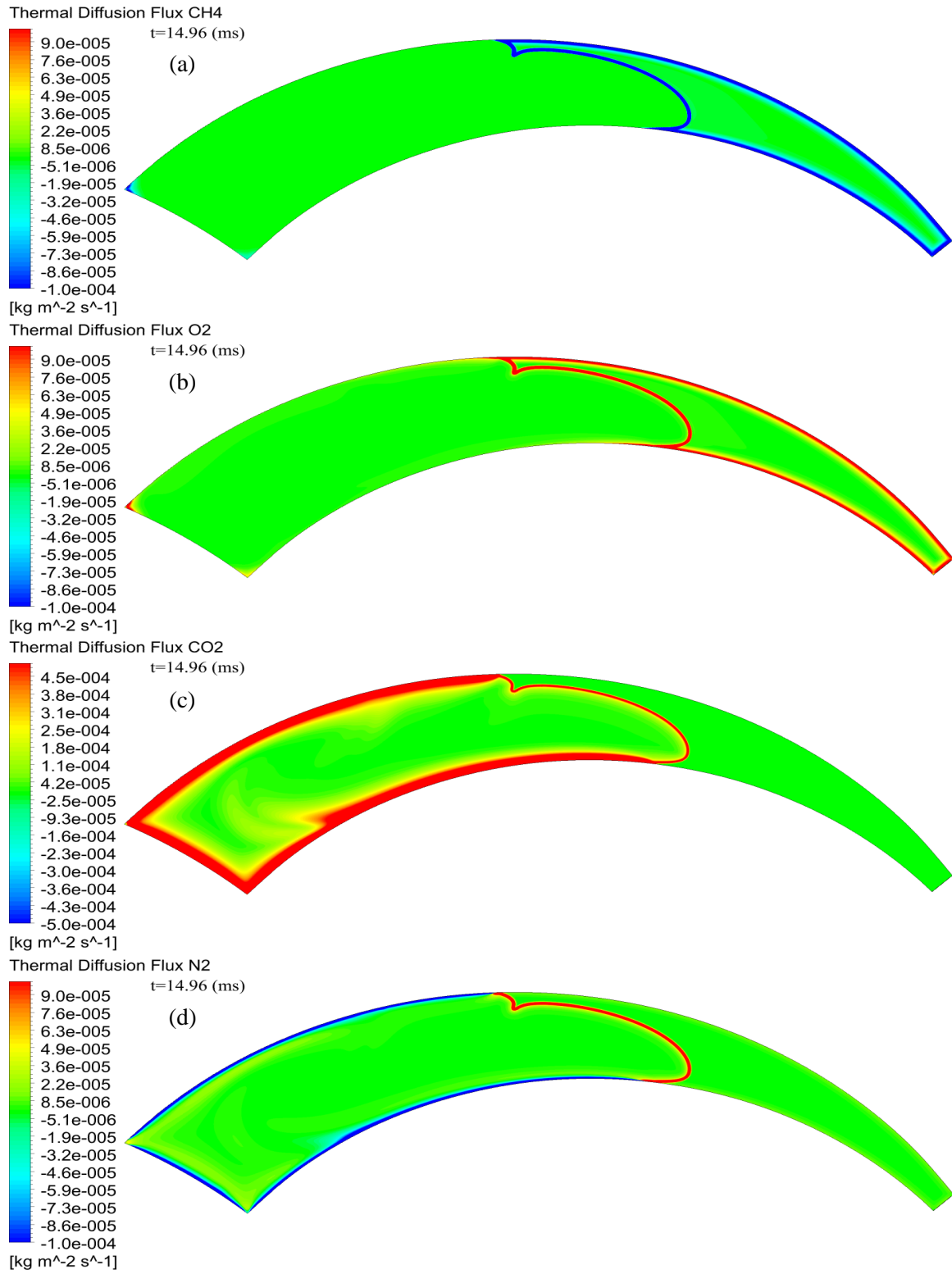


Figure 5.20: Mass diffusion flux due to Soret effect at, 14.96 ms for: (a) CH_4 ; (b) O_2 ; (c) CO_2 ; (d) N_2 .

5.5 Influence of Effective Lewis Number

As it is used to compare the molecular diffusion speeds of species versus heat, the Lewis number for laminar premixed flame is of critical importance since it has a direct effect on the intrinsic thermodiffusive instabilities, stretching, extinction, and other flame features Poinso & Veynante (2005).

The comparison between time history of peak temperature and average pressure using unity Lewis number model $M(III)$ and more detailed diffusion models $M(I)$, and $M(II)$ is presented in Figs. 5.22, 5.21. The peak temperature and average pressure of unity Lewis number are following but lagging behind its counterparts of $M(I)$ and $M(II)$ up to the combustion time of 11.8 ms, after which time the peak temperature (Figs. 5.22) as well as the average pressure (Figs. 5.21) of unity Lewis number increase drastically and jump above the values of $M(I)$ and $M(II)$ during the time 11.8 to 17.6, during which time the expansion of lower flame tongue speed of $M(III)$ is accelerated dramatically faster than other flames of $M(I)$ and $M(II)$ as we have discussed in Section 5.1.2. Furthermore, the unity Lewis number model develops a new secondary tulip flame at about 16 ms after the first primary tulip flame was completely annihilated which has never been reported in any previous study. These deviations in peak temperature, average pressure, and flame dynamics for unity Lewis number model are however unrealistic since neither the models $M(I)$ and $M(II)$ nor the experiments in the previous work Najim et al. (2015) produce such behavior. This reveals that the Lewis number cannot be assumed as unity or even constant in a situation where we have stretched tulip flame since we are dealing with multicomponent mixture in which the temperature, the pressure, and the mixture composition are changing with space and time.

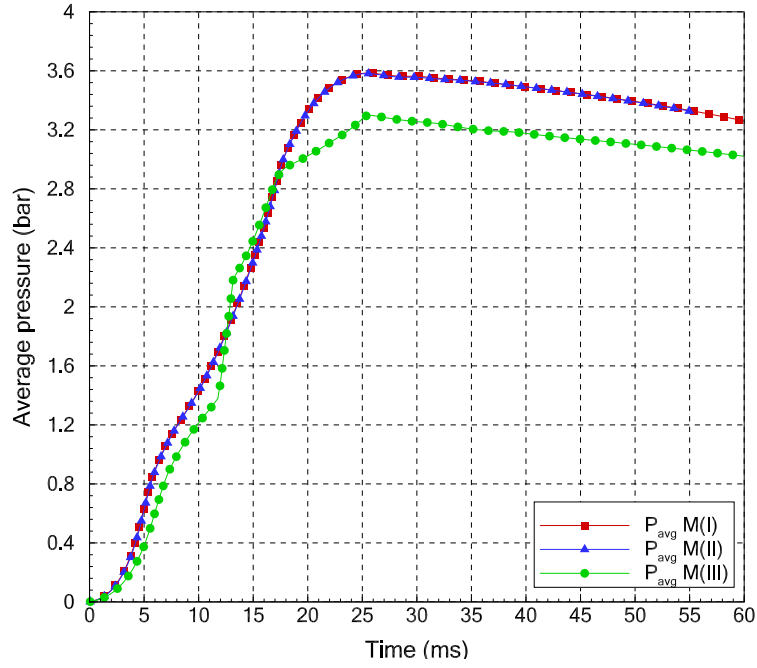


Figure 5.21: Average pressure developed in the WDE channel under three different diffusion model $M(I)$, $M(II)$, and $M(III)$ for stoichiometric methane/air.

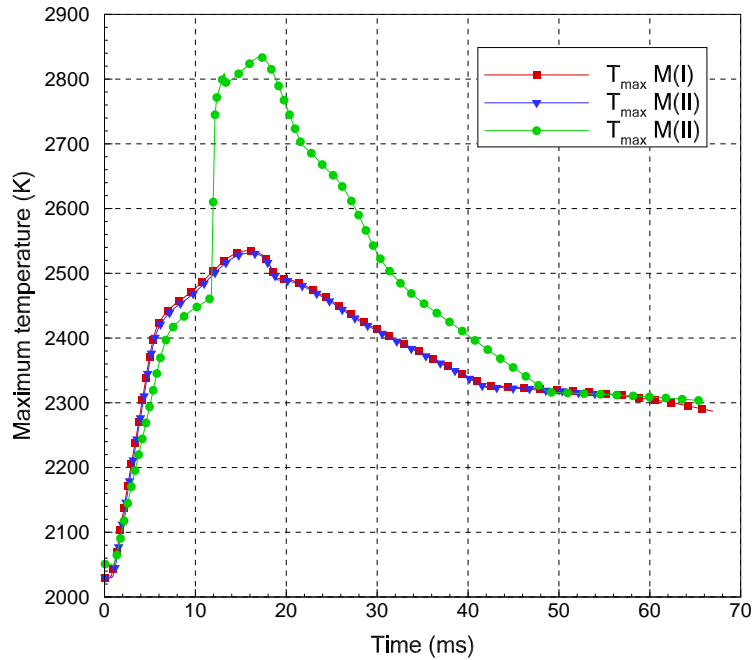


Figure 5.22: Peak temperature developed in the WDE channel under three different diffusion model $M(I)$, $M(II)$, and $M(III)$ for stoichiometric methane/air.

For syngas/air of $\phi = 0.7$ and hydrogen content 50% by mass, the Lewis number was estimated

for reactants at atmospheric pressure and room temperature. Since the mixture is lean, the Lewis number must be evaluated based on the fuel components (H_2 and CO) as D'ippolito (2015):

$$Le = \frac{\alpha}{X_{H_2} D_{H_2 m} + X_{CO} D_{CO m}} \quad (5.1)$$

Where α is the mixture thermal diffusivity ($\alpha = \lambda / \rho c_p$), $D_{H_2 m}$, $D_{CO m}$ is the diffusion coefficients of H_2 and CO into the mixture, respectively. Based on this analysis, the effective Lewis number is estimated to be 0.57.

The peak temperature and average pressure of case $M(III)$ exhibit moderate differences from $M(I)$ and $M(II)$ (Figs. 5.23, 5.24) possibly because the Lewis number for the syngas/air mixture is evaluated at the initial state ($Le = 0.57$) D'ippolito (2015).

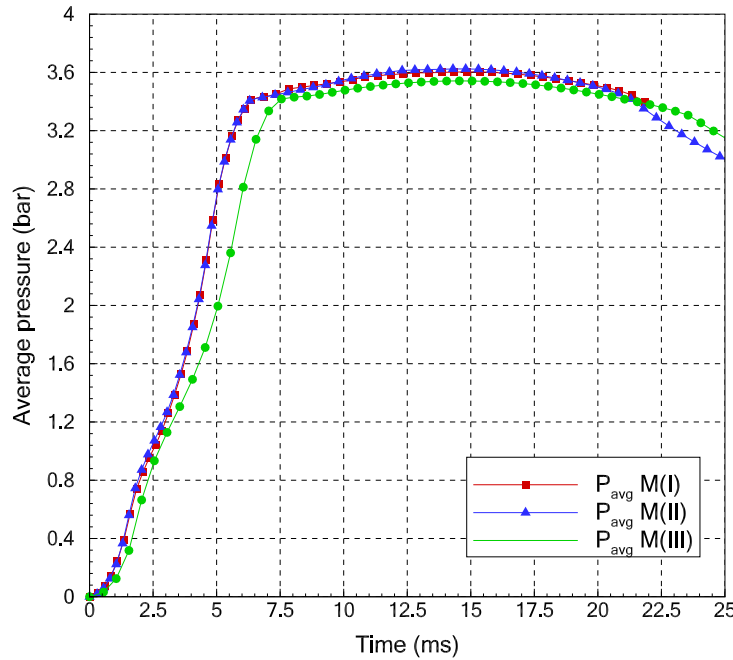


Figure 5.23: Average pressure developed in the WDE channel under three different diffusion model $M(I)$, $M(II)$, and $M(III)$ for syngas/air of $\phi = 0.7$ and 50% H_2 .

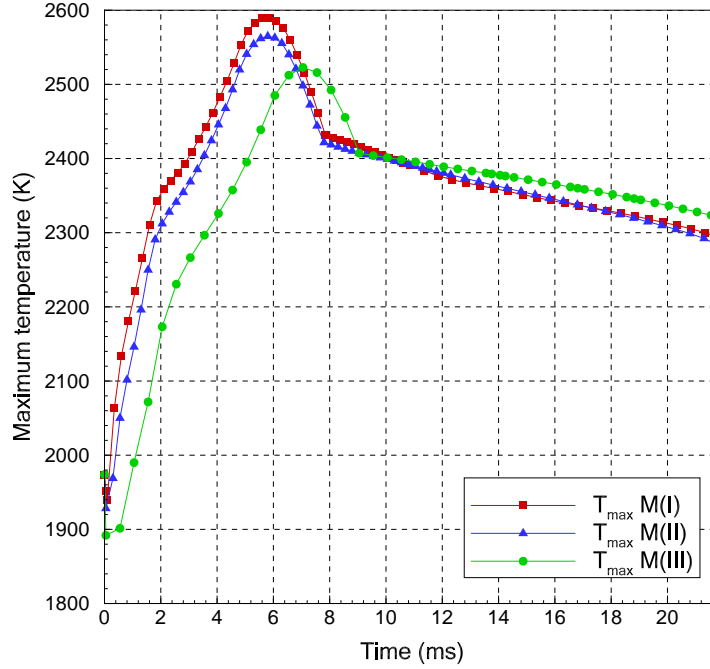


Figure 5.24: Peak temperature developed in the WDE channel under three different diffusion model $M(I)$, $M(II)$, and $M(III)$ for syngas/air of $\phi = 0.7$ and 50% H_2 .

The effective Lewis number can be formulated based on heat release, volume fraction, and diffusional properties of the main fuel components as reviewed by Bouvet et al. (2013). It is our understanding that all mixture species contribute to the overall transport of heat and mass, therefore the effective Lewis number is estimated based on the volume fraction of all individual species not only the fuel components. Thus we define $Le_{eff} = \sum_{k=1}^{N_s} X_k Le_k$. Figure 5.25 for the evolution of the effective Lewis number shows that the unburned methane/air mixture is nearly constant, approximately 1.139 during combustion. However, Le_{eff} decreases to between 1.10-1.02 close to the flame front in the unburned mixture (Fig. 5.25g): the species molecular diffusivity is lower than its thermal diffusivity. Since the front shape of the lower, dominant tulip flame tongue is convex toward the unburned gases, the reactants diffuse from a large to a small area thereby following a convergent path. This decreases the laminar flame speed below the planar flame value, see Figs. 5.25b-d. Consequently, this environment stabilizes the flame front and reduces the tendency

for it to fold Kadowaki et al. (2005), Poinso & Veynante (2005). It can be seen from Fig. 5.25g that the effective Lewis number is time dependent, showing different behaviors near the flame front before and after flow inversion.

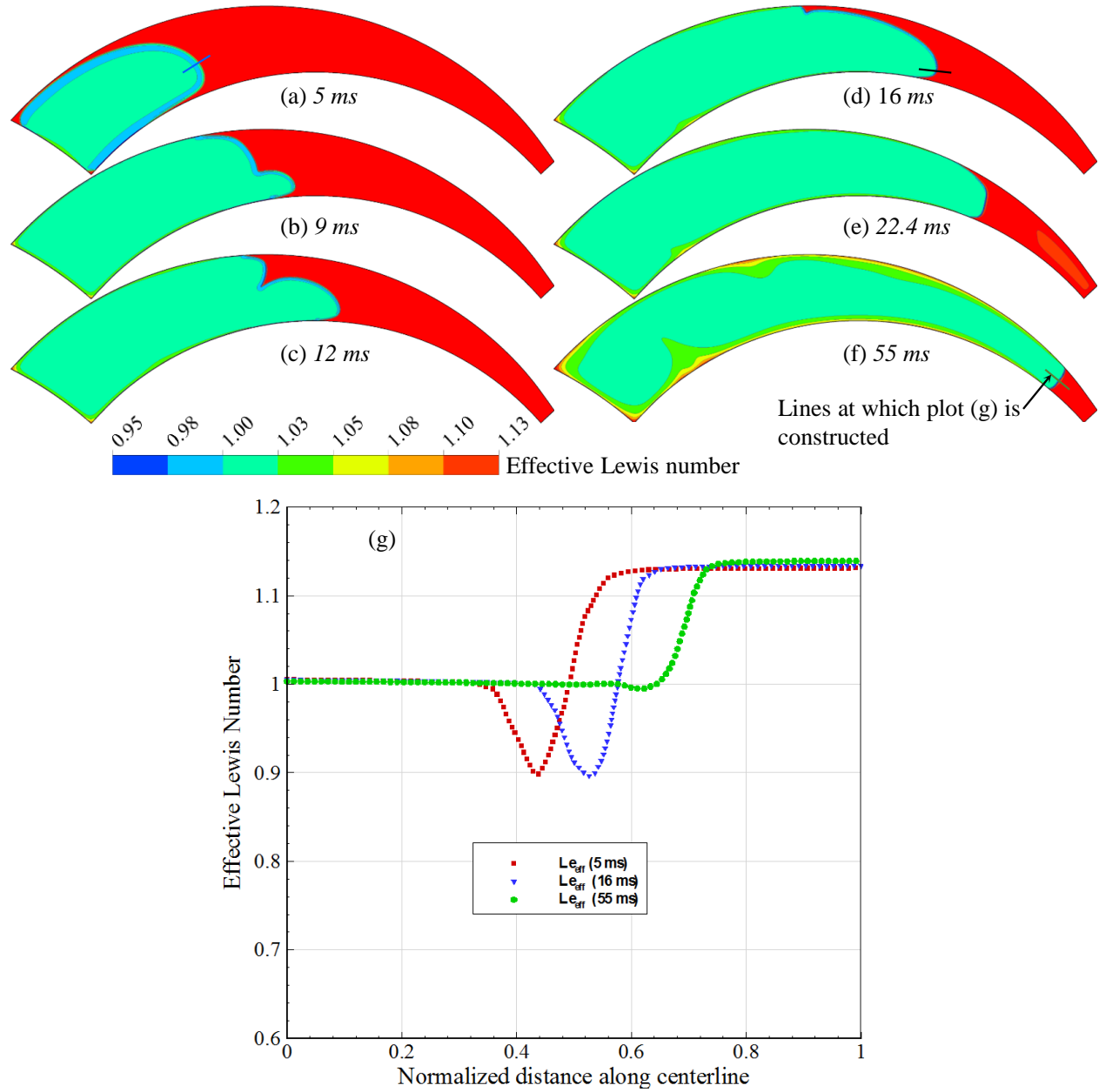


Figure 5.25: Evolution of effective Lewis number derived from case $M(II)$ for methane/air mixture at different combustion time.

After inversion (i.e. when thermodiffusive phenomena become dominant), Le_{eff} drops below

unity (~ 0.9) within the flame front. The progressively narrowing space at the end of the channel likely prevents the flame from folding and reproducing the tulip flame observed in constant cross section channels Xiao et al. (2012b). It can be deduced from these behaviors that the flame tendency to fold is increased by assigning $Le = 1$ to the fresh gases ahead of the flame front since its “natural” response is to develop a $Le < 1$ region in front of the flame (indicating more pronounced mass transport). This suggests that decreased mass transport favors the formation of the artificial folded flame of Fig. 5.3.

5.6 Characteristic Burning Regime

The discussion in Section 5.5 reveals three different burning regimes (Fig. 5.26). Regime (1) of dominant hydrodynamical phenomena, where the flame structure only slightly influenced by the diffusion, hence the $M(III)$ flame structure agrees with experimental observation; regime (2) of dominant thermodiffusion phenomena, where the diffusion model influences the flame structure and other thermochemical properties. In this regime, model $M(III)$ is insufficient and yield an unrealistic flame structure, peak temperature, and pressure; regime (3), in which the flame propagates slowly into the narrowing space ahead of it. The flame in Regime (3) is unable to produce a tulip flame but rather generates a concave (finger) flame. To characterize these regimes, we introduce the non-dimensional characteristic time ratio:

$$\mathcal{N} = \frac{\text{Hydrodynamic time scale}}{\text{Diffusive time scale}} = \frac{\frac{L}{U_{ave}}}{\frac{L^2}{D_{imave}}} = \frac{1}{U_{ave}L/D_{imave}} \quad (5.2)$$

Here, the characteristic length, L , is the local channel width, the volumetric average velocity magnitude, U_{ave} , the volumetric average mass diffusion coefficient between unburned and burned gases,

$D_{im_{ave}}$. Shown in Fig. 5.26 is a plot of the ratio $\mathcal{N}/\mathcal{N}_{(2)}$ where $\mathcal{N}_{(2)}$ is the value of \mathcal{N} in the Regime (2), versus the normalized time t/t_{max} . Consequently, $\mathcal{N}/\mathcal{N}_{(2)}$ has average value unity in Regime (2) but is large by a factor of ten in Regime (1), the hydrodynamic regime, and smaller by a factor of ten in the heat-loss Regime (3). The rescaled time variable ranges between zero and unity indicates that the bulk of the transition processes have ended at approximately 30% of the total burn time.

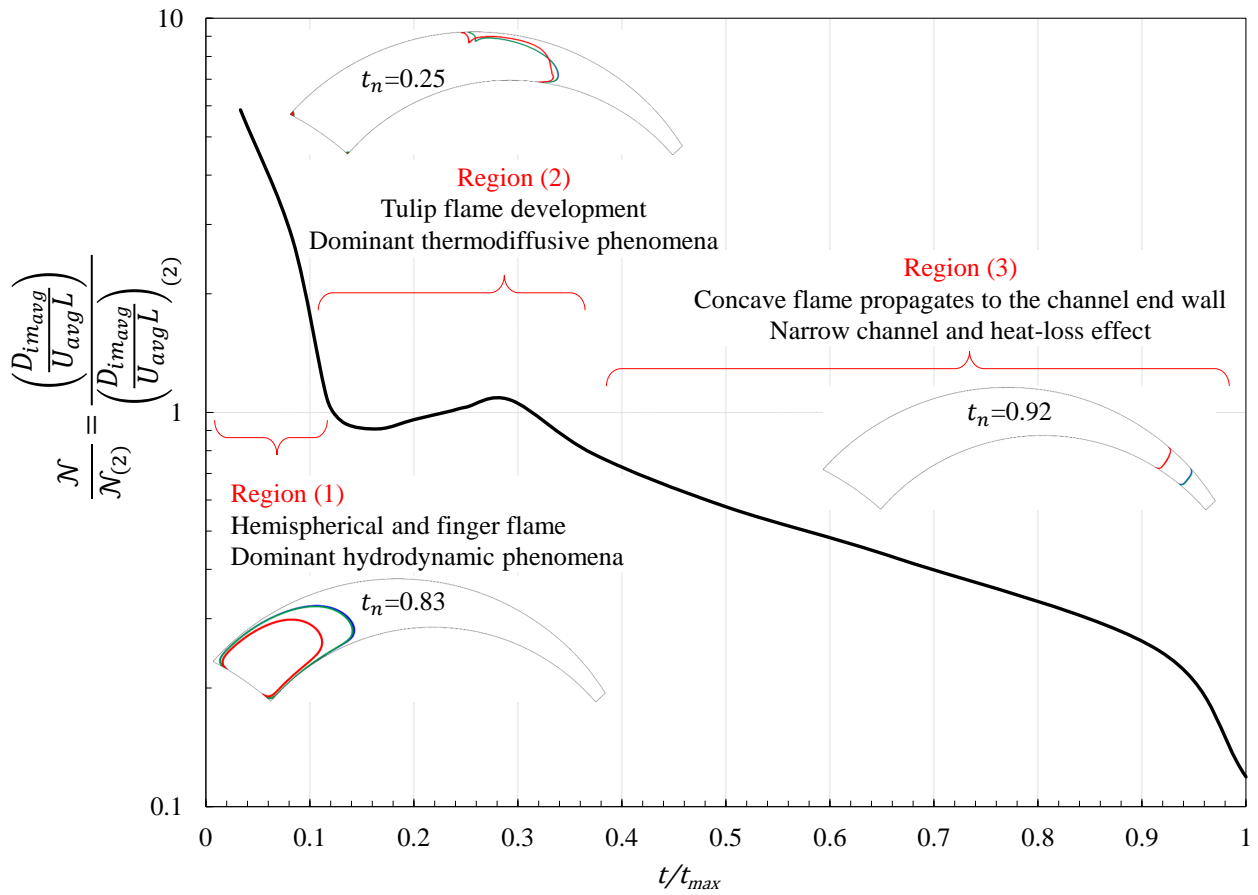


Figure 5.26: Normalized inverse Peclet number ratio $\mathcal{N}/\mathcal{N}_{(2)}$ versus normalized total time t/t_{max} . The hydrodynamic Regime (1), and the thermodiffusive Regime (2) occupy 10 and 20% of the total time. The heat-loss Regime (3) occupies the remaining 70% of the burn time.

5.7 Influence of Mixture stoichiometry on Syngas Flames

5.7.1 Flame structure

The evolution of syngas premixed flame structure propagating in a rectangular channel is described for nine (9) cases of different stoichiometry, see table 5.1. It be seen from Fig. 5.27 that the confined, premixed syngas flames exhibit several distinct modes. For all nine (9) cases, the process of syngas flame propagation in rectangular channel starts with hemispherical expansion of the flame kernel followed by elongated finger-shaped flame which expands axially and gains more surface area. A dramatic reduction of the flame surface area takes place after the flame skirt annihilated by the channel side wall leading to the formation of tulip flame with cusp pointing towards burned gases. This evolution of flame structure has been reproduced experimentally and numerically as we discussed before Ponizy et al. (2014), Dunn-Rankin & Sawyer (1998), Clanet & Searby (1996), Hariharan & Wichman (2014), Xiao et al. (2015), Xiao et al. (2012b), Jeung & Cho (1989), Dunn-Rankin et al. (1988), Matalon & McGreevy (1994). However, the syngas flames show unique structure evolution after the tulip flame is fully established, see Fig. 5.27 from 5.0 *ms* to 18 *ms*. The flames of C2, and C3 at 11 *ms* exhibit a unconventional structure where the tulip flame evolves into highly wrinkled, corrugated curved shape-flame and then to less wrinkled flame front and end up with laminar-like type of flame front with backward cusp when it get closer to the channel end wall. The results also indicates that the temporal change in syngas flame structure is highly dependent on the stoichiometric ratio and hydrogen content in the mixture (Fig. 5.27). The mixture stoichiometry affects the combustion time significantly. For example, the flame of C9 approach the channel end wall at 8.5 *ms* while for C1, it takes 28 *ms*, which means 3.3 times the time required for C9 (Fig. 5.28). As can be seen in Fig. 5.28, the rate of flame acceleration by increasing the hydrogen content in the mixture depends on the mixture stoichiometric ratio and

it is higher when $\phi = 0.7$ than $\phi = 1.5$. Also, when increasing the hydrogen content from 20% to 50%, the syngas flame accelerate much faster when hydrogen content in the mixture goes from 50% to 80%, see Figs. 5.29, 5.29

Mixture	Stoichiometric ratio	Hydrogen Content (% by mass)
C1	0.7	20
C2	0.7	50
C3	0.7	80
C4	1.0	20
C5	1.0	50
C6	1.0	80
C7	1.5	20
C8	1.5	50
C9	1.5	80

Table 5.1: Cases for syngas flame simulations.

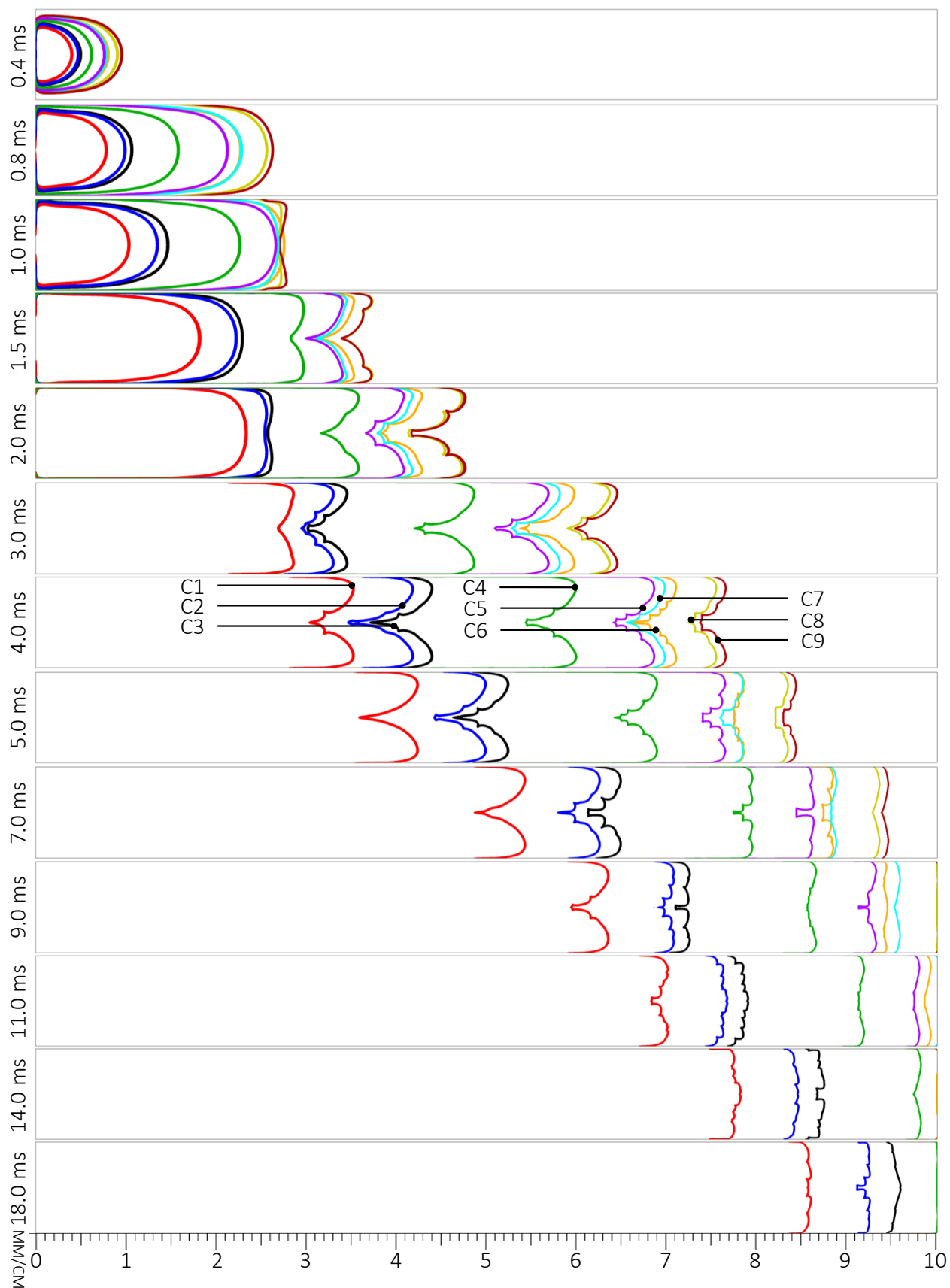


Figure 5.27: Syngas flame structure for different stoichiometric ratios and hydrogen content (C1-9).

Figures 5.27, 5.28, 5.29 reveal that the C9 mixture ($\phi = 1.5$ with 80% hydrogen content) produces faster flame propagation speed while the slowest propagation speed is produced by C1 ($\phi = 0.7$ and 20% hydrogen content). Since the laminar flame speed approaches maximum near the stoichiometric conditions for conventional hydrocarbon fuels, see Fig. 3.1, it becomes even more interesting when we see that the propagation speeds of rich mixture case C9 ($\phi = 1.5$, 80% H_2) is faster than stoichiometric mixture of C6 ($\phi = 1.0$, 80% H_2). This unique feature of syngas flame has a great impact on the industrial combustion chambers that working on syngas/air mixture. The analysis of one-dimensional, freely propagating syngas laminar flame reported by Sun et al. (2007), Singh et al. (2012) and Kèromnès et al. (2013) has verified this behavior (Fig. 3.2) in which the laminar flame speed for syngas approaches maximum at about $\phi = 2$. Figure. 5.27 also shows that the temporal evolution of flame structure for C9 is faster than other cases. It can be concluded from Fig. 5.28 that the propagation speed of syngas flames nonlinearly increases when the hydrogen content in the mixture is increased. It can be seen from Fig. 5.28, however, that propagation speed slightly increases when the hydrogen content goes from 50% to 80%.

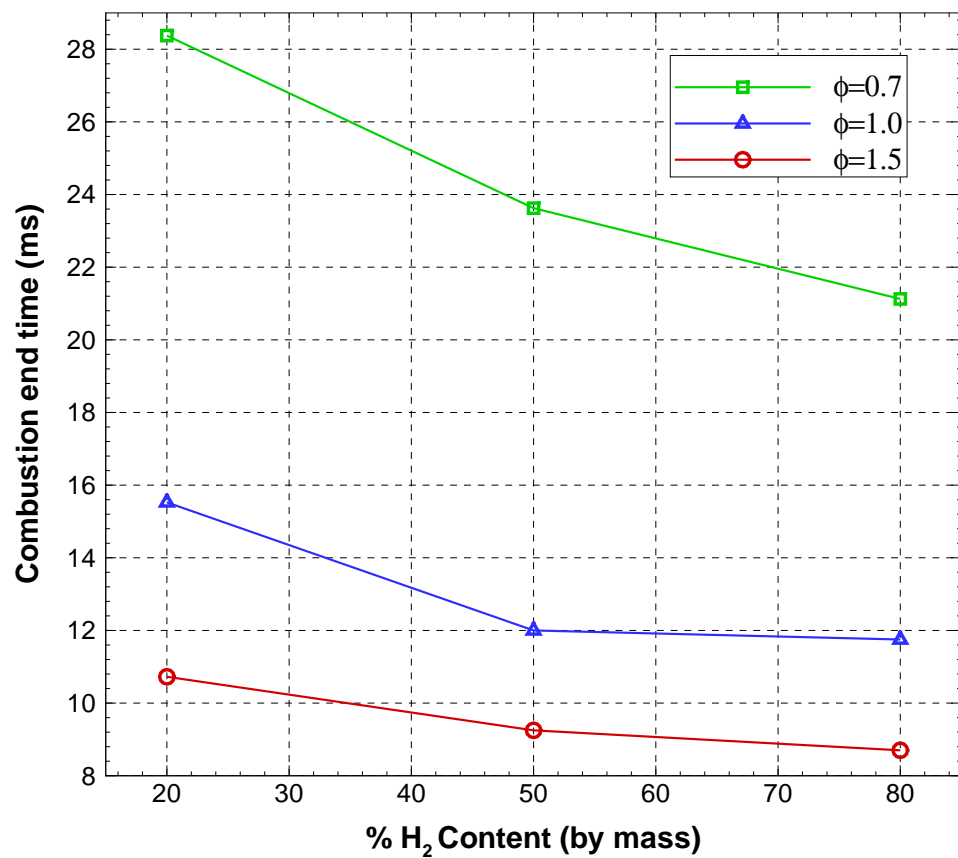


Figure 5.28: Syngas combustion time for different mixture stoichiometry.

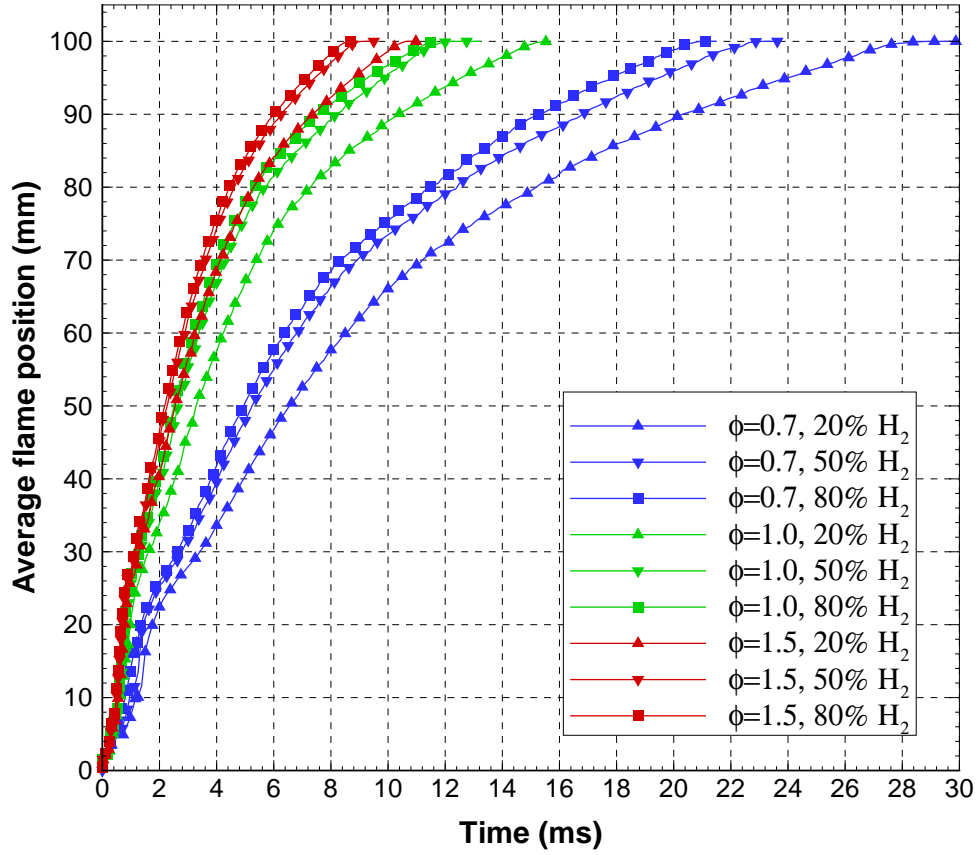


Figure 5.29: Instantaneous syngas flame distance for different mixture stoichiometry.

5.7.2 Pressure dynamics

The average pressure of the channel starts build up after the ignition kernel expansion and increases exponentially during the axial expansion of the finger-flame at around 0.07% of the combustion time, see Figs. 5.30, 5.31. The pressure time-history correlate with the evolution of associated flame structure as discussed in Sec. 5.7.1. Faster propagation speed, as in C9, result in higher rate of pressure increase and vice versa. The normalized average pressure is presented in Fig.5.31 which reveals that the pressure data collapsed regardless the stoichiometry and hydrogen content. By neglecting the short exponential increase of the pressure during the finger-flame expansion, a

conclude can be drawn from Fig. 5.31 such that:

$$\underbrace{\frac{p}{P_{max}}}_{\text{Normalized pressure}} = \underbrace{\frac{t}{t_{max}}}_{\text{Normalized time}} \quad (5.3)$$

Where p is the channel average pressure, P_{max} is the maximum average pressure attained, t is the time, and t_{max} is the time at which the flame approaches the channel end wall.

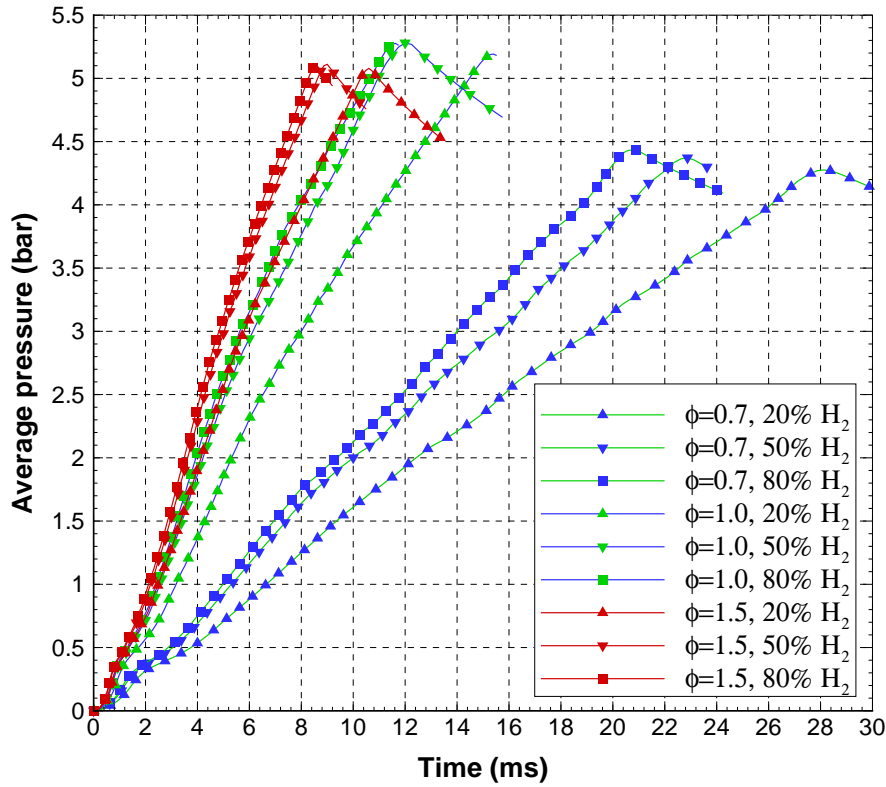


Figure 5.30: Time-history of the channel average pressure under different mixture stoichiometry.

This equation tells us that regardless the syngas mixture stoichiometry condition, the channel average pressure p at any time t can be estimated by knowing the maximum pressure and the combustion time. The maximum average pressure is mainly controlled by the heat released from combustion and the heat lost to the channel cold walls or the heat accumulated in the channel which result in increasing the average temperature and consequently increasing the average pressure since

the mixture average density remains unchanged due to CV combustion.

Same behavior is obtained with the normalized instantaneous flame front distance presented in Fig. 5.32. It can be concluded that the temporal instantaneous flame front distance collapse when normalized by the channel length (100 mm) and plotted versus the normalized time. Furthermore, this behavior is verified experimentally for stoichiometric methane/air flame propagating in a rectangular channel, see Fig. 4.6.

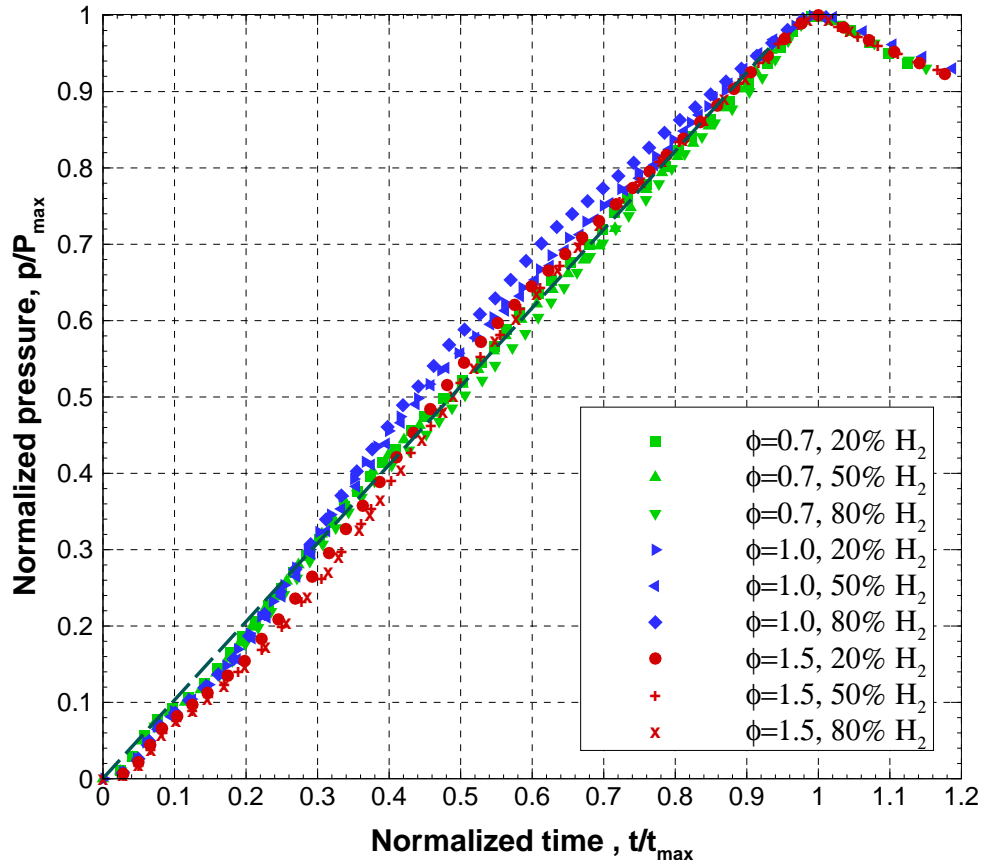


Figure 5.31: Time-history of the normalized pressure under different mixture stoichiometry.

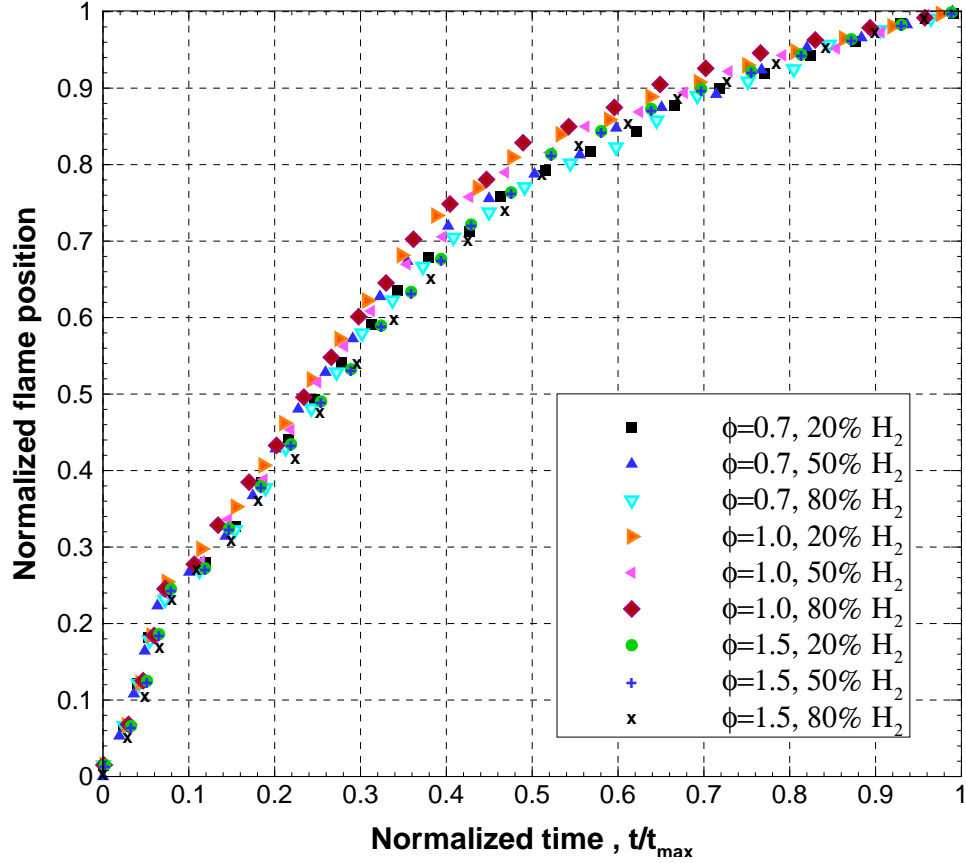


Figure 5.32: Normalized syngas flame distance for different mixture stoichiometry.

5.7.3 Flame-flow interaction

The interaction between flame front and flame-induced flow for different combustion time and hydrogen content are presented for $\phi = 0.7$, $\phi = 1.0$, and $\phi = 1.5$ in Figs. 5.33, 5.34, and 5.34, respectively. It is evident from these figures that the different mixtures stoichiometry develop different flame front structure and subsequent flame-induced flow pattern. All mixtures produces the conventional tulip flames with two tongue pointing towards the unburned gases and one cusp pointing towards the burned gases. With the increase of hydrogen fraction for same equivalence ratio, the flame wrinkles tend to increase on the flame front while it decreases with the increase of the stoichiometric ratio. This agrees with the experimental observations of the spherical syngas

flame propagation in closed chamber conducted by Li et al. (2014). It is also evident that the flame wrinkles and flame instabilities decreases when the pressure build up before the combustion ends which has never been reported in the literature. The flames of $\phi = 0.7$ and $\phi = 1.0$ develop a convex front at the end of the combustion time after the flame approaches 80-90% of the channel length while the flame of $\phi = 1.5$ develops a concave-like shape and for all hydrogen content fraction.

Figures. 5.33, 5.34, 5.35 show that the flow intensity increases with the increase in the mixture stoichiometric ratio and hydrogen mass fraction due to the increase in laminar flame speed which, in turn, increases the reaction rate.

The vortical flow is formed in the burned gases region behind the tulip flame cusp is more pronounced for mixtures of $\phi = 1.0$ and $\phi = 1.5$ (Figs. 5.34, 5.35). The results show that stagnation points develop behind the tulip flame tongues in the burned region which remarks the flame tendency to fold at that region.

The flame propagation speed decelerates near the channel end wall due to the high pressure developed in the closed channel. The impact of high pressure on the flame front structure depends on stoichiometric ratio. When the syngas/air mixture is rich ($\phi = 1.5$), the high pressure smooths the flame front and the flame tend to be a laminar-like flame at the end of the combustion and for different hydrogen content (Fig. 5.35). On the other hand, the flame still generates a wrinkled front in the high pressure environment when the mixture stoichiometric ratio is 0.7 and less wrinkled front is seen for mixture of $\phi = 1.0$.

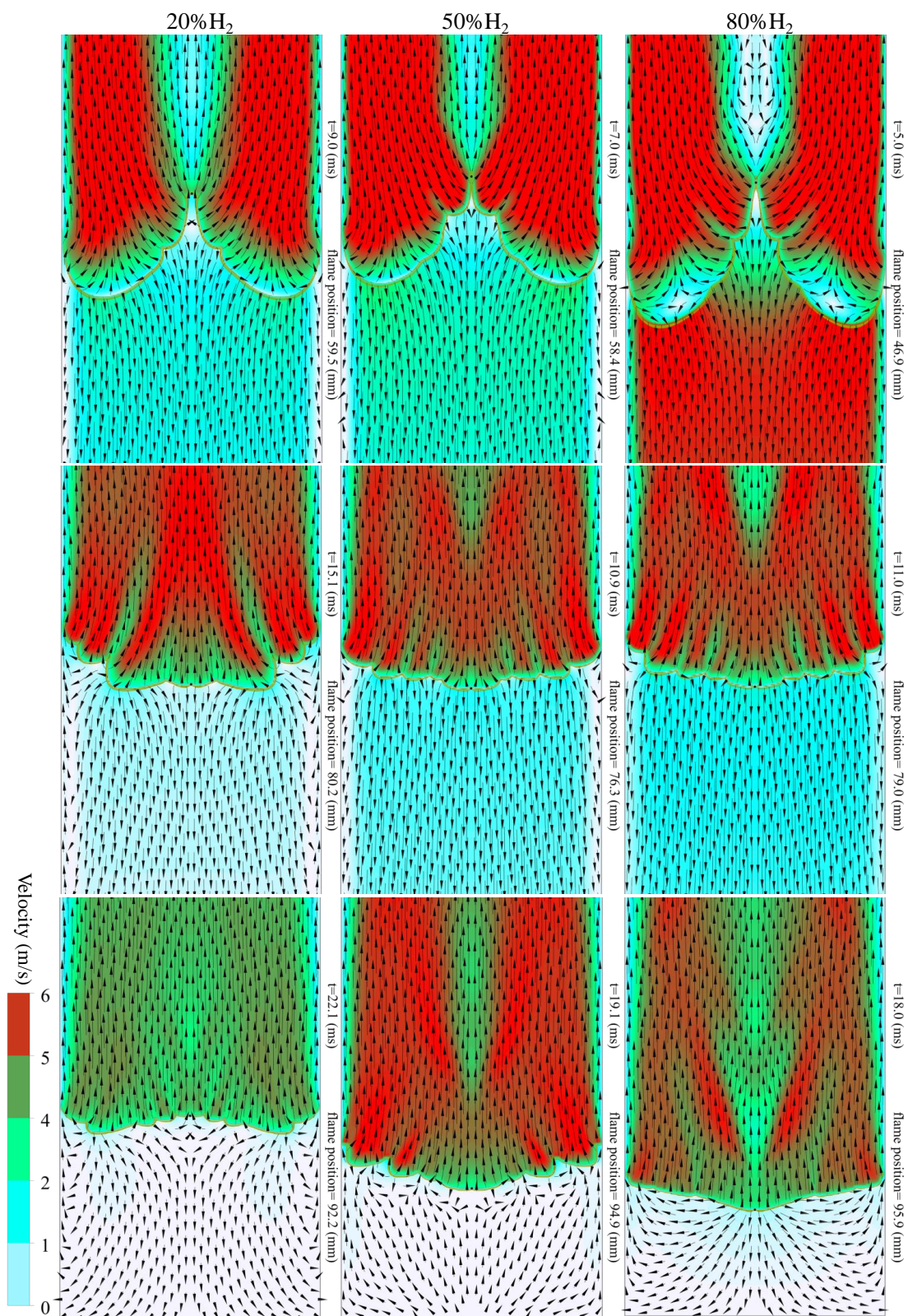


Figure 5.33: Flame front interaction with flame-induced flow for stoichiometric ratio of 0.7 for different combustion time, hydrogen content, and flame front position at the channel centerline.

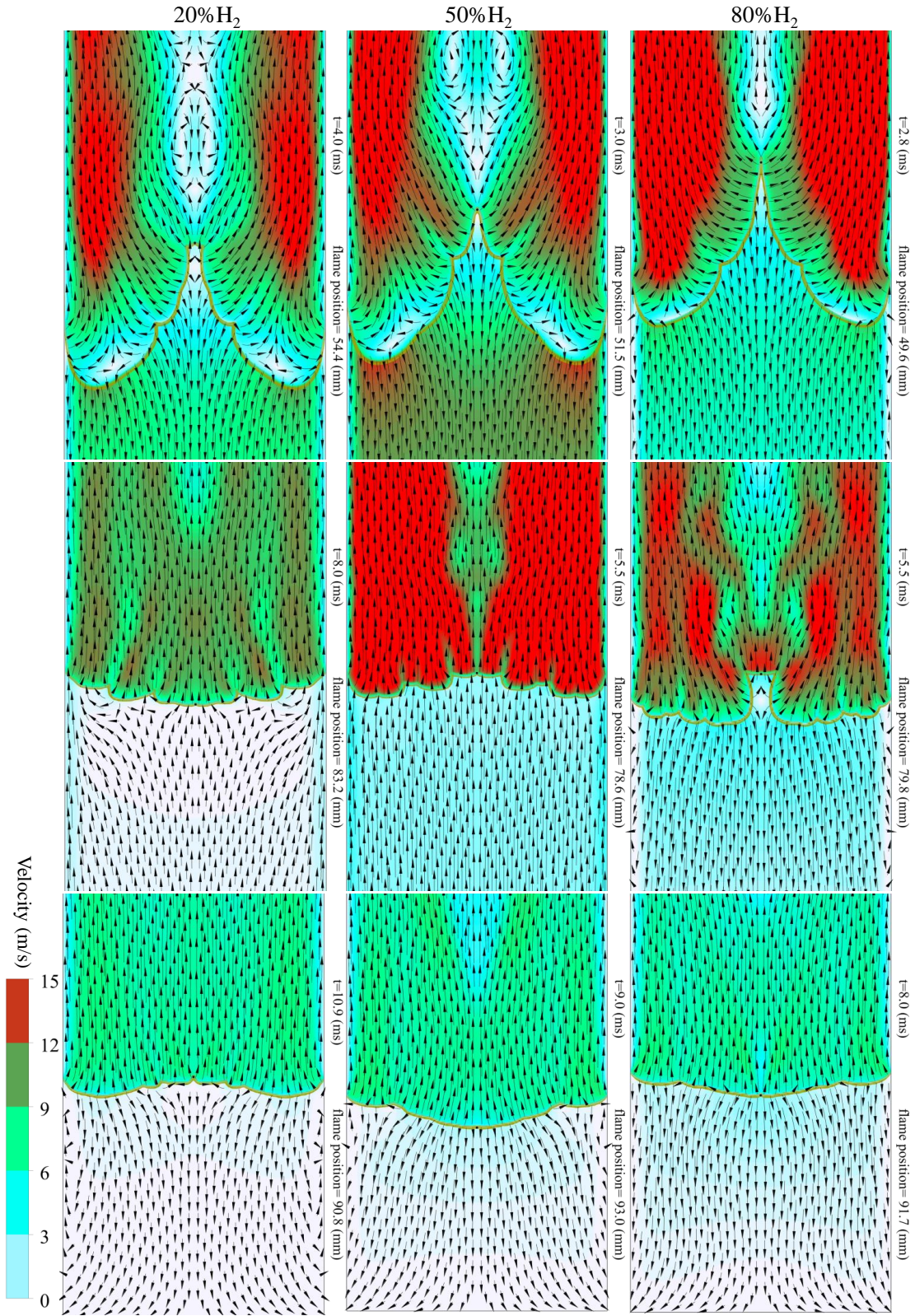


Figure 5.34: Flame front interaction with flame-induced flow for stoichiometric ratio of 1.0 for different combustion time, hydrogen content, and flame front position at the channel centerline.

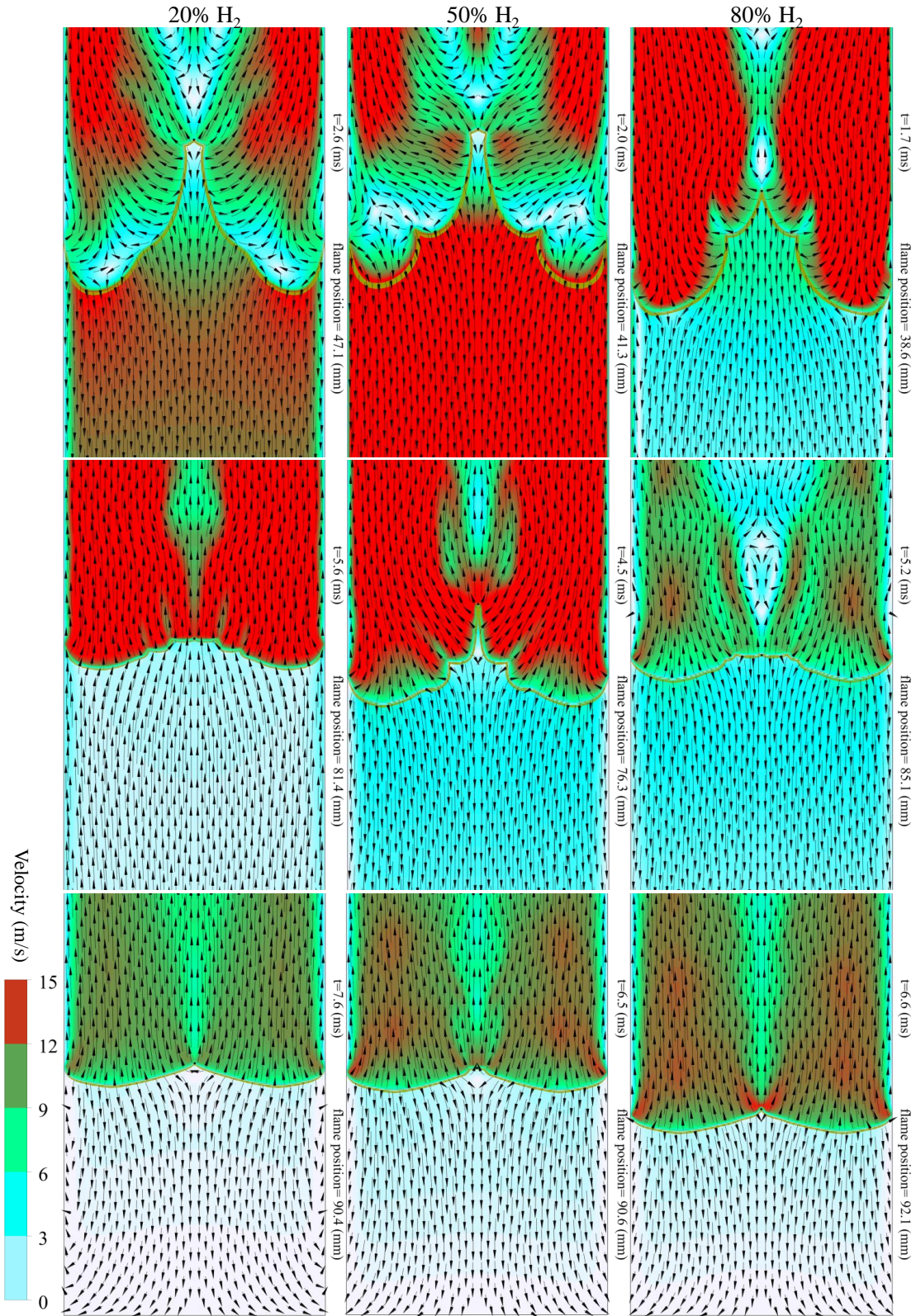


Figure 5.35: Flame front interaction with flame-induced flow for stoichiometric ratio of 1.5 for different combustion time, hydrogen content, and flame front position at the channel centerline.

Chapter 6

FLAME SURFACE DENSITY FOR LES

6.1 Three-Dimensional Structure of the Flame Front

6.1.1 Transverse tulip flame

Figure 6.1 shows the structural evolution of three-dimensional premixed flame propagating in a closed-curved channel. After ignition, the flame expands hemispherically with approximately constant flame speed. Finger flame then takes place at 4.5 ms with the flame front deflected toward lower sidewall. During this time, the burned and unburned gases are moving away from ignition location due to burned gases expansion. The flame touches the inner sidewall at approximately 5 ms and the outer sidewall at 6 ms , and the bottom and top sidewalls at about 8 ms . Once the flame touches all sidewalls, the burned gases flow is inverted toward ignition location causing a dramatical deceleration in flame propagation speed. As a consequence, the saddle points moves closely to the flame front, see Fig. 6.1-d. At this time, the non-symmetric tulip flame on the lateral xy plane starts developing to cusped convex shape with large lower tongue near inner sidewall and small rounded tongue near outer sidewalls (Fig. 6.1-e). During the time 20 ms , the three-dimensional simulation conducted here uncovers an interesting behavior for the flame structure on the xz plane. We observed what may be referred as a “*transverse tulip*” flame which is developed in the direction perpendicular to that of the initial tulip flame after the latter underwent the transition from cusped convex back to concave finger shape. This “*transverse tulip*” flame is symmetric across

transverse xz planes and it has two tongues which accelerate near the sidewalls while the concave finger flame in the xy plane, at $z=0$, decelerates and lags behind. During the combustion time 22-40 *ms* the “*transverse tulip*” flame tongues start growing by moving forward and toward the channel centerline. At the time when the two tongues are about to touch each other at the channel middle xy plane, the finger flame in the middle plane experiences minimum propagation speed (approaching zero). This leads to more pronounced cusp pointing toward burned gases for the “*transverse tulip*” flame which continues into a tulip shape that persisted to the end of the channel. The flame-induced flow on the transverse xz plane shows dramatic pattern changes through the evolution of “*transverse tulip*” flame. The burned gases flow patterns are driven by the difference in burned gases velocity produced by the flame tongues, which produces higher velocity, and near cusp region, which is of low burned gases velocity, see Fig. 6.1. The flow patterns behind “*transverse tulip*” flame can be characterized by vortical motion that continuously changes depending on the structure of the “*transverse tulip*” flame.

The comparison between experiments and numerical simulation results indicates that the algebraic flame surface density with Metghalchi-Keck correlation for flame speed are capable of reproducing the main features of flame structure and propagation speed, see Fig. 6.2 a-d. The initial tulip flame cusp predicted by numerical simulation, however, appears more rounded and smoother than experiment (Fig. 6.2 d) and San Diego kinetic mechanism reported in Najim et al. (2015) because of the coarse mesh used here to afford the three-dimensional model which in turn diffuses and smooths the relatively sharp changes that taking place in flame front. The “*transverse tulip*” flame can be observed in Fig. 6.2 f, in which the two tongues of “*transverse tulip*”, at $z = 7.25 \text{ mm}$, are leading the finger concave flame in the middle plane ($z = 0 \text{ mm}$) and hence they seem clearly in the experiment shadowgraph in contrast with the finger flame which hiding behind and appears faint and fade.

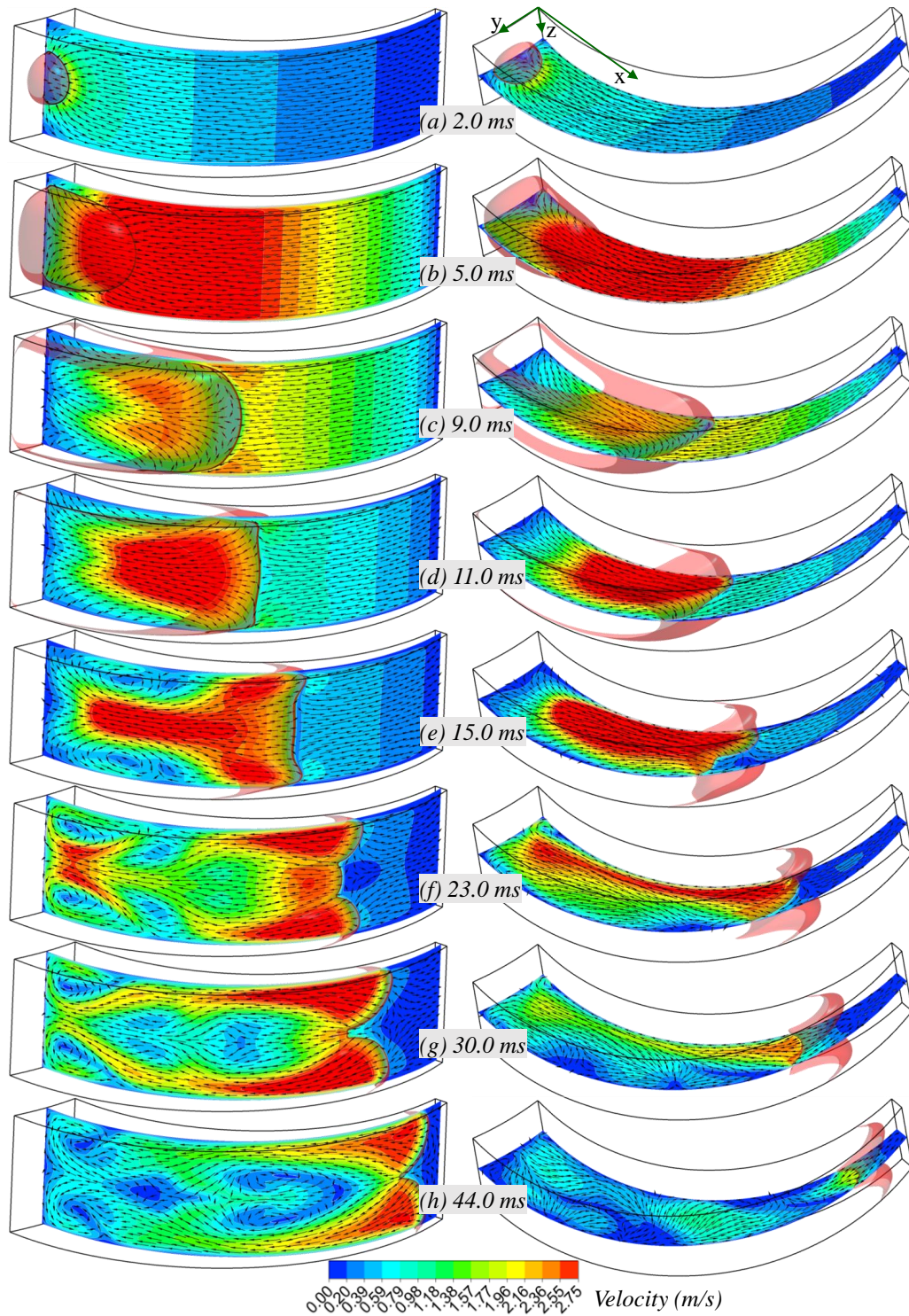


Figure 6.1: Flame structure evolution; (a) hemispherical flame, (b) finger flame, (c) skirt flame (d) straight flame front on transverse plane and concave flame on lateral plane, (e) non-symmetric tulip flame on lateral plane, (f) initial tulip flame back to concave finger shape (g-h) transverse tulip flame.

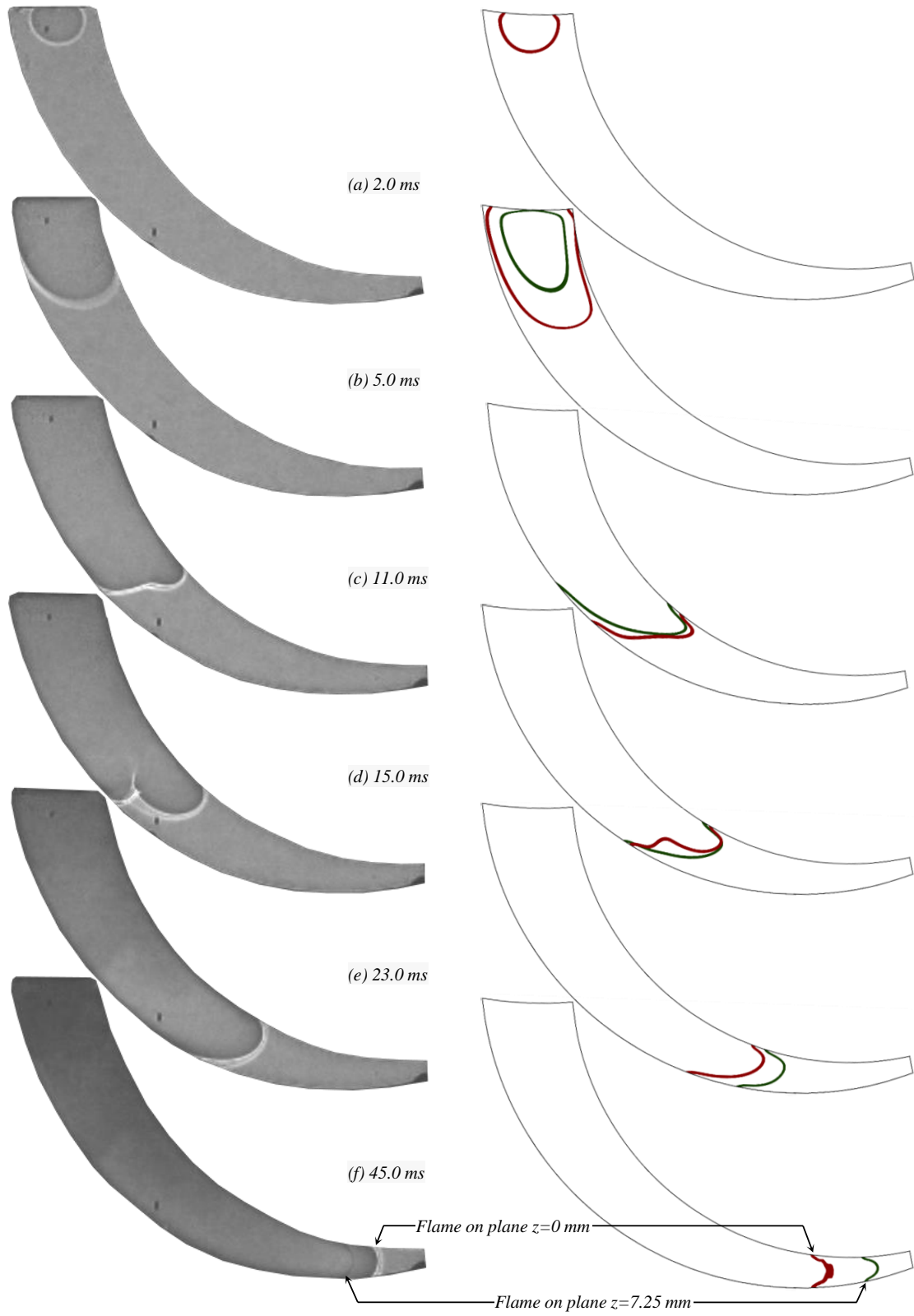


Figure 6.2: Experiment flame front shadowgraphy (on the left side) and numerical simulation flame front on plane $z = 0$ mm and $z = 7.25$ mm projected on one plane (on the right side).

6.1.2 3D flame dynamics in a rectangular channel

Figures 6.4, 6.3 indicate that the algebraic flame surface density modified by incorporating the temporal change in the unburned gases temperature and pressure is capable of reproducing the main features of the premixed flame propagating in a closed rectangular channel which was reported in Hariharan & Wichman (2014); Ponizy et al. (2014); Xiao et al. (2015). As described previously, flame expands hemispherically after ignition with approximately constant flame propagation speed (Fig. 6.3-a). The flame then takes elongated finger-shape and accelerates dramatically in the axial direction gaining more surface area. During finger flame phase, the burned gases produced from the lateral flame near the channel sidewalls moves toward the centerline of the channel and is then deflected axially along the channel centerline toward the flame front, in the same direction of unburned gas moving ahead of the flame as shown in Fig. 6.3-b. This flow pattern produces a saddle point near ignition point, see Fig.6.4 at approximately 20 *ms*. When the flame skirt is annihilated by the channel sidewalls, which rapidly reduces the flame surface area and reaction rate as well, the flame front flattens and experiences minimum propagation speed, see Fig. 6.4. The burned gases flow is inverted toward ignition location after most the lateral flames are annihilated by the channel sidewalls while the unburned gases continues to move towards the channel end wall, see Fig. 6.3-c. At this time, the saddle point moves close to the flame front which indicates the tendency of flame to fold. When saddle point approaches the flame front, the flame structure starts a transition from convex to concave and end up with a cusp pointing to the burnt region followed by the formation of tulip flame as shown in Fig. 6.3-d. At this time, the saddle point moves next to the flame front in the unburned region. The tulip flame propagates with nearly constant speed to the channel's end wall and saddle point moves slowly away from the flame front towards unburned region, see Fig.6.4.

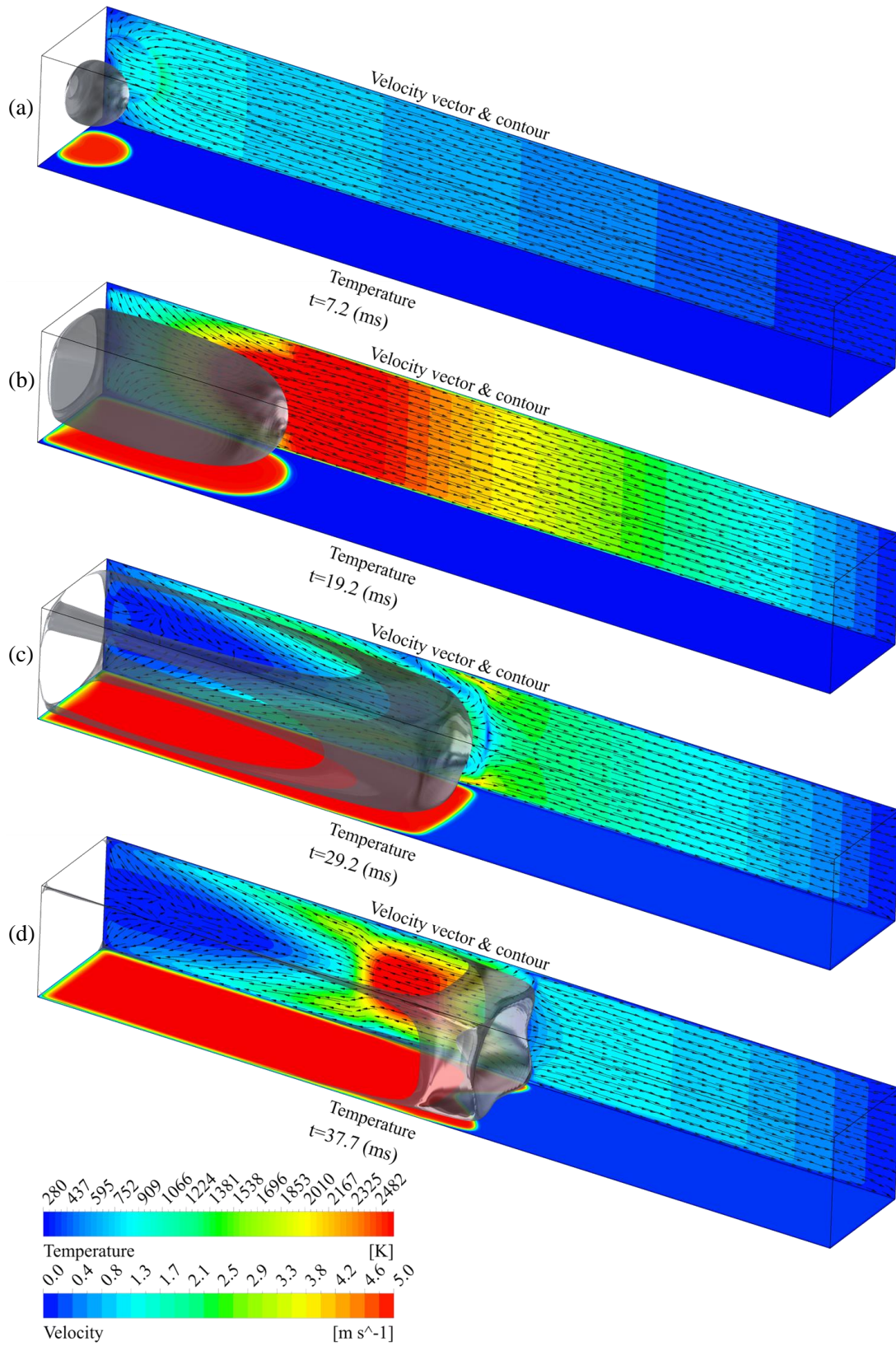


Figure 6.3: Three-dimensional, flame front structure developed in a rectangular chamber. (a) spherical expansion of ignition kernel, (b) finger-flame expansion, (c) skirt-flame, (d) tulip-flame.

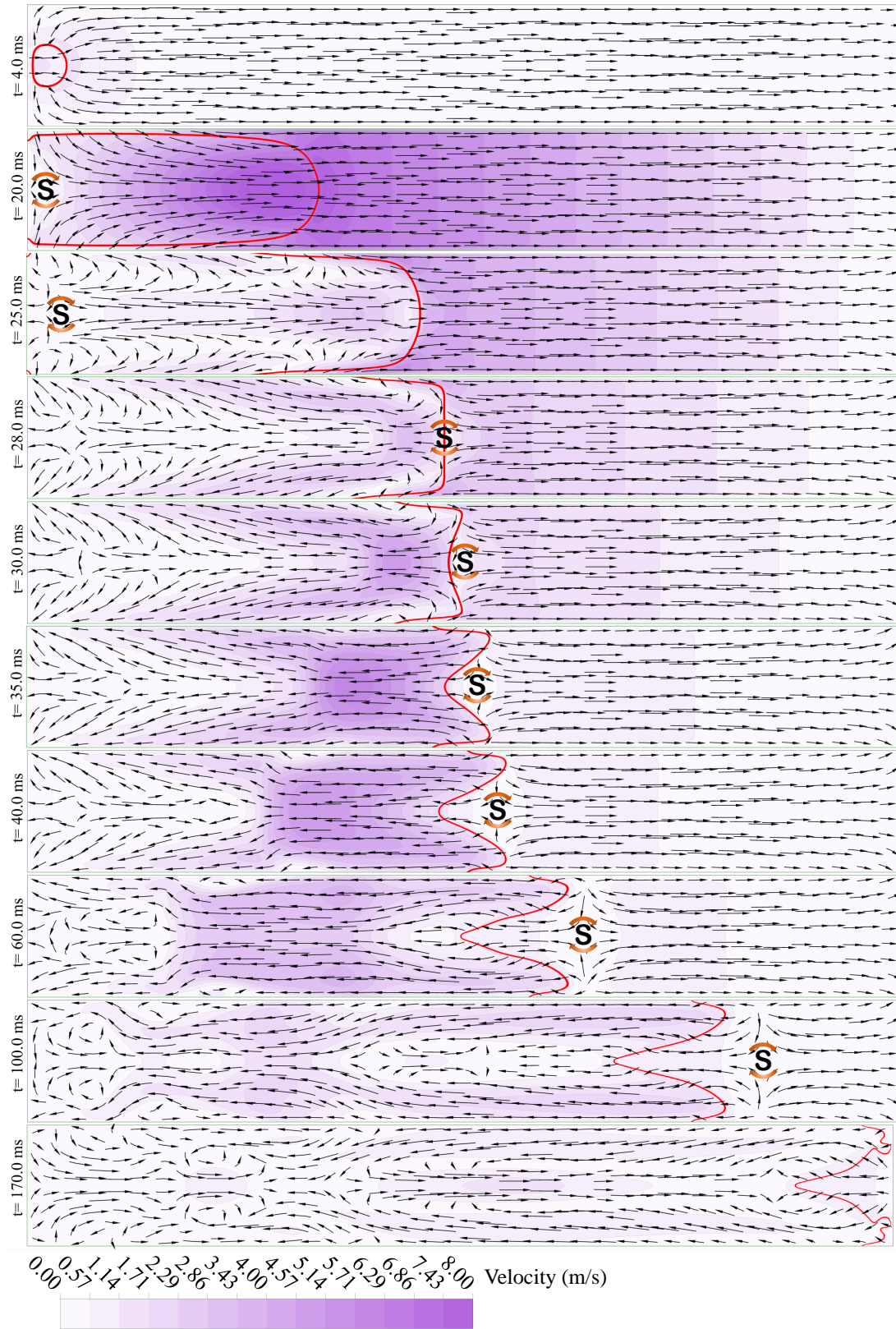


Figure 6.4: Evolution of flame structure, flame-induced flow, and dynamics of saddle point.

6.1.3 Flame surface density

The flame surface density area shown in Figs. 6.5, 6.6 provides important information about how the evolution of flame structure affects the flame surface area and consequently the reaction rate. The flame surface density has a unit of $\frac{1}{m}$ which represents the flame area per unit volume evaluated at each computational element. The result in Figs. 6.5, 6.6 indicates that the flame surface significantly increases during the finger-shape flame expansion (Figs. 6.5, 6.6) in which the flame expands in all direction gaining more flame surface area which appears clearly before 6 and 20 *ms* in Fig. 6.5 and Fig. 6.6, respectively. A rapid reduction in flame surface density is seen when the flame approaches the channel cold walls and loses the lateral parts of its surfaces which dramatically reduces the flame surface density and so affects the reaction rate as well, see Figs. 6.5, 6.6. The flame surface area slightly increases when the lower tongue of the initial tulip grows toward the outer sidewalls at approximately 15 *ms* for the WDE channel, which is about the time when the two tongues of “*transverse tulip*” flame grow forward and toward channel middle plane (Fig. 6.5). When the initial tulip flame back into finger concave shape and “*transverse tulip*” flame is developed, the flame surface area decreases at a constant rate which accounts for the convergence of channel walls. Similar behavior can be seen in the rectangular channel when the flame surface density increases again at a low rate after the two tongues of the tulip flame accelerate axially faster than the flame cusp which results in net increase in flame surface area at approximately 48 *ms*, see Fig. 6.6. It is evident from Figs. 6.5, 6.6 that the reaction rate is highly dependent on the flame surface density and both have almost the same structure which emphasizes the importance of flame surface density in combustion modeling.

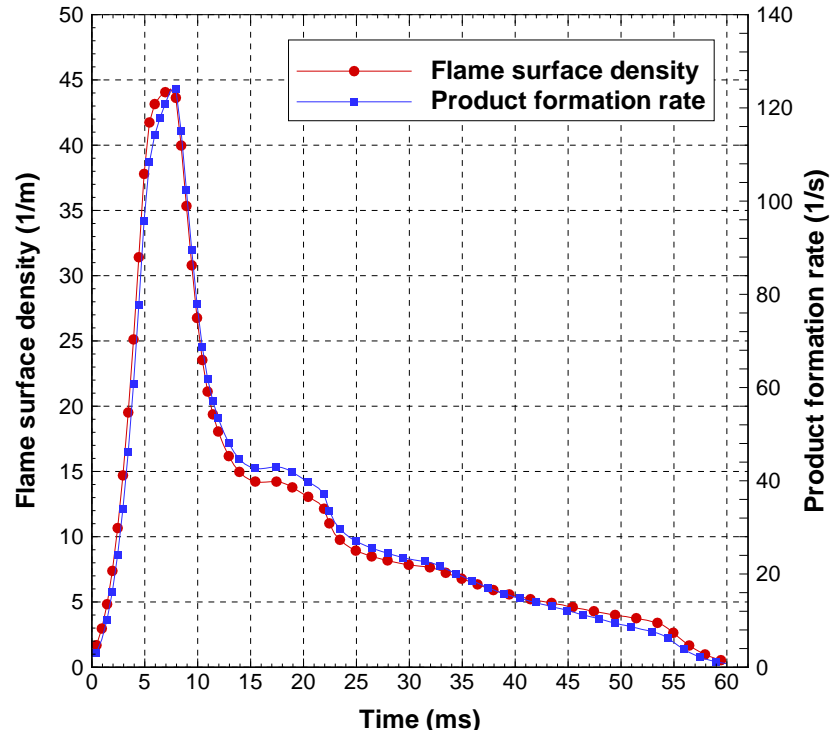


Figure 6.5: Flame surface density and product formation rate for WDE channel.

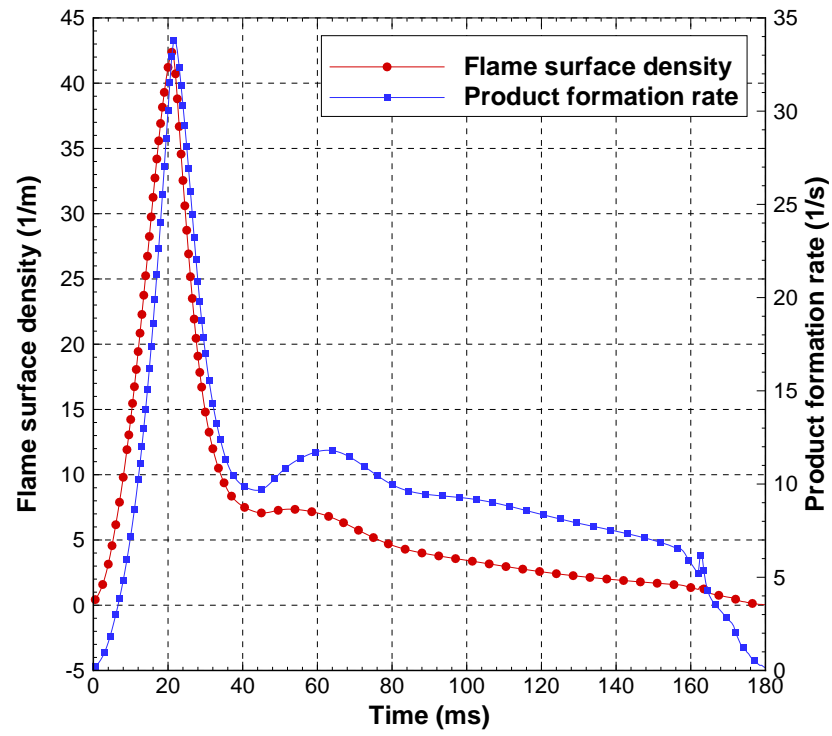


Figure 6.6: Flame surface density and product formation rate for the rectangular chamber.

6.1.4 Turbulent flame speed

When a premixed flame starts accidentally in quiescent mixture and propagates through confined chambers, the temperature, pressure, and density of the unburned gases vary considerably during the combustion time(Figs. 6.8, 6.10). To reproduce an appropriate flame propagation speed, the temporal change of temperature and pressure of the mixture need to be incorporated. The laminar flame speed is proportional to transient temperature and inversely proportional to the transient average pressure of the unburned gases Metghalchi & Keck (1980), Turns (2012). However, the net effect of this combination works in favor of the flame speed because of the coupling between pressure and temperature in a constant volume combustion. Therefore, the flame speed shows high dependence on the unburned gases temperature and both reach maximum before the initial tulip flame backs into finger concave flame at approximately 22.5 *ms*, see Figs.6.7, 6.8. This is because the exponent of unburned gases temperature term in Eq. 3.54 is higher than the exponent of pressure term by order of magnitude. The details on determining the temporal unburned gases density is presented in Appendix. B. Other turbulent flow parameters are not incorporated in the flame speed model since the flame starts in quiescent mixture and generates flow with low turbulence intensity, see Appendix B.

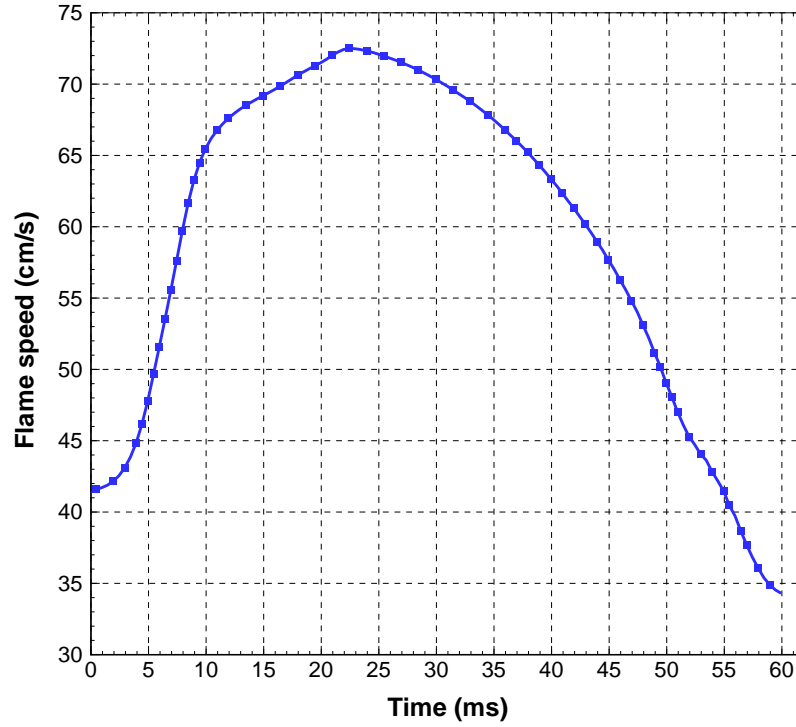


Figure 6.7: Variation of flame speed during the flame propagation in the WDE channel.

When the flame approaching the channel end wall, the net effect of transient unburned gases temperature and pressure works against flame speed which becomes even less than the reference value of the laminar flame speed for stoichiometric methane/air mixture (S_{lref}) at 55 ms (Fig. 6.7). This behavior agrees with the experiment and numerical simulation presented in Section 5.2.

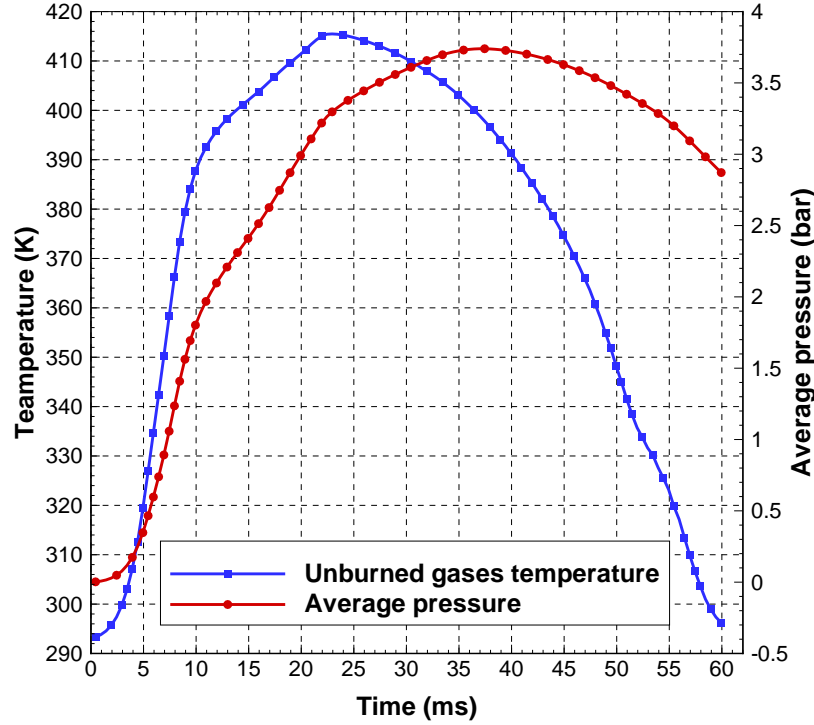


Figure 6.8: Temperature of unburned gases and average pressure developed in the WDE channel.

The variation of flame speed during the combustion in a rectangular channel shows different behavior as shown in Fig. 6.9, which implies that the combustion chamber geometry influence the flame speed. The flame speed in a rectangular channel also shows a strong dependence on the unburned mixture temperature with four (5) distinct regions. (1) in this region, the flame speed remains almost constant with the standard laminar flame speed (S_{lref}) up to around 8 ms, (2) exponential acceleration in flame speed following the increase in the unburned region temperature by compression effect and last up to 32 ms, see Figs.6.9, 6.10 (3) the flame speed then increases at about constant rate between 40-140 ms, (4) the flame speed decreases when the temperature of the unburned gases decreases due to heat losses to the channel walls, (5) when the flame approaches the channel end wall, the temperature of the remaining unburned mixture trapped between the flame and the wall increases again by the heat transport due to conduction and mixing which increases the flame speed again short before the flame annihilation at the channel end wall.

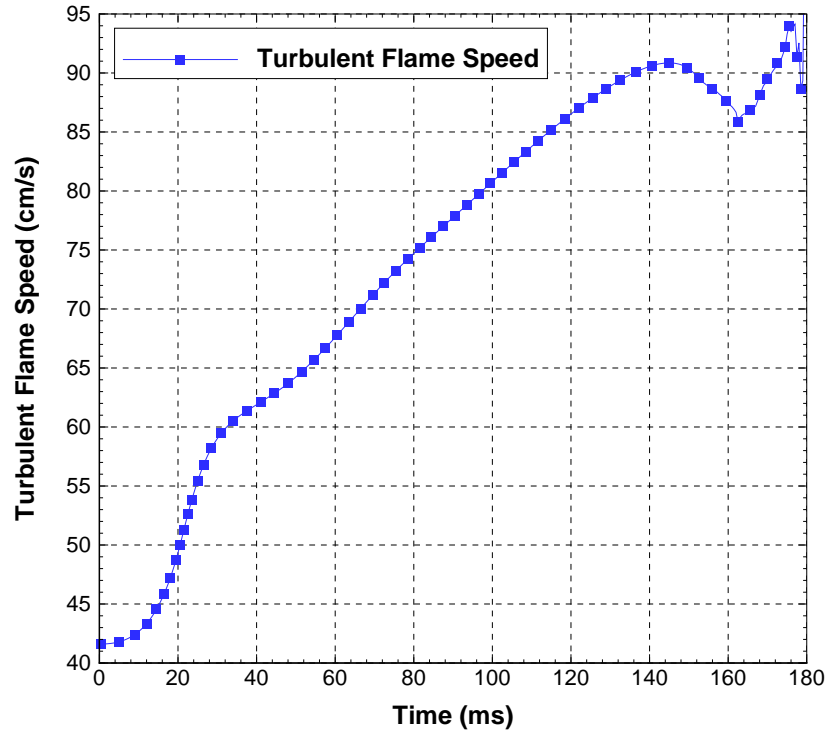


Figure 6.9: Transient flame speed developed in a rectangular channel.

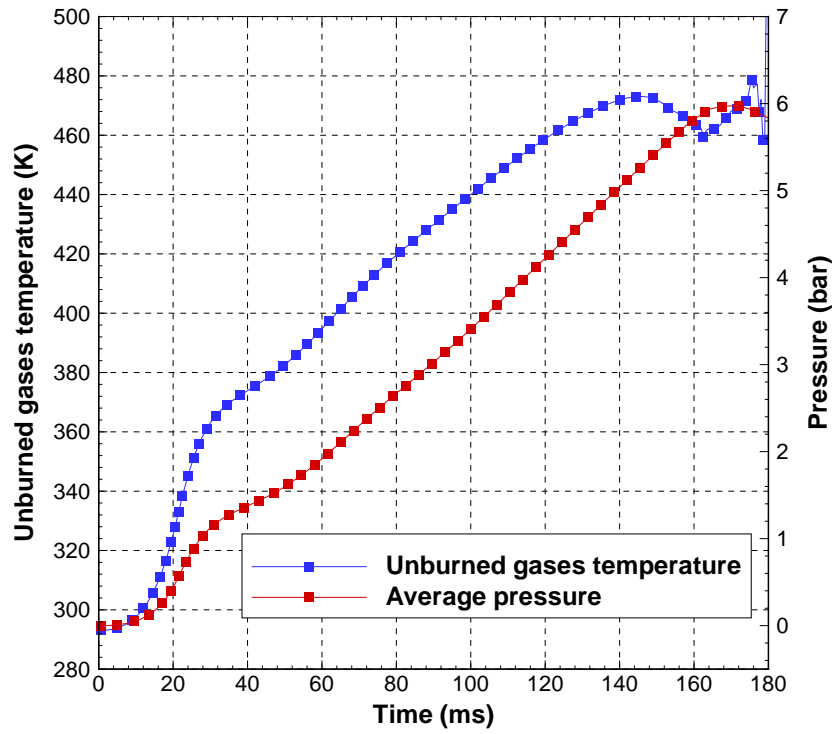


Figure 6.10: Unburned gases average temperature and pressure for premixed flame propagating in the rectangular channel.

6.1.5 Assessment of AFSD

As we mentioned in Section 3.2.2 that the concept of flame surface density is originally derived for reacting flow that is characterized by high mixing intensity. The comparison of numerical simulation results with the experimental data for the rectangular chamber verified that this model successfully reproduces the main features of the confined premixed flame. The model is in good agreement with the experimental observation during hemispherical and finger flame expansion as shown in Fig. 6.12 a-c. The model, however, overpredicts the time at which the flame flattens (Fig. 6.12 d). This might be due to a deficit in the prediction of flame extinction on the channel sidewall which requires detailed information about chemical reactions and species transport that we dismissed in the methodology conducted here.

The pressure time-history curve shown in Fig. 6.11 demonstrates that the model is sufficient for describing the reaction rate and the associated combustion time which is coupled with average pressure developed and other mixture properties.

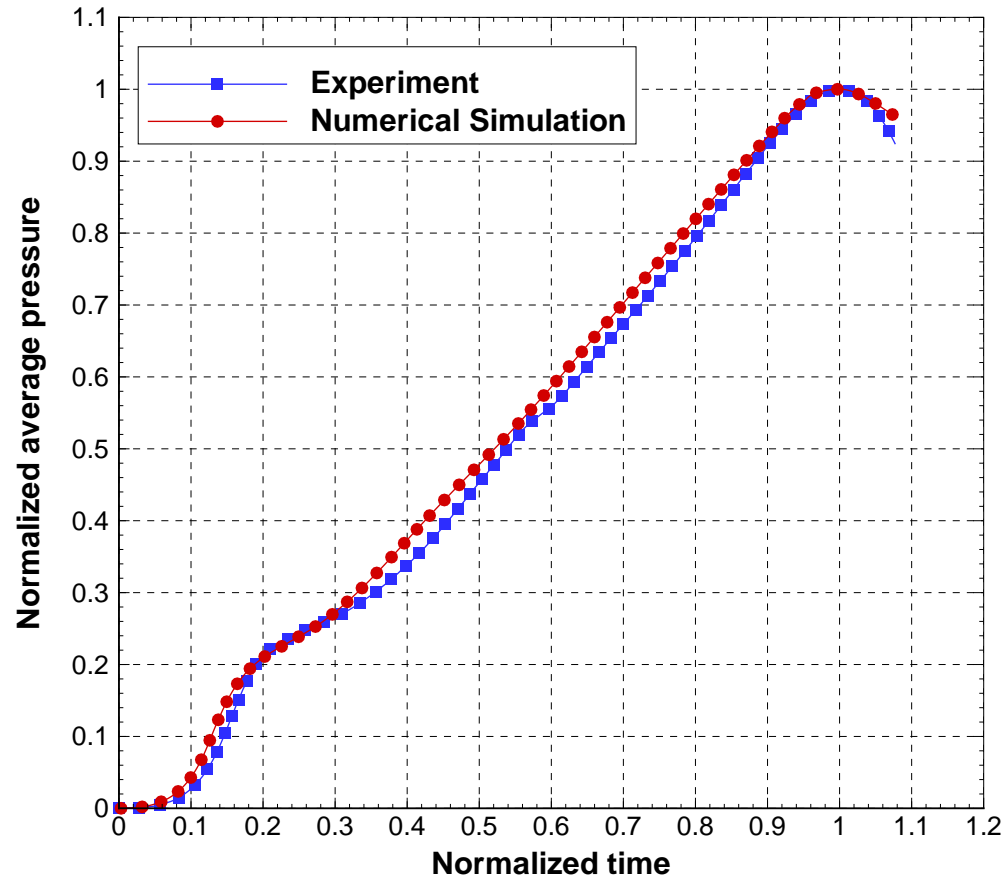


Figure 6.11: Time-history of the average pressure developed in a rectangular chamber.

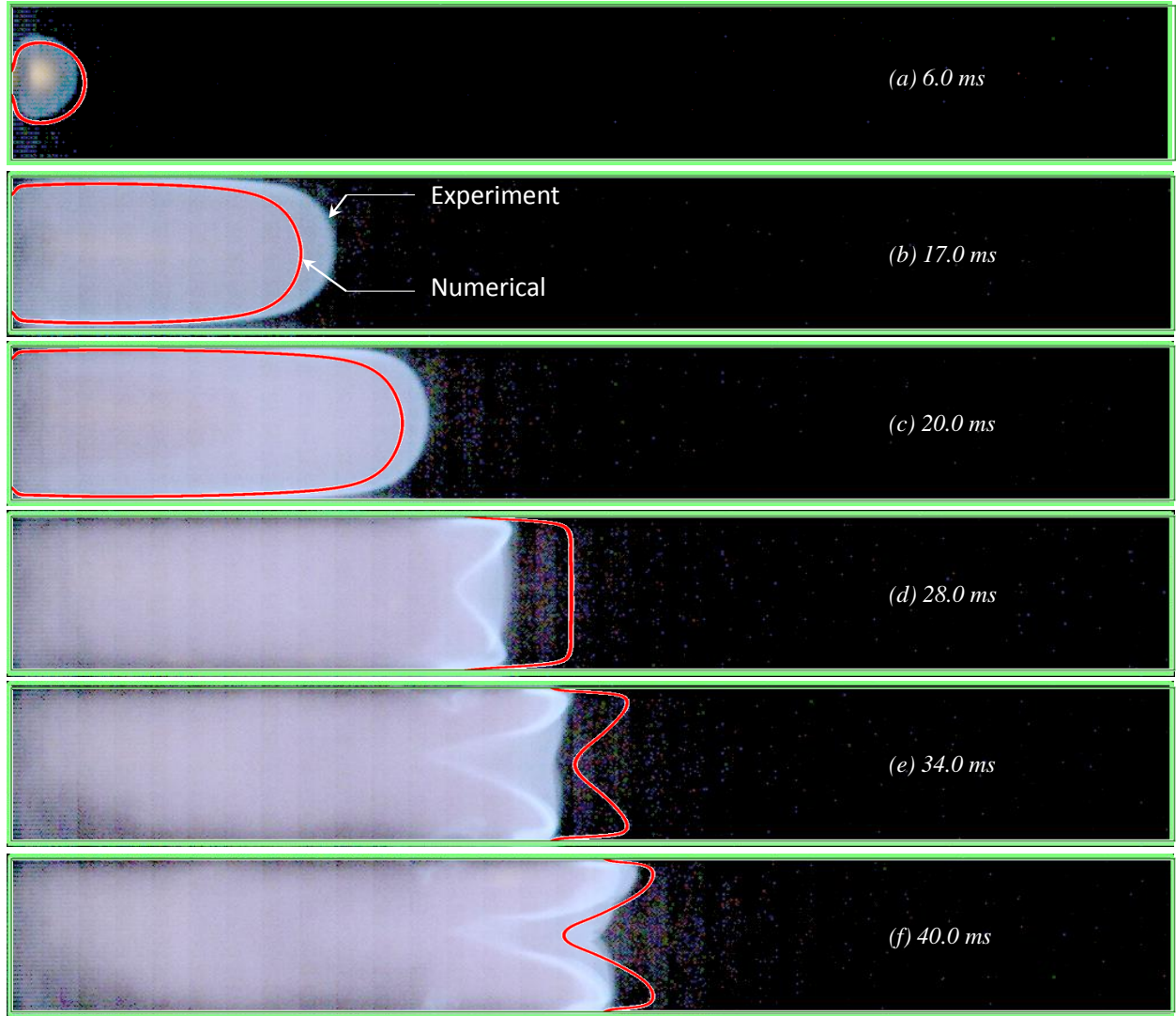


Figure 6.12: Comparison between flame predicted by algebraic flame surface density and experimental observation.

To further assess the transient algebraic flame surface density, the LES and Zimont model with its default parameters values are used to model the confined premixed flame in the rectangular channel. The flame predicted by Zimont model shows deficiency in two aspects; (1) the flame propagation speed is over predicted and (2) unrealistic and diffused flame front. During the tulip flame formation, the spatial gradient of the progress variable extended over the tulip flame tongues which doesn't agree with experimental observations in Fig. 6.12.

The combination of large eddy simulation with eddy viscosity modeled by Wall-Adapting Lo-

cal eddy-viscosity and modified algebraic flame surface density addresses the issues with the Zimont model as shown in Fig. 6.13.

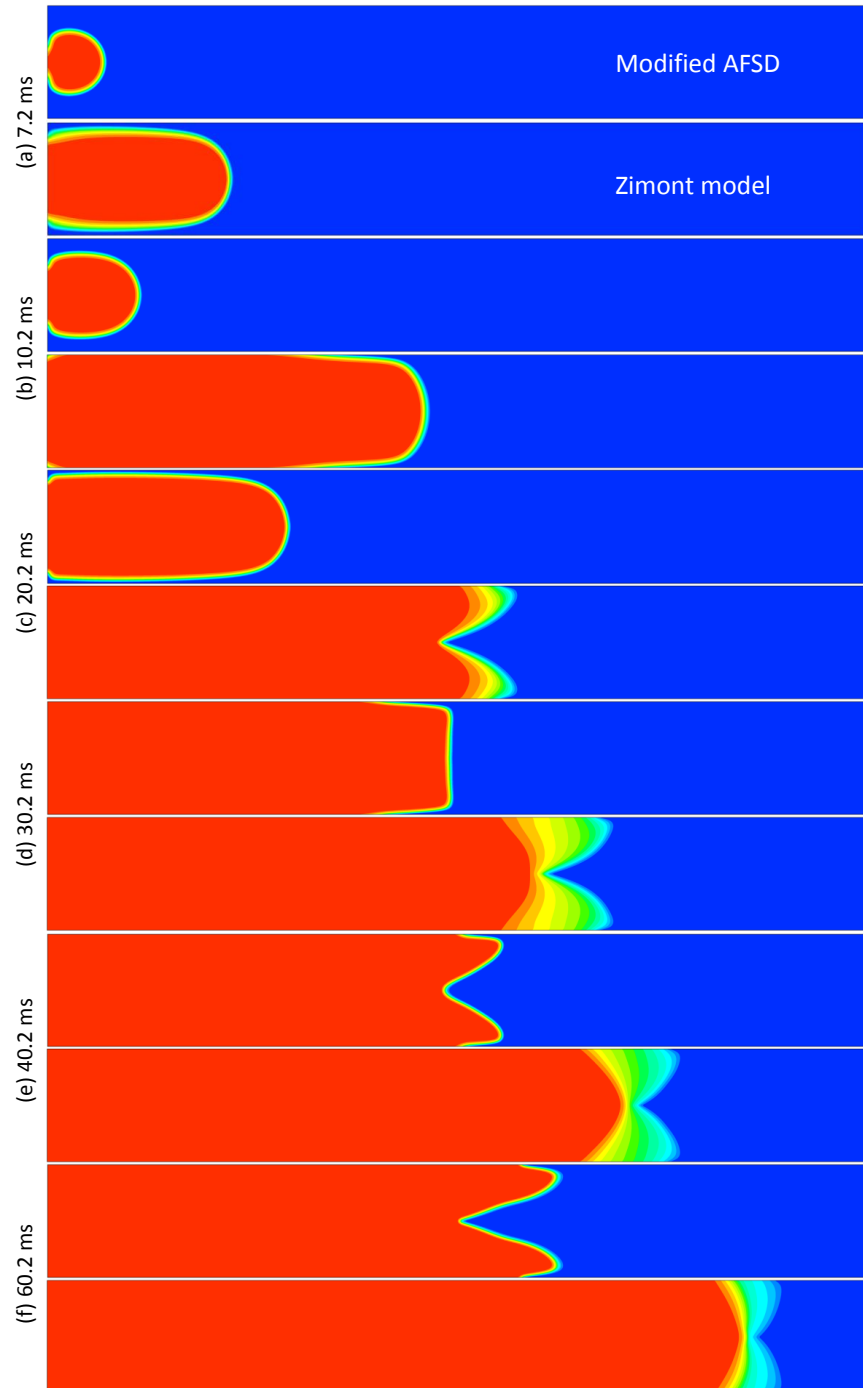


Figure 6.13: Comparison between modified algebraic flame surface density and Zimont model

Chapter 7

CONCLUSIONS AND RECOMMENDATIONS

7.1 Conclusion

This dissertation investigates the propagation of confined premixed flame through closed chamber of isothermal walls and initially quiescent mixture. For two-dimensional analysis, the reaction rate is modeled using detailed and reduced kinetic mechanisms. The mass diffusion is investigated using three different diffusion models with different level of approximation; the multicomponent diffusion model of Chapman-Enskog including Soret effect; the mixture-averaged; and constant Lewis number. For three-dimensional simulation, the large eddy simulation coupled with the reaction progress variable equation is used to model the confined premixed flame in the WDE and rectangular channel. The reaction rate is predicted using Boger model of algebraic flame surface density modified with transient flame speed. The syngas flame dynamics in a rectangular channel of aspect ratio 10 was investigated numerically under different hydrogen content and mixture stoichiometry. Experiment tests were conducted for both WDE and rectangular channel to validate the numerical simulation results and to gain further understanding about the dynamics of the confined premixed flame and resulting pressure growth.

Several conclusions may be drawn from this work.

- (1) The numerical simulation using the San-Diego mechanism reproduced the main features of experimentally observed flame evolution. The numerical results explored the flame front and flame-induced flow interaction in all flame phases.
- (2) The premixed flame propagating in the WDE channel exhibits a conversion from convex (phases I, II) to tulip (phase III) and then from a tulip back to a concave (phase IV) and finally into a more or less steadily propagating flame that eventually is extinguished at the far wall (phase V). In these stages, a weak outer flame is observed and a reduction in heat release is indicated by the diminishment of $p(t)$.
- (3) The pressure, its derivative and its second derivative provide information about the flame stages. The high pressure sampling rate suggests its usefulness as a diagnostic of the events occurring in the CV chamber.
- (4) The rate of pressure rise during CV combustion becomes negative because of heat loss and weak flame propagation (phase (V)).
- (5) The major important deviation between experiment and simulation was the three dimensionality of the former contrasted with the two dimensionality of the latter. The consequences of this difference was discussed in the context of Fig. 5.2. The flame speed using a 2-D simulation is slightly faster than the experiment due excluded "side losses".
- (6) In spite of (5), the comparison in Fig. 5.2 shows that the overall sequence of events is temporally identical. Similar processes occur at identically proportionate times.
- (7) The flame speed experiences dramatic deceleration during the last phase (V), which consumes approximately 75

- (8) The flame generated vorticity is largest along the walls, approximately 5X larger than flame-generated vorticity. Prior to tulip formation, vorticity is generated at the upstream walls. After tulip destruction (second convex flame) vorticity is primarily generated at the downstream walls.
- (9) The Chapman-Enskog multicomponent model $M(I)$ and the mixture-average model $M(I)$ produce almost the same flame structure, peak temperature, average pressure. The maximum deviation in flame distance between these two models was observed at about 3-5 *ms* when the hydrodynamical phenomena associated with thermal expansion is dominated.
- (10) The Soret effect slightly changes the mixture stoichiometry and the equivalence ratio decreased near the cold sidewalls by 3%. The results revealed that the effect of thermal diffusion increases as the difference between the fuel species and oxygen weight increases. The distribution of species concentration in the burned region shows complicated behavior since higher temperature gradient exists, more species get involved, and dissociation phenomena.
- (11) The flame dynamics under unity Lewis number can be characterized into three regions:
- (11-1) Before the lateral flames touch the sidewalls, the hydrodynamic phenomena driven by flame-induced flow is dominant and the unity Lewis number of $M(III)$ is sufficient but producing slower propagation speed compared with $M(I)$ and $M(II)$.
- (11-2) When the lower tongue of the tulip flame start to expand toward the upper tongue at about 11.8 *ms*, a sudden acceleration in the flame $M(III)$ is observed, the peak temperature approaches unrealistic values (from 2460 K to 2830 K), and the average pressure showed more pronounced deviation from the values of $M(I)$ and $M(II)$. This accelerated flame ends by producing an artificial, second tulip flame of smaller size which neither observed in $M(I)$, $M(II)$, nor in the experiment work Najim et al. (2015).

- (11-3) Once the second tulip flame of $M(III)$ annihilated following similar scenario of its predecessor, it starts lagging behind its counterparts of $M(I)$ and $M(II)$ to end of channel.
- (11-4) The syngas/air flame unable to produce wrinkled front when constant Lewis number ($Le = 0.57$) is used. The multicomponent and mixture-averaged diffusion models generate similar wrinkling density on the flame front.
- (12) The values of effective Lewis number for methane/air mixture is above unity (1.13) and it decreases to about 1.07-1.05 when it get closer to the flame vicinity. This slow down the reactivity and stabilize the flame front because the flame develops a convex shape Dinkelacker et al. (2011). Close to the upper tongue and the cusp of the tulip flame, the value of Le_{eff} drop even below unity as indication of increasing the flame tendency to fold and wrinkle its front. Later on the grown front of lower tulip flame tongue, the Le_{eff} also drop below unity flatten the following concave flame immersed from flame lower tongue.
- (13) The influence of mixture stoichiometry on syngas/air flame can be seen in the combustion time, flame structure, and pressure developed. Unlike hydrocarbon fuels, higher propagation speed take place when the mixture is rich at approximately $\phi = 2.0$. The flame propagation speed decelerates near the channel end wall when the average channel pressure is high.
- (14) The syngas flame develops more wrinkles when the mixture lean at elevated pressure. When the syngas/air mixture is rich ($\phi = 1.5$), the high pressure smooths the flame front and the flame tend to be a laminar-like flame at the end of the combustion and for different hydrogen content (Fig. 5.35).
- (15) The large eddy simulation and modified Boger model of algebraic flame surface density used for three-dimensional confined premixed, stoichiometric methane/air flame reproduced,

with good agreement, the experimental observations of the main features of flame structure, pressure time-history, and burning time.

- (16) The increase in unburned gases temperature and pressure during burning works in favor of flame speed which increases rapidly during finger flame expansion and nearly at a constant rate during after tulip flame is developed.
- (17) The Boger model overpredicts the time at which flame front flattens which emphasizes the common deficit of the flame extinction in the turbulent premixed confined flame modeling.

7.2 Recommendations

The dissertation established a reference point from which future advancements in flame and burning acceleration in WDEs and PDE can be assessed. Since these engines must work at high frequencies in order to produce power with a reasonable efficiency, it is recommended that a more realistic turbulence intensity be used for initial condition in order to account for the effect of flow developed during the previous charging process under rotating frame of reference. This should be used in parallel with more advanced optical diagnostics such as Particle Image Velocimetry (PIV) which further provide quantitative information about the velocity field and flame dynamics. The flame can be significantly accelerated through WDE and PDE channel by generating a certain level of turbulence, therefore, a more advanced algebraic flame surface density that accounts for flame stretching, curvature, and flame-turbulence interaction is certainly recommended for the three-dimensional large eddy simulation. One way to increase the turbulence intensity is through flow circulation between two successive channels.

APPENDICES

Appendix A

Grid Resolution Test

As we mentioned in Section 3.3.1, the mesh size is estimated using freely propagating premixed flame. The grid resolution in this work is examined by conducting mesh sensitivity study. Two cases are used for mesh study and summarized in table. A.1. For WDE channel, the premixed methane/air (DRM19) is used with refined cell size of 0.025 *mm*. In the rectangular channel, the premixed syngas/air ($\phi = 1.5$, 80% H_2) flame which exhibits faster propagation speed and hence it would be more sensitive to the mesh resolution than any other cases in this work. The current mesh size of the syngas/air flame is (150×1500) and examined with finer mesh (300×3000) .

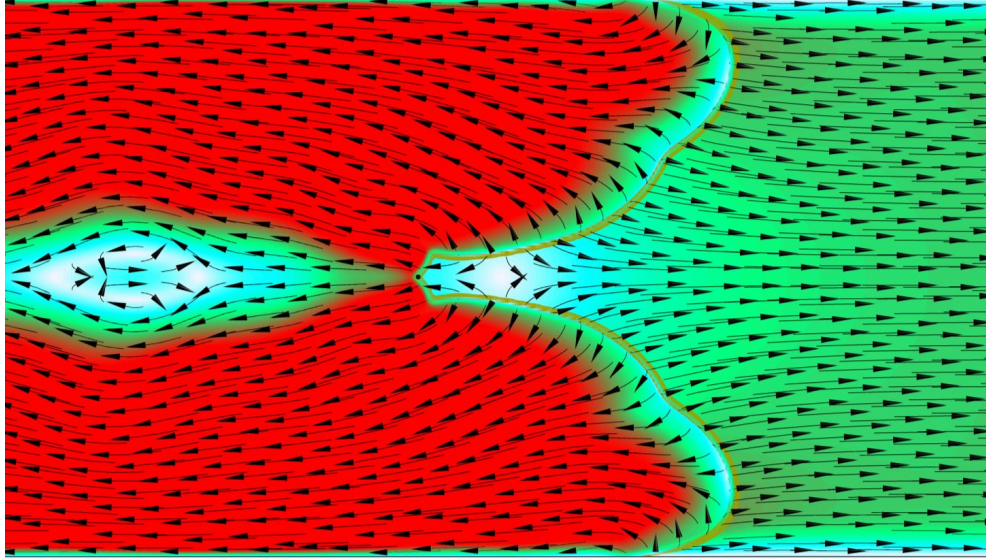
Fuel	Channel	Current cell size	Refined Cell Size
Methane/air (DRM19)	WDE	0.05	0.025 mm
Syngas/air ($\phi = 1.5$, 80% H_2)	Rectangular	(150×1500)	(300×3000)

Table A.1: CFD cases used to examine grid resolution.

The comparison between these cases reveals that current grid resolution used in the syngas or methane flames are sufficient and generates similar flame structure and propagation speed, see Fig. A.1. The flame-generated flow is quantitatively the same in both syngas and methane flames. In rectangular channel, the saddle point developed in front of the syngas/air flame cusp at the channel centerline and vortical motion developed behind the flame cusp in the burned gases region. However, the results shows slightly different flame position at the channel centerline where the

flame with finer mesh advances by 1.1 *mm* at the same combustion time. The channel average pressure for both cases is shown in Fig. A.2. It can be seen that the fine mesh case predict slightly higher pressure than the current mesh case.

(a) Mesh (150x1500), $t=2.7$ (ms), flame position at channel Centerline=55.2 (mm)



(b) Mesh (300x3000), $t=2.7$ (ms), flame position at channel Centerline=56.3 (mm)

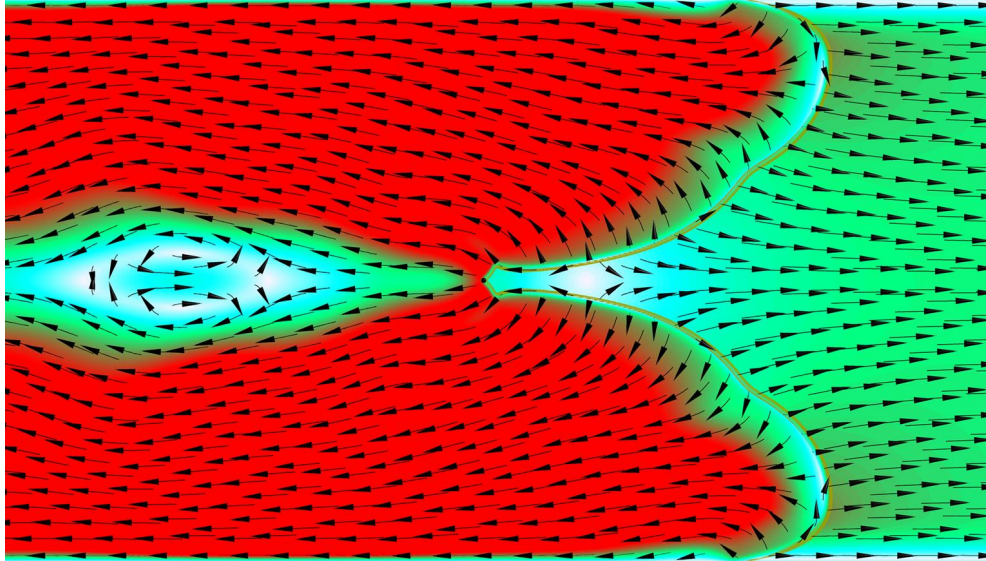


Figure A.1: Flame front structure and flame-generated flow predicted by (a) current mesh size(150×1500) and (b) finer mesh(300×3000).

The methane/air flames front structure for the current and refined cell sizes are shown in Fig. A.3. Figure. A.3 indicates that the current and refined grid resolutions and generate simi-

lar flame structure. The refined mesh generates, however, more HCO species within the flame front. The flame front thickness is slightly reduced by the refined mesh.

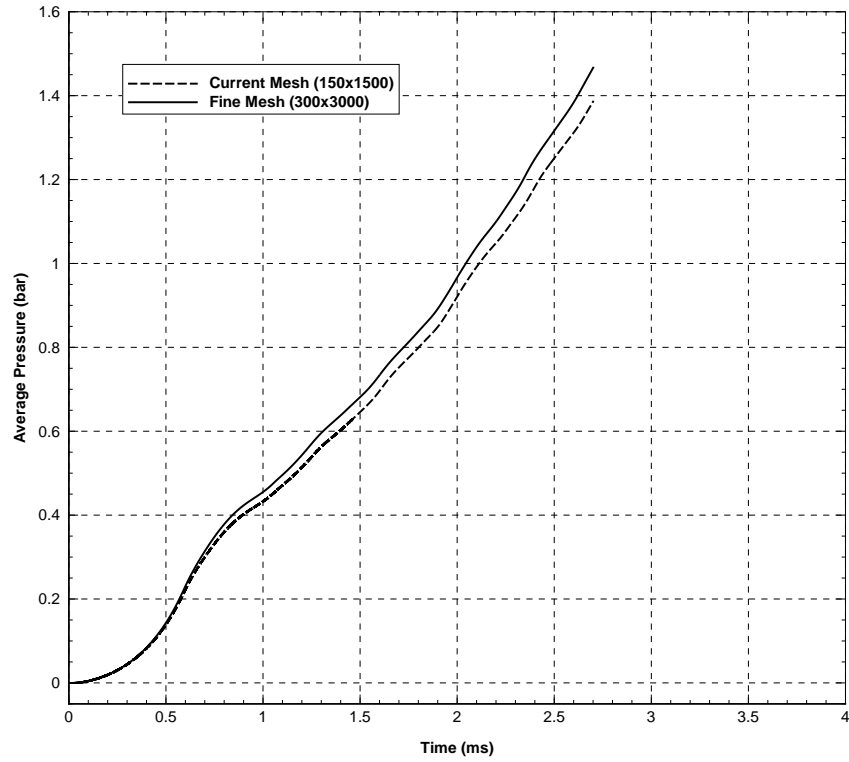


Figure A.2: Average pressure of the syngas/air premixed flames.

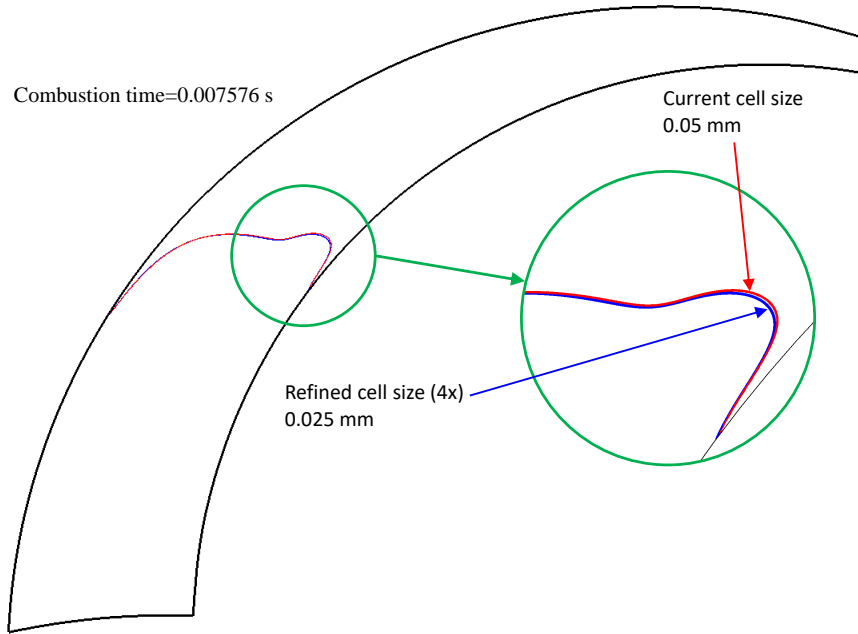


Figure A.3: Methane/air flame front structure predicted by 0.05 mm and 0.025 mm maximum cell sizes. The Flames front are represented by C_2H_6 contours.

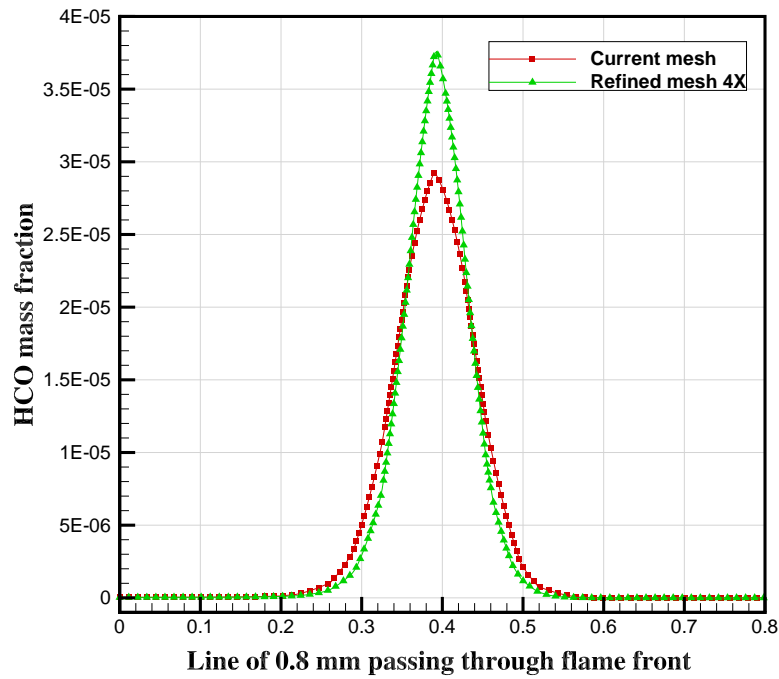


Figure A.4: Mass fraction of HCO species plotted along a line of 0.8 mm passing through the methane/air flames front.

Appendix B

Turbulent Flame Model

Turbulence Intensity

In this Section, the turbulence parameters are presented to assess the turbulence intensity developed during the three-dimensional, premixed flame propagation. In Fig. B.1, the maximum cell Reynolds number is plotted versus burning time in the rectangular channel and showing proportional behavior with the local velocity.

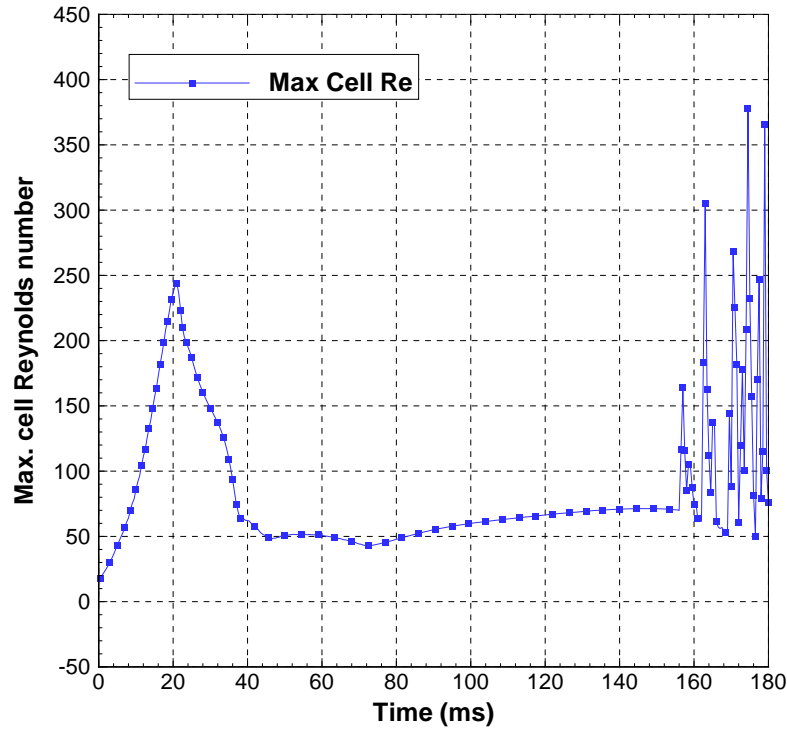


Figure B.1: Maximum cell Reynolds number evaluated during flame propagating in the 3D rectangular channel.

The cell Re increases during the spherical flame expansion during which the burned gases dramatically expands toward the cold, unburned region. Figure. B.1 reveals that the maximum cell Re showing high fluctuation at the time when the flame front annihilated by the channel end wall causing significant disturbance for the flame-generated flow. Since the flame at the end of the WDE channel shows weak propagation, the cell Re progressively decrease during this time.

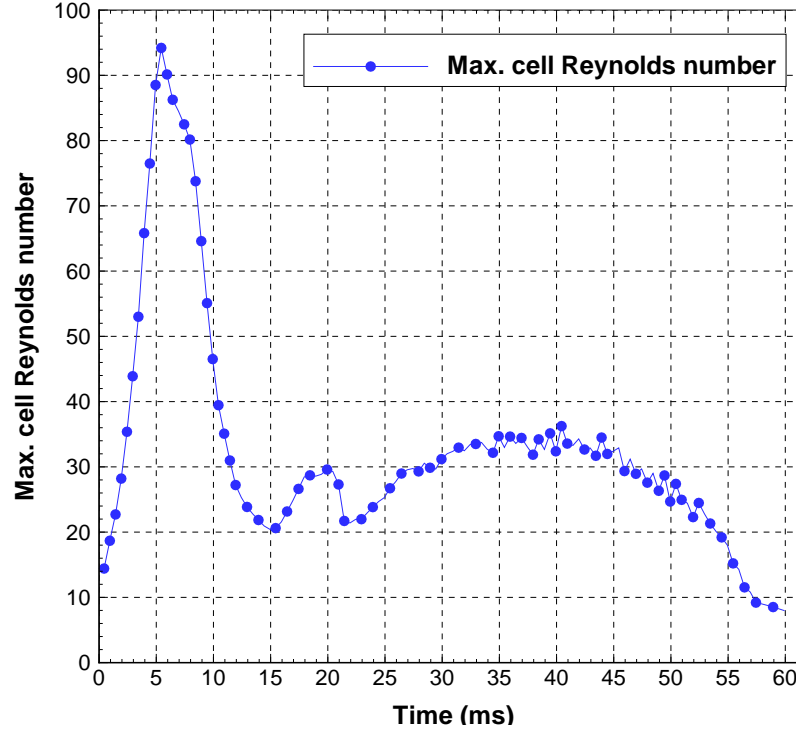


Figure B.2: Maximum cell Reynolds number evaluated during flame propagating in WDE channel.

The flow effect on the flame front structure is generally quantified using Damköhler number ($Da = \frac{\tau_c}{\tau_l}$). Figure B.3 shows large Damköhler numbers evolution during burning which indicates that the chemical time scale τ_c is much smaller than the flow time scale τ_l and represent the case of infinitely fast chemistry. It can be seen that the Damköhler number curve in Fig. B.3 exhibits a reverse behavior to the maximum cell Reynolds number presented in Fig. B.2.

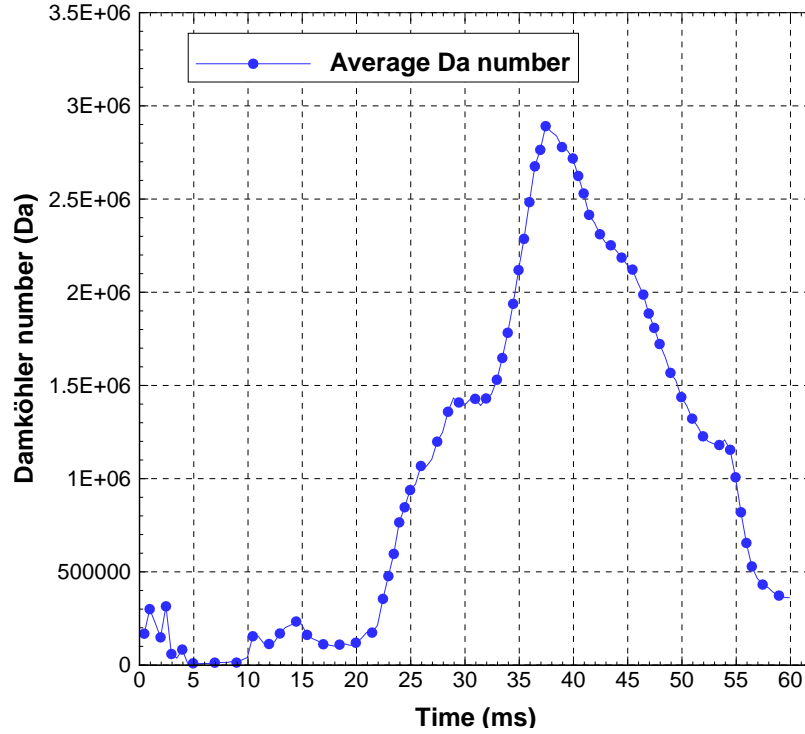


Figure B.3: Average Damköhler number for WDE channel.

Calculation of unburned gases density

In confined chambers, the flame front represent a surface that separates the burned and unburned regions. The thermochemical and transport properties of the burned gases are significantly different from unburned gases. The unburned gases density is calculated as the weighted average of the unburnt density in a computational element at which the reaction progress variable is less than 0.001. When the reaction progress variable is larger than 0.001 everywhere in the domain, then the unburnt density is the minimum density in all computational elements. In constant volume combustion, the average density is constant for the entire mixture because the total mass remains unchanged during burning. The density of the unburned gases, however, increases, as the pressure build up in the channel, see Figs. B.4, B.5.

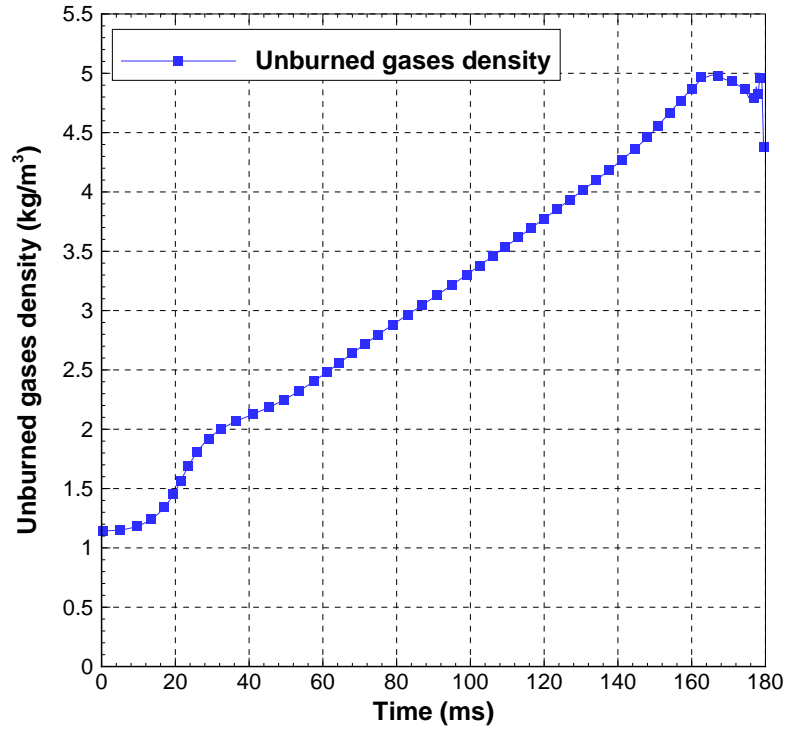


Figure B.4: Unburned gases density developed during flame propagation in a rectangular channel.

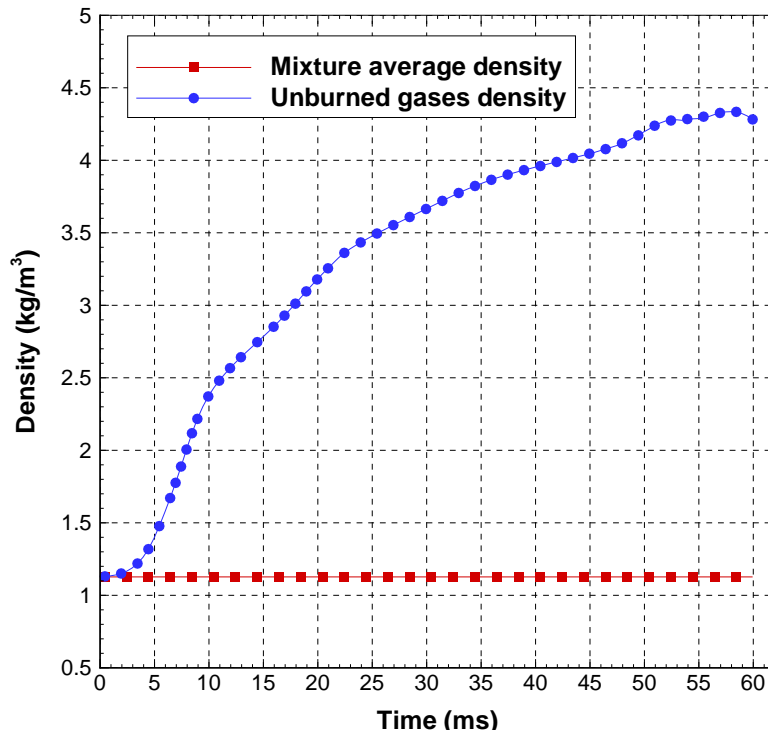


Figure B.5: Unburned gases density developed during flame propagation in the WDE channel. Also showing the mixture average density.

BIBLIOGRAPHY

BIBLIOGRAPHY

- Andac, M.G. & F.N. Egolfopoulos. 2007. Diffusion and kinetics effects on the ignition of premixed and non-premixed flames. *Proceedings of the Combustion Institute* 31(1). 1165–1172.
- ANSYS® Academic Research. 2015. Release 16.2, help system, fluent theory guide, ansys, inc. www.ansys.com.
- Beeckmann, J., L. Cai & H. Pitsch. 2014. Experimental investigation of the laminar burning velocities of methanol, ethanol, n-propanol, and n-butanol at high pressure. *Fuel* 117(Part A). 340 – 350.
- Bird, R.B., W.E. Stewart & E.N. Lightfoot. 2007. *Transport phenomena* Wiley International edition. Wiley.
- Boger, M., D. Veynante, H. Boughanem & A. Trouvé. 1998. Direct numerical simulation analysis of flame surface density concept for large eddy simulation of turbulent premixed combustion. *Symposium (International) on Combustion* 27(1). 917 – 925.
- Bongers, H. & L. P. H. De Goey. 2003. The effect of simplified transport modeling on the burning velocity of laminar premixed flames. *Combustion Science and Technology* 175(10). 1915–1928.
- Bouvet, Nicolas, Fabien Halter, Christian Chauveau & Youngbin Yoon. 2013. On the effective lewis number formulations for lean hydrogen/hydrocarbon/air mixtures. *International Journal of Hydrogen Energy* 38(14). 5949 – 5960.
- Brambilla, Andrea, Marco Schultze, Christos E. Frouzakis, John Mantzaras, Rolf Bombach & Konstantinos Boulouchos. 2015. An experimental and numerical investigation of premixed syn-gas combustion dynamics in mesoscale channels with controlled wall temperature profiles. *Proceedings of the Combustion Institute* 35(3). 3429 – 3437.
- Bray, K. N. C. & R. S. Cant. 1991. Some applications of kolmogorov's turbulence research in the field of combustion. *Proceedings: Mathematical and Physical Sciences* 434(1890). 217–240.
- Burbano, Hugo J., Jhon Pareja & Andrès A. Amell. 2011. Laminar burning velocities and flame stability analysis of H₂/CO/air mixtures with dilution of N₂ and CO₂. *International Journal of Hydrogen Energy* 36(4). 3232 – 3242.
- Chapman, S & T G Cowling. 1970. *The mathematical theory of non-uniform gases: An account of the kinetic theory of viscosity, thermal conduction and diffusion in gases* Cambridge Mathematical Library. Cambridge University Press.
- Chemical-Kinetic Mechanisms for Combustion Applications, San Diego Mechanism web page,

- Mechanical and Aerospace Engineering (Combustion Research), University of California at San Diego. 2014. <http://combustion.ucsd.edu>.
- CHEMKIN-PRO 15131. 2013. Reaction Design: San Diego. <http://www.reactiondesign.com/products/chemkin/chemkin-2/>.
- Chomiak, Jerry & Gang Hou. 1996. A numerical study of large amplitude baroclinic instabilities of flames. *Symposium (International) on Combustion* 26(1). 883 – 889.
- Clanet, Christophe & Geoffrey Searby. 1996. On the “tulip flame” phenomenon. *Combustion and Flame* 105(1 - 2). 225 – 238.
- Clavin, Paul. 1985. Dynamic behavior of premixed flame fronts in laminar and turbulent flows. *Progress in Energy and Combustion Science* 11(1). 1–59.
- D’ippolito, Cesare. 2015. *A numerical study of syngas laminar premixed flames: Effects of lewis number and flame stretch*: Politecnico di Torino dissertation.
- Damköhler, Gerhard. 1947. The effect of turbulence on the flame velocity in gas mixtures. *Z. Elektrochem* 46. 601.
- De Charentenay, J. & a. Ern. 2002. Multicomponent transport impact on premixed turbulent H₂/O₂ flames. *Combustion Theory Modelling* 6(3). 439–462.
- Dinesh, K.K.J. Ranga, H. Shalaby, K.H. Luo, J.A. van Oijen & D. Thévenin. 2016. High hydrogen content syngas fuel burning in lean premixed spherical flames at elevated pressures: Effects of preferential diffusion. *International Journal of Hydrogen Energy* 41(40). 18231 – 18249.
- Dinesh, K.K.J. Ranga, H. Shalaby, K.H. Luo & D. Thévenin. 2015a. Flame structure analysis for turbulent lean premixed spherical flames at elevated pressures. In *7th european combustion meeting ECM2015, Budapest, Hungary*, .
- Dinesh, K.K.J. Ranga, H. Shalaby, K.H. Luo & D. Thévenin. 2015b. Numerical investigation of turbulent lean premixed H₂/CO combustion at elevated pressures. In *25th international colloquium on the dynamics of explosions and reactive systems ICDERS2015, Leeds, Uk*, .
- Dinkelacker, F., B. Manickam & S.P.R. Muppala. 2011. Modelling and simulation of lean premixed turbulent methane/hydrogen/air flames with an effective lewis number approach. *Combustion and Flame* 158(9). 1742 – 1749.
- Dunn-Rankin, D., P.K. Barr & R.F. Sawyer. 1988. Numerical and experimental study of “tulip” flame formation in a closed vessel. *Symposium (International) on Combustion* 21(1). 1291–1301.
- Dunn-Rankin, D. & R. F. Sawyer. 1998. Tulip flames: changes in shape of premixed flames

- propagating in closed tubes. *Experiments in Fluids* 24(2). 248 – 256.
- Dworkin, S.B., M.D. Smooke & V. Giovangigli. 2009. The impact of detailed multicomponent transport and thermal diffusion effects on soot formation in ethylene/air flames. *Proceedings of the Combustion Institute* 32(1). 1165–1172.
- Ellis, O. C. 1928. Flame movement in gaseous explosive mixtures. *Fuel in Science and Practice* 7. 502–508.
- Emami, Sina Davazdah, Meisam Rajabi, Che Rosmani Che Hassan, Mahar Diana A. Hamid, Rafiziana M. Kasmani & Mojtaba Mazangi. 2013. Experimental study on premixed hydrogen/air and hydrogen-methane/air mixtures explosion in 90 degree bend pipeline. *International Journal of Hydrogen Energy* 38(32). 14115 – 14120.
- Ern, Alexandre & Vincent Giovangigli. 1999. Impact of detailed multicomponent transport on planar and counterflow hydrogen/air and methane/air flames. *Combustion Science and Technology* 149(1-6). 157–181.
- Ern, Alexandre & Vincent Giovangigli. 2008. *Multicomponent transport algorithms* Lecture Notes in Physics Monographs. Springer Berlin Heidelberg.
- Eslamian, Morteza. 2012. Advances in thermodiffusion and thermophoresis (Soret effect) in liquid mixtures. *Frontiers in Heat and Mass Transfer* 2(4).
- Frenklach, A. Kazakov & M. 1994. Kinetic mechanism DRM, <http://www.me.berkeley.edu/drm/>.
- Giacomazzi, E., F. R. Picchia & N. Arcidiacono. 2007. A review of chemical diffusion: Criticism and limits of simplified methods for diffusion coefficient calculation. *Combustion Theory and Modelling* 12(1). 135–158.
- Giovangigli, Vincent. 2014. Multicomponent transport in laminar flames. *Proceedings of the Combustion Institute* 35(1). 625–637.
- Glassman, Irvin, Richard A. Yetter & Nick G. Glumac. 2015. Chapter 4 - flame phenomena in premixed combustible gases. In Irvin Glassman, Richard A. Yetter & Nick G. Glumac (eds.), *Combustion (fifth edition)*, 147 – 254. Boston: Academic Press fifth edition edn.
- Gonzalez, M., R. Borghi & A. Saouab. 1992. Interaction of a flame front with its self-generated flow in an enclosure: The “tulip flame” phenomenon. *Combustion and Flame* 88(2). 201 – 220.
- Grcar, Joseph F., John B. Bell & Marcus S. Day. 2009. The solet effect in naturally propagating, premixed, lean, hydrogen-air flames. *Proceedings of the Combustion Institute* 32(1). 1173–1180.
- Gülde, Ömer & Gregory Smallwood. 2007. Flame surface densities in premixed combustion at medium to high turbulence intensities. *Combustion Science and Technology* 179(1-2). 191–206.

- Halter, F., C. Chauveau, N. Djebaili-Chaumeix & I. Gökalp. 2005. Characterization of the effects of pressure and hydrogen concentration on laminar burning velocities of methane-hydrogen-air mixtures. *Proceedings of the Combustion Institute* 30(1). 201 – 208.
- Han, Wang & Zheng Chen. 2015. Effects of soot diffusion on premixed counterflow flames. *Combustion Science and Technology* 187(8). 1195–1207.
- Hariharan, Ashwin & Indrek S. Wichman. 2014. Premixed flame propagation and morphology in a constant volume combustion chamber. *Combustion Science and Technology* 186(8). 1025–1040.
- Hassan, M. I., K. T. Aung & G. M. Faeth. 1997. Properties of laminar premixed CO/H₂/air flames at various pressures. *American Institute of Aeronautics and Astronautics* 13(2). 239 – 254.
- Hilbert, R., F. Tap, H. El-Rabii & D. Thévenin. 2004. Impact of detailed chemistry and transport models on turbulent combustion simulations. *Progress in Energy and Combustion Science* 30(1). 61–117.
- Jeung, In-Seuck & Kyung-Kook Cho. 1989. Role of flame generated flow in the formation of tulip flame. In *27th aerospace sciences meeting*, 492.
- Johansen, Craig Thomas. 2009. *Experimental and numerical investigation of flame acceleration in an obstructed channel*: Queen's University dissertation.
- Kadowaki, Satoshi, Hiroshi Suzuki & Hideaki Kobayashi. 2005. The unstable behavior of cellular premixed flames induced by intrinsic instability. *Proceedings of the Combustion Institute* 30(1). 169–176.
- Kazakov, Andrei & Michael Frenklach. 1994. Reduced reaction sets based on GRI-Mech 1.2. *University of California at Berkeley, Berkeley, CA*, <http://www.me.berkeley.edu/drm>.
- Kéromnès, Alan, Wayne K. Metcalfe, Karl A. Heufer, Nicola Donohoe, Apurba K. Das, Chih-Jen Sung, Jörgen Herzler, Clemens Naumann, Peter Griebel, Olivier Mathieu, Michael C. Krejci, Eric L. Petersen, William J. Pitz & Henry J. Curran. 2013. An experimental and detailed chemical kinetic modeling study of hydrogen and syngas mixture oxidation at elevated pressures. *Combustion and Flame* 160(6). 995 – 1011.
- Kiran, R., I. Wichman & N. Mueller. 2013. On combustion in a closed rectangular channel. *8th US National Combustion Meeting* 3. 2147–2155.
- Kiran, Rohitashwa. 2013. *Numerical simulations for performance enhancement of a radial, pressure wave driven, internal combustion engine*: Michigan State University dissertation.
- Kiran, Rohitashwa, Indrek S. Wichman & Norbert Mueller. 2014. On combustion in a closed rectangular channel with initial vorticity. *Combustion Theory and Modelling* 18(2). 272–294.

- Kleijn, Chris R & Harry E A Van Den Akker. 1999. Multi-component diffusion in 2-dimensional laminar methane / air flames. *ASME, Pressure Vessels and Piping* (397-1). 1–9.
- Kleijn, CR. 1995. Chemical vapor deposition processes. *Computational modeling in semiconductor processing* 97–229.
- Kuo, K.K. 2005. *Principles of combustion*. John Wiley.
- Kuzuu, Kazuto, Katsuya Ishii & Kunio Kuwahara. 1996. Numerical simulation of premixed flame propagation in a closed tube. *Fluid Dynamics Research* 18(3). 165 – 182.
- Lewis, B. & G. v. Elbe. 1987. *Combustion, flames and explosions of gases*. San Diego: Academic Press 2nd edn.
- Li, Hong-Meng, Guo-Xiu Li, Zuo-Yu Sun, Yue Zhai & Zi-Hang Zhou. 2014. Research on cellular instabilities of lean premixed syngas flames under various hydrogen fractions using a constant volume vessel. *Energies* 7(7). 4710–4726.
- Liu, Jie, Xin Zhang, Tao Wang, Xiaosen Hou, Jibao Zhang & Shizhuo Zheng. 2015. Numerical study of the chemical, thermal and diffusion effects of H₂ and CO addition on the laminar flame speeds of methane-air mixture. *International Journal of Hydrogen Energy* 40(26). 8475 – 8483.
- Marble, F & J Broadwell. 1977. The coherent flame model of non-premixed turbulent combustion. *Project Squid TRW-9-PU, Project Squid Headquarters, Chaffee Hall, Purdue University*.
- Matalon, Moshe. 2009. Flame dynamics. *Proceedings of the Combustion Institute* 32(1). 57–82.
- Matalon, Moshe. 2014. Laminar premixed flames, lewis number effects and flame stretch. Lecture presented at Princeton University-Combustion Energy Frontier Research Center-Combustion Institute.
- Matalon, Moshe & Jennifer L. McGreevy. 1994. The initial development of a tulip flame. *Symposium (International) on Combustion* 25(1). 1407 – 1413.
- Matalon, Moshe & Philippe Metzener. 1997. The propagation of premixed flames in closed tubes. *J. Fluid Mech.* 336. 331–350. 1997 Cambridge University Press.
- McGee, H A. 1991. *Molecular engineering*. McGraw Hill.
- McIlroy, A, G McRae, V Sick, DL Siebers, CK Westbrook, PJ Smith, C Taatjes, A Trouve, AF Wagner, E Rohlfing et al. 2006. Basic research needs for clean and efficient combustion of 21st century transportation fuels. Tech. rep. DOESC (USDOE Office of Science (SC)).
- Metghalchi, M. & J.C. Keck. 1980. Laminar burning velocity of propane-air mixtures at high temperature and pressure. *Combustion and Flame* 38. 143 – 154.

- Muppala, S.P.R., M. Nakahara, N.K. Aluri, H. Kido, J.X. Wen & M.V. Papalexandris. 2009. Experimental and analytical investigation of the turbulent burning velocity of two-component fuel mixtures of hydrogen, methane and propane. *International Journal of Hydrogen Energy* 34(22). 9258 – 9265.
- Najim, Younis M., Norbert Mueller & Indrek S. Wichman. 2015. On premixed flame propagation in a curved constant volume channel. *Combustion and Flame* 162(10). 3980 – 3990.
- Nicoud, F. & F. Ducros. 1999. Subgrid-scale stress modelling based on the square of the velocity gradient tensor. *Flow, Turbulence and Combustion* 62(3). 183–200.
- Ogle, Russell A. 2017. Chapter 8 - confined unsteady dust flame propagation. In Ogle & Russell A. (eds.), *Dust explosion dynamics*, 407 – 498. Butterworth-Heinemann.
- Peters, N. 1988. Laminar flamelet concepts in turbulent combustion. *Symposium (International) on Combustion* 21(1). 1231 – 1250.
- Peters, N. 1999. The turbulent burning velocity for large-scale and small-scale turbulence. *Journal of Fluid mechanics* 384. 107–132.
- Peters, N. 2000. *Turbulent combustion* Cambridge Monographs on Mechanics. Cambridge University Press.
- Poinsot, T. & D. Veynante. 2005. *Theoretical and numerical combustion*. Edwards.
- Ponizy, Bogdan, Alain Claverie & Bernard Veyssi re. 2014. Tulip flame - the mechanism of flame front inversion. *Combustion and Flame* 161(12). 3051 – 3062.
- Pope, S.B. 2000. *Turbulent flows*. Cambridge University Press.
- Qin, Xiao & Yiguang Ju. 2005. Measurements of burning velocities of dimethyl ether and air premixed flames at elevated pressures. *Proceedings of the Combustion Institute* 30(1). 233 – 240.
- Reid, R.C. & T.K. Sherwood. 1966. *The properties of gases and liquids: their estimation and correlation* McGraw-Hill chemical engineering series. McGraw-Hill.
- Shang, Rongxue, Yang Zhang, Mingming Zhu, Zhezi Zhang, Dongke Zhang & Gang Li. 2016. Laminar flame speed of CO₂ and N₂ diluted H₂/CO/air flames. *International Journal of Hydrogen Energy* 41(33). 15056 – 15067.
- Singh, Deepti, Takayuki Nishiie, Saad Tanvir & Li Qiao. 2012. An experimental and kinetic study of syngas/air combustion at elevated temperatures and the effect of water addition. *Fuel* 94. 448 – 456.

- Smooke, Mitchell D. 2013. The computation of laminar flames. *Proceedings of the Combustion Institute* 34(1). 65–98.
- Starke, R. & P. Roth. 1986. An experimental investigation of flame behavior during cylindrical vessel explosions. *Combustion and Flame* 66(3). 249 – 259.
- Sun, G, Pezhman Akbari, B Gower & N Muller. 2012. Thermodynamics of the wave disk engine. *AIAA Paper* 3704.
- Sun, Guangwei. 2011. *Numerical study of the aerodynamic characteristics of a wave disc engine*: Michigan State University dissertation.
- Sun, Hongyan, S.I. Yang, G. Jomaas & C.K. Law. 2007. High-pressure laminar flame speeds and kinetic modeling of carbon monoxide/hydrogen combustion. *Proceedings of the Combustion Institute* 31(1). 439 – 446.
- Swaminathan, N. & K.N.C. Bray. 2011. *Turbulent premixed flames* Cambridge books online. Cambridge University Press.
- Tuncer, Onur & A. Mendez-Vilas. 2013. Premixed combustion of hydrogen and syngas fuels in gas turbine combustors. *Materials and Processes for Energy: Communicating Current Research and Technological Developments, Formatex Research Center, Badajoz, Spain* 946–957.
- Turns, S.R. 2012. *An introduction to combustion: Concepts and applications* McGraw-Hill series in mechanical engineering. McGraw-Hill.
- U.S Department of Energy. 2015. Annual energy outlook 2015. <https://www.eia.gov/analysis>.
- Vagelopoulos, Christine M. & Fokion N. Egolfopoulos. 1998. Direct experimental determination of laminar flame speeds. *Symposium (International) on Combustion* 27(1). 513 – 519. Twenty-Seventh Symposium (International) on Combustion Volume One.
- Vedachalam, N., S. Srinivasalu, G. Rajendran, G.a. Ramadass & M.a. Atmanand. 2015. Review of unconventional hydrocarbon resources in major energy consuming countries and efforts in realizing natural gas hydrates as a future source of energy. *Journal of Natural Gas Science and Engineering* 26. 163–175.
- Veynante, Denis & Luc Vervisch. 2002. Turbulent combustion modeling. *Progress in Energy and Combustion Science* 28(3). 193 – 266.
- Wichman, Indrek S. & Gilles Bruneaux. 1995. Head-on quenching of a premixed flame by a cold wall. *Combustion and Flame* 103(4). 296 – 310.
- Williams, Bradley A. 2001. Sensitivity of calculated extinction strain rate to molecular transport formulation in nonpremixed counterflow flames. *Combustion and Flame* 124(1-2). 330–333.

- Williams, F.A. 1975. Recent advances in theoretical descriptions of turbulent diffusion flames. In S.N.B. Murthy (ed.), *Turbulent mixing in nonreactive and reactive flows*, 189–208. Springer New York.
- Wu, Fujia, Andrew P. Kelley, Chenglong Tang, Delin Zhu & Chung K. Law. 2011. Measurement and correlation of laminar flame speeds of CO and C2 hydrocarbons with hydrogen addition at atmospheric and elevated pressures. *International Journal of Hydrogen Energy* 36(20). 13171 – 13180.
- Xiao, Huahua, Xuechao He, Qiangling Duan, Xisheng Luo & Jinhua Sun. 2014a. An investigation of premixed flame propagation in a closed combustion duct with a 90° bend. *Applied Energy* 134. 248 – 256.
- Xiao, Huahua, Ryan W. Houim & Elaine S. Oran. 2015. Formation and evolution of distorted tulip flames. *Combustion and Flame* 162(11). 4084 – 4101.
- Xiao, Huahua, Dmitriy Makarov, Jinhua Sun & Vladimir Molkov. 2012a. Experimental and numerical investigation of premixed flame propagation with distorted tulip shape in a closed duct. *Combustion and Flame* 159(4). 1523 – 1538.
- Xiao, Huahua, Dmitriy Makarov, Jinhua Sun & Vladimir Molkov. 2012b. Experimental and numerical investigation of premixed flame propagation with distorted tulip shape in a closed duct. *Combustion and Flame* 159(4). 1523–1538.
- Xiao, Huahua, Jinhua Sun & Peng Chen. 2014b. Experimental and numerical study of premixed hydrogen/air flame propagating in a combustion chamber. *Journal of Hazardous Materials* 268. 132 – 139.
- Xiao, Huahua, Qingsong wang, Xiaobo Shen, Song Guo & Jinhua Sun. 2013. An experimental study of distorted tulip flame formation in a closed duct. *Combustion and Flame* 160(9). 1725 – 1728.
- Xin, Yuxuan, Wenkai Liang, Wei Liu, Tianfeng Lu & Chung K. Law. 2015. A reduced multicomponent diffusion model. *Combustion and Flame* 162(1). 68–74.
- Yang, F., H.Q. Zhang & X.L. Wang. 2011. Effects of soot diffusion on the laminar flame speed of n-butane-air mixtures. *Proceedings of the Combustion Institute* 33(1). 947 – 953.
- Zhang, Weikuo, Xiaolong Gou, Wenjun Kong & Zheng Chen. 2016. Laminar flame speeds of lean high-hydrogen syngas at normal and elevated pressures. *Fuel* 181. 958 – 963.
- Zhou, Biao, Andrzej Sobiesiak & Peng Quan. 2006. Flame behavior and flame-induced flow in a closed rectangular duct with a 90° bend. *International Journal of Thermal Sciences* 45(5). 457 – 474.

Zimont, V, W Polifke, M Bettelini & W Weisenstein. 1998. An efficient computational model for premixed turbulent combustion at high reynolds numbers based on a turbulent flame speed closure. *Journal of Engineering for Gas Turbines and Power* 120(3). 526–532.